Using compartment models of diffusion MRI to investigate the preterm brain

Zach Eaton-Rosen

A dissertation submitted in partial fulfillment

of the requirements for the degree of

Doctor of Philosophy

of

University College London.

Department of Medical Physics and Biomedical Engineering

University College London

September 20, 2017

I, Zach Eaton-Rosen, confirm that the work presented in this thesis is my own. Where information has been derived from other sources, I confirm that this has been indicated in the work.

Abstract

Preterm birth is the leading cause of neonatal mortality, with survivors experiencing motor, cognitive and other deficits at increased rates. In preterm infancy, the developing brain undergoes folding, myelination, and rapid cellular growth. Diffusion-Weighted Magnetic Resonance Imaging (DW MRI) is an imaging modality that allows non-invasive inference of cellular microstructure in living tissue, and its parameters reflect changes in brain tissue composition. In this thesis, we employ compartment models of DW MRI to investigate the microstructure in preterm-born subjects at different ages.

Within infants, we have used the NODDI model to investigate longitudinal changes in neurite density and orientation dispersion within the white matter, cerebral cortex and thalamus, explaining known trends in diffusion tensor parameters with greater specificity. We then used a quantitative T_2 sequence to develop and investigate a novel, multi-modal parameter known as the 'g-ratio'. We have also investigated changing microstructural geometry within the cortex. Immediately after preterm birth, the highly-ordered underlying cellular structure makes diffusion in the cortex almost entirely radial. This undergoes a transition to a disordered and isotropic state over the first weeks of life, which we have used the DIAMOND model to quantify. This radiality decreases at a rate that depends on the cortical lobe.

In a cohort of young adults born extremely preterm, we have quantified differences in brain microstructure compared to term-born controls. In preterm subjects, the brain structures are smaller than for controls, leading to increased partial volume in some regions of interest. We introduce a method to infer diffusion parameters in partial volume, even for regions which are smaller than the diffusion resolution.

Overall, this thesis utilises and evaluates a variety of compartment models of DW MRI. By developing and applying principled and robust methodology, we present new insights into microstructure within the preterm-born brain.

Acknowledgements

I am indebted to Seb for taking me on as a student, for his advice, and for the example he has set. I also thank Andrew: he has been generous with his time, input, and has always gone out of his way in helping me build my career.

I spent some time in Harvard, for which I thank Seb (again), Simon Warfield, Benoit Scherrer, Brian Monson, and Jeff Neil. I learned a lot, and the work was rewarding.

I have received advice, help and support from many people in CMIC including, but not limited to, Jorge, Pankaj, Marc, Sjoerd, Gary, Andre & Alex (Mendelson).

I joined the programme at a fortuitous time: I met Alex, Eliza, Felix and Mark, whom I thank for their friendship.

I also owe thanks as follows: To Alison, for inspiring strength, hilarity and ambition. To Sam, for simply being my brother. To Jassy and Sabri, for treading the path ahead of me. To Matt Taylor, for his sharpness and wit. To the residents of Toad Hall, for openness, love and support.

To Laurence, for inspiring me to aim high and push. To Tino, for being a constant source of advice, conversation and understanding — your rationality has been a guiding light. To Emma, who's been there for the PhD, and everything that came before. I love you. Finally, to my parents, to whom I owe everything. I couldn't wish for more, and have felt your love, encouragement and warmth throughout my entire life.

Contents

List of Figures

List of Tables

Chapter 1

Introduction

1.1 Context of the work

In preterm birth, an infant is delivered at fewer than 37 completed weeks of gestation, compared to full-term birth at 40 weeks. Over recent decades, rates of preterm birth have risen within developed nations [22]. Due to medical advances, infants are increasingly likely to survive preterm birth, but it remains the leading cause of neonatal mortality, and associated morbidity often persists into adulthood. Research into this population is necessary in order to predict the likelihood of specific deficits, and evaluate early intervention strategies.

Disabilities linked with preterm birth represent one of the most pressing public health concerns in Europe and the U.S.A [26]. Very preterm (VPT) infants (born at 32 weeks or fewer) are significantly more likely to suffer from cerebral palsy, cognitive deficits, loss of neuro-motor function and have long-term difficulties in education [136]. For an infant born "extremely preterm", at 25 weeks or fewer completed gestation, the rate of severe disability is 23%. This is defined as requiring assistance to perform routine, daily activities, such as walking unassisted. The rate of less severe disabilities, such as profound hearing loss, is 49% [160]. Additionally, disability implies financial costs associated with extended perinatal care, and ongoing support into adulthood [126]. Despite improvements in infant survival, the prognosis for those born preterm remains negative. Several psychological deficits cannot be measured until school age, so intervention cannot be performed in the perinatal period, or infancy. If medical imaging could be used to assess children at an early developmental stage, intervention could be recommended and tested with greater success.

Why is preterm birth associated with developmental delay and disability? One causal reason is that the event of birth occurs during a critical time for neurodevelopment. The brain is increasingly rapidly in volume, and the cortical surface folds, dramatically increasing the surface area. On the cellular level, neural afferents and glia travel radially to populate the cortex [32]. These changes cannot be imaged using conventional MRI, as the length scales of changes are orders of magnitude below currently attainable resolution. Diffusion-Weighted MRI (DW MRI) is a non-ionising, non-invasive technique that is sensitive to cytoarchitecture on the scale of microns [92].

In DW MRI, the signal is sensitised to the bulk molecular motion of water in a given direction. By sampling a variety of these directions, we establish how the water preferentially diffuses within a voxel. This diffusion depends on local conditions and so, by fitting models to the diffusion signal, we make inferences about the local microstructure. The "diffusion tensor" (DT) model fits an ellipsoid to the shape of the water diffusion [16]. In regions of homogeneous and aligned white matter, these ellipsoids are highly prolate (javelin-shaped), whereas they would be spheroidal in the cerebro-spinal fluid (CSF) where diffusion is unconstrained and isotropic. Measures such as the Fractional Anisotropy (FA) summarise properties of the tensor — in this case, how isotropic the distribution is [18]. The FA and other scalars derived from the tensor depend, in a complex way, on the local microstructure.

One example of cellular microstructure being detected with DW MRI is within the cortex. In early development, the elaboration of the radial glial cells causes a reduction in FA, as radial diffusivity decreases due to the cellular maturation [101]. Recent work has attributed the changes in DTI parameters to a general increase in complexity [14] during development. As well as these detectable changes within white matter and the cortex, changes are observed in the thalamus, a deep grey matter structure that acts as a neuronal relay centre. MRI measurements of reduced thalamic volume have been shown to correlate with later disability [11]. These differences suggest that devising non-invasive measures of growth, both in volume and microstructure, will have predictive value for future cognitive outcome. Because the consequences of preterm birth often persist into adult life, it is also likely that the adult brain has measurable differences caused by preterm birth.

1.2 Problem statement

Diffusion MRI has been used to investigate water diffusion non-invasively within tissue for decades, in both adults and infants. As diffusion imaging has become a common, if not routine, inclusion in clinical practice, advances have been made in every aspect of the acquisition — from the preparations of subjects (in particular, infants), to the resolution, and the number of directions acquired within one scanning session. This technical progress has been accompanied by a body of work on quantifying the maturation, particularly of white matter tracts, from infancy into early adulthood. Advances in imaging have enabled the invention and application of multi-compartment diffusion models. These models represent the diffusion from a voxel as coming from distinct compartments, which may be inspired by the known underlying histology. These models promise greater sensitivity and specificity to tissue microstructure.

Multi-compartment diffusion models have potential for analysing the measurable effects of preterm birth on brain development. While the diffusion tensor model has been utilised for some time in preterm research, the inherent challenges in recruiting and imaging preterm infants, and young adults, have limited the use of advanced techniques within these cohorts. However, the at-risk nature of these subject groups necessitates a sustained effort to establish early markers of disease of abnormal development. Additionally, diffusion techniques have mainly been used within white matter, with the grey matter neglected by comparison. One of the reasons for this is that the cortex is thin and convoluted, and thus partial volume is a confounding factor. Using models that account for partial volume explicitly, by using multiple compartments, would allow a more principled way to deal with partial volume, and analyse the tissue within the cortex, which may be affected by prematurity.

In this light, there is merit in applying, developing, and evaluating microstructural models of diffusion within the brains of preterm-born subjects. There are outstanding problems in selecting appropriate models of diffusion, pre-processing methodology, and the interpretation of the data.

1.3 Aims and scope of the thesis

The principal aim of this work is to investigate the use of multi-compartment diffusion models in the preterm brain. The work is carried out on MRI datasets from several,

distinct, cohorts. Because we are using novel models to represent the diffusion signal, some part of the work involves determining normative parameter values for the subject population. In addition, we aim to devise appropriate methodology to deal with the difficulties inherent to the subject population, including partial volume and low resolution.

There are limitations inherent in the presented work. Although novel imaging techniques could provide further insight into microstructural development, the scanning and recruitment paradigms were devised before this project began. Thus, the analysis uses data that were already acquired, or planned to be acquired, and further acquisition is outside the scope of the work.

Another limitation is that the imaging data cover a restricted time-span. There is only data covering the perinatal period, and early adulthood, on distinct cohorts. Where longitudinal scans have been obtained, they span a period of, at maximum, 18 weeks. Nonetheless, these two timepoints are of interest, and there remains a great deal to discover within the studied cohorts.

1.4 Structure of the thesis

Chapter 2 introduces the scientific background to the work. There is a review of the literature on brain development, which is fundamental in relating DW MRI to tissue properties and the underlying biology. We introduce several diffusion compartment models, including NODDI and DIAMOND, including their applications in preterm cohorts.

This thesis includes work performed on multiple datasets, which lends a natural structure to the work. In each part of the thesis, we first introduce the technical aspects of the dataset (for example, recruitment, cohort characteristics, and MRI acquisition), followed by the work that used the cohort in question.

We introduce the Sparks cohort in Chapter 3. This study recruited a cohort of extremely preterm-born infants, and they were imaged at up to two timepoints during their time in the NICU. Within this cohort, we investigated how a multi-compartment model (NODDI) represented the changes in white matter (Chapter 3), during the preterm period. After the white matter, in Chapter 4, we show that the NODDI model is able to detect different maturation patterns in the grey matter regions of the thalamus and

cortex, and that the microstructural parameters agree with known biology.

The analysis within these regions averaged values from all voxels identified as cortex or thalamus, for each subject. While this works well for homogeneous structures, such as the cortex, the thalamus is a relatively heterogeneous structure. To account for this heterogeneity, we developed a registration technique to use within the thalamus, using the tractography-defined anatomical regions, to map the parameters within the thalamus at 30 weeks EGA, to the term-equivalent age timepoint. Because the registration occurs within the same subject, we can assume that regions are accurately mapped, and derive parameter changes in these regions. This work is described in Chapter 5.

In thinking about the relationship between diffusion parameters and the underlying microstructure, we became aware of efforts in susceptibility-MRI to calculate the ratio of *internal axon diameter* to *myelinated axon diameter*, known as the g-ratio. This ratio is especially important in infants, as it can help quantify the myelination status during brain development. We combined multiple MRI modalities to calculate the axonal volume fraction (from a multi-compartment DW-MRI model), and the volume of myelin (from T_2-relaxometry). We thus derived an *in-vivo* measurement of the g-ratio, detailed in Chapter 6.

In Chapter 7 we investigated a different cohort of infants, in order to investigate diffusion within the cortex further. We present the use of a different multi-compartment model (DIAMOND) in order to model cortical diffusion changes in the preterm period. By combining cortical mesh generation and the diffusion processing, we quantified the "radiality" of the diffusion as a function of age and location in the cortex. To deal with the challenges of missing, partial or incomplete data, we used mixed-effects modelling. By combining these techniques, we present in Chapter 7 a quantification of the cortical "radiality index", as measured by DW MRI.

In Chapter 8, we examine the differences in brain microstructure between preterm-born young adults and term-born controls, using the NODDI model and DTI. This cohort was recruited around 20 years ago, and in early adulthood, undertook their first MRI scans. The study design also incorporated a peer-matched control group. In Chapter 9, we developed a technique to aggregate partial-volume data in a principled manner, so that accurate region-of-interest statistics could be ensured in regions such as the fornix, which is surrounded by cerebrospinal fluid.

Finally, we conclude with some closing remarks in Chapter 10, including a discussion of outstanding questions, and further work.

Chapter 2

Literature Review

2.1 Neurodevelopment in late gestation

To understand the impact of preterm birth, it is necessary to understand the neurological processes that occur in this time frame. Whereas infants have developed a functioning heart, limbs and other organs by 23 weeks of gestation, the development of the brain is very much incomplete. There is rapid neurological change immediately preceding, and during, the last trimester of pregnancy, which preterm birth disrupts.

2.1.1 Cortical Maturation

The cerebral cortex is a laminar grey matter structure that makes up the outer layers of the brain. Neural proliferation to the cortex begins from as early as the 25th embryonic day [118] and reaches a peak at 3-4 months gestation, being predominantly completed before the 24th week [156]. This migration results in the formation of the 6-layered structure of the cerebral cortex.

From 24-32 weeks, thalamacortical afferents enter the cortex, followed by callosal and cortico-cortical fibres at 32-36 weeks [156]. The surface of the brain progresses from smooth and lissencephalic to convoluted, with the formation of gyri and sulci, which is accompanied by the volume of the cerebral cortex increasing by a factor of four from 28-40 weeks post-conceptual age [156].

There is also rapid cellular change in the cortex. Radial glial cells are progenitor cells for several other types of glial cells, creating neurons, astrocytes and oligodendrocytes. Neurons are a type of post-mitotic (non-dividing) cell, and these mostly survive throughout the adult lifetime. Neurons are supported in their function by astrocytes,

another type of glial cell with a characteristic star shape. Oligodendrocytes have many roles, including generating myelin and regulating extracellular fluid. Radial glial cells also play a structural role: by spanning the width of the cortex, they act as scaffolding for neurons to migrate [27], guiding them from their origin to their position in the cerebral cortex[128]. Neurons are attached to neighbouring fibres throughout their trajectories. Neural afferents and glia travel radially along these cells, to populate the cortex [32], which progressively obscures the radial structure.

2.1.2 Thalamic Maturation

The thalamus is a deep grey matter structure that acts as a relay centre for sensory input to reach the cerebral cortex. In the preterm period, thalamo-cortical connectivity is being developed, which underpins basic cognitive processes, including the development of sensory perception [82]. The thalamus has a nuclear structure, with different nuclei being connected to different cortical regions. These nuclei are formed by 26 weeks of gestation [48]. The developmental importance of the thalamus, and the thalamo-cortical connections in particular, suggests that non-invasively measuring its volumetric and microstructural growth could have predictive value for subject outcome.

2.1.3 Maturation in the white matter

Myelin is a dielectric material that surrounds the axons of mature, healthy neurons, insulating them and increasing the speed of electrical transmission. Myelin sheaths are essential for healthy neuronal function, having a role in transmission efficiency and synchronisation of signals. Prenatally, myelin develops in the brainstem and the internal capsule, leaving the white matter predominantly unmyelinated at birth. Myelin levels rise in early childhood, and continue to rise into adulthood [112].

The sequence of human myelination was first explained using staining techniques on histological samples [29]. Myelination begins in brain regions such as the posterior limb of the internal capsule and the optic tracts. Mature axons have myelin sheaths and as such myelin is a marker for maturity, and the process of myelination is regarded as a vulnerable process in infant development [44].

2.2 Consequences of preterm birth

2.2.1 The incidence of preterm birth

Worldwide, the incidence of preterm birth was approximately 9.6% [22] in 2005. In the USA, this rate rose from 10.6% in 1990 to 11.7% in 2011 [99]. The proportion of perinatal death caused by preterm birth is estimated to be as high as 75% [63]. Although advances in medical practice and technology have caused increasing rates of infants surviving this period, associated morbidity often persists into adulthood. Disabilities linked with preterm birth are among the most pressing public health concerns in Europe and the U.S.A [26], which leads to extensive costs associated with perinatal care, and ongoing support into adulthood [126]

2.2.2 Disability and abnormalities associated with preterm birth

Very preterm (VPT) infants ($\leq$ 32 weeks completed gestation) are significantly more likely to suffer from cerebral palsy, cognitive deficits, loss of neuro-motor function, and have long-term difficulties in education [136]. Extremely preterm infants (EPT) ($\leq$ 25 weeks completed gestation) have rates of 49% for disability and 23% for severe disability [160]. These disabilities are often persistent: 86% of those assessed with severe disability in infancy have moderate or severe disability at six years of age [98].

Infants born extremely preterm have some disability in 80% of cases, as opposed to 25% for their term-born peers. While this number may seem high, "no disability" includes being free of mild hearing impairment, possessing an IQ score of $\geq$ 94 and not having asthma [98]. Research into this population is necessary in order to predict the likelihood of specific deficits and compare different early intervention strategies

Disability resulting from preterm birth is often caused by brain injury in the preterm period [156]. A combination of neuronal/axonal disease, and periventricular leukomalacia (PVL) (a white matter injury), is termed the "encephalopathy of prematurity". This is summarised in [156]. In short, white matter lesions are common in preterm infants. Neuronal/axonal injury affects not only the white matter, but also the cerebral cortex and thalamus and other regions, with thalamic neurons "commonly affected". Thalamic axonal injury is more common than in the cerebral cortex. Necroses caused by PVL can cause axonal degeneration even away from the necrotic site. This can also stunt the growth of the corpus callosum. Preterm infants have reduced thalamic

volume, especially in those with white matter injury.

In summary, preterm birth is associated with a wide range of alterations to normal brain development, which are pervasive throughout the brain.

2.2.3 The role of MRI

The high risk of adverse outcome associated with preterm birth necessitates research into the developing brain. Magnetic Resonance Imaging (MRI) is a non-ionising, non-invasive technique that allows for the investigation of tissue, *in-vivo*, with little to no risk. Within the field of MRI, there are many scanning sequences and techniques that can be used to produce scans with differing contrasts, sensitive to different biological factors. Structural scans, such as T_1-weighted and T_2-weighted scans, acquire one 3-dimensional image in a scan. These images normally have a resolution of $\sim 1\times 1\times 1 \text{mm}^3$, are acquired in a short time, and have excellent soft tissue contrast. These "conventional" MRI techniques measure the aggregate properties of voxels. More recent techniques have been developed that allow the inference of tissue properties on the cellular level, below the MRI resolution.

2.3 Diffusion-weighted MRI

Changes to the cellular environment cannot be measured using conventional MRI techniques, as the dimensions of cells are orders of magnitude below currently-attainable resolution. Diffusion-Weighted MRI (DW MRI) is a popular MRI technique that is sensitive to cytoarchitecture on the scale of microns [92].

DW MRI is sensitised to diffusion by applying magnetic field gradients in specified directions. As well as this gradient direction, the b-value is a vital parameter to characterise the scan, which quantifies the amount of diffusion-weighting. This b-value is defined as:

$$b = \gamma^2 G^2 \delta^2 (\Delta - \delta/3) \tag{2.1}$$

where γ is the gyromagnetic ratio, G is the gradient pulse amplitude, δ is the duration of the pulse, and Δ is the separation between the two pulses. The units of b are $s.mm^{-2}$. A typical acquisition consists of dozens of MRI volumes, with varying gradient directions or b-values. To make these measurements comparable across scanners,

subjects, protocol, and so forth, it is common to use models to fit the data. For parametric models of diffusion, the model's parameters can be compared on a voxel-wise basis if subjects are co-registered. It is also possible to segment regions of interest on each subject's unregistered scans. In this case, diffusion parameters are often averaged over a given region to compare tissue properties between subjects.

2.3.1 Diffusion Tensor Imaging (DTI)

In DW MRI, the "Apparent Diffusion Coefficient" (ADC) measures the diffusivity of water in each voxel. This is measured with no regard to tissue's natural anisotropy, so the measurements depend on the orientation of the subject within the scanner. Because brain tissue is anisotropic, an average diffusivity is not a good model of the signal. Diffusion signal models are used to make sense of the wealth of raw data coming from diffusion acquisitions.

A natural mathematical tool for capturing the properties of diffusion in space is a tensor. The diffusion tensor, $\mathbf{D}$, is a rank 2, symmetric, positive-definite tensor:

$$\mathbf{D} = \begin{bmatrix} D_{xx} & D_{xy} & D_{xz} \\ D_{yx} & D_{yy} & D_{yz} \\ D_{zx} & D_{zy} & D_{zz} \end{bmatrix} \tag{2.2}$$

The subscripts denote the directions of the gradient applied. A diagonal tensor is aligned with the measurement axes, with no covariance between the axes. The tensor is symmetric ($\mathbf{D}_{i,j} = \mathbf{D}_{j,i}$), because of the statistical physics of the water diffusion. Because of this symmetry, the matrix has 6 unknown values. Thus, by measuring 6 gradient directions, and one reference volume to fit the amplitude, there is enough data to fit the tensor.

The modelled signal, from the diffusion tensor model, for a given b-value and gradient direction g, is:

$$log\left(\frac{S}{S_0}\right) = -bg^T\mathbf{D}g \tag{2.3}$$

The diffusion tensor may be fit using ordinary least squares, or weighted least squares [16]. Weighted least-squares is superior for dealing with the Rician noise inherent to MRI. It is also possible to fit the tensor non-linearly, which may require

significantly more computing time.

DTI is built upon the assumption of Gaussian diffusion [75], which has mono-exponential signal decay. As technology has advanced, and *b*-values have risen, it has become clear that diffusion diverges from mono-exponential. Even a voxel with crossing fibres is non-Gaussian in its diffusion. More advanced models of the diffusion signal utilise and predict this non-Gaussianity, and these types of models are used extensively in this thesis.

There are other factors than crossing fibres which lead to non-mono-exponential diffusion. In fact, when considering the microstructural environment, it is clear that the model is too simple. In [89] the authors showed that the measured diffusion constant depends on the observation time in the acquisition (it is *b*-value-dependent), and explored the inclusion of membrane into the mathematical model. This was expanded in [148], where the authors introduced a tissue model of periodic cells with membranes, which explained some of the dependence of measured ADC on observation time. Compartment models were further explored in [145], where there were multiple compartments with individual diffusion characteristics. Much later, explicitly measuring the deviation of the diffusion signal from Gaussian has been shown to improve sensitivity to cellular change in the developing rodent brain. More examples follow in later sections. Despite these limitations, DTI has nevertheless proven to be a useful tool for diffusion MRI analysis.

2.3.1.1 Derived measures from the diffusion tensor

In order to analyse the diffusion tensor, it it standard to use rotationally-invariant indices, because these can be compared between subjects and scanning paradigms. The eigenvectors of a tensor are rotationally invariant, and so the most commonly used scalar parameters are derived from the eigenvectors. The mean diffusivity, MD, is defined as $MD = \hat{\lambda} = \frac{1}{3}\sum_{i=1}^{3}\lambda_i$, where the λ_i are the eigenvalues.

The fractional anisotropy, FA, is a dimensionless quantity, defined as:

$$FA = \sqrt{\frac{3}{2}}\frac{\sqrt{\Sigma(\lambda_i - \hat{\lambda})^2}}{\sqrt{\Sigma\lambda_i^2}} \tag{2.4}$$

The FA takes values between 0 and 1, where 0 would be totally isotropic diffusion

(ball-shaped) and 1 would be totally aligned in one direction (a stick) [17].

2.3.2 Statistical models for diffusion signal

Yablonskiy et al [162] introduced a compartment model where each tissue has an apparent diffusion coefficient (ADC) that has both a mean, and a distribution width. A voxel's signal in this model comes from several tissue components within the voxel, each diffusing isotropically with a tissue-specific ADC. This can account for non-Gaussianity within the measured signal, which in this study is found to exist in all tissue in the brain.

Similarly to adding tissue compartments, the bi-exponential model is an extension of the single tensor model, to fit to the non-Gaussian signal that is exhibited at higher b-values. The signal estimate for the bi-exponential distribution is given by:

$$\frac{S}{S_0} = v_f e^{-\mathbf{D}_f b} + v_s e^{-\mathbf{D}_s b} \tag{2.5}$$

Where $\mathbf{D}$ is the diffusion tensor, S_0 is the signal from the compartment with no diffusion weighting, and the v are the volume fractions of the (f)ast and (s)low compartments. This can be fitted by non-linear least squares. This technique has been used in the cortex and deep grey matter [97] with a CSF-suppressed diffusion acquisition, which mapped the fraction of fast/slow diffusion for white and grey matter. Here, this model was found to be the most complex that was supported by the data.

Another model for non-Gaussian diffusion is Diffusion Kurtosis Imaging (DKI). This, in common with other more mathematically-inspired models, makes no assumptions about the microstructure — it does not assume multiple compartments exist within a voxel. The approach works by measuring the deviation from Gaussian diffusion. DKI requires two or more diffusion-weighted shells, in addition to a b=0 volume. The kurtosis model is able to accurately and robustly estimate its parameters and has been used in many recent imaging studies, including of the developing brain [125].

2.3.3 Biophysical compartment models

Statistical models for water diffusion, including the diffusion tensor, can be challenging to interpret in terms of the underlying microstructure. For instance, low fractional anisotropy can be attributed to lack of myelin, fibre-thinning, edema or fibres cross-

ing [74]. Biophysical compartment models represent the signal as a linear combination of diffusion signals, coming from distinct microstructural environments.

In biophysical compartment models, the mathematical properties of the elements used to model the signal are inspired by the underlying microstructural environment. For example, a diffusion sphere, with fixed diffusivity, may represent a free-water component. One of the first bio-physical models for the diffusion signal [145] was introduced for diffusion in a bovine optic nerve. The model includes a signal for plasma, exchange of water between compartments and a model for intra-cellular diffusion in red blood cells. This is a compartment model that uses multiple b-value "shells" to investigate microstructural environment. These models are based on the underlying structure of the tissue and so interpretation should be more straightforward than, for example, the tensor model.

Other models have simplified some of the assumptions — for example, by ignoring exchange. In the "Composite Hindered And Restricted Model of Diffusion" (CHARMED) model, compartments include intra- and extra-axonal spaces [8]. These models tend to require a thorough diffusion acquisition at high angular resolution and a wide range of b-values. This technique required over 15 minutes of acquisition in the original work, and has a minimum of 12 parameters to fit. More recent models have simplified the assumptions further, in an attempt to derive meaningful parameters from a more sparse data acquisition.

2.3.4 The Neurite Orientation Dispersion and Density Imaging model (NODDI)

NODDI [165] is a multi-compartment microstructural model for multi-shell diffusion data. The model can be fitted with two distinct b-values of acquisition, or 'shells', of diffusion data. In NODDI, the diffusion signal is divided into signal from compartments of volume fraction v_{iso}, v_i and v_e. The isotropic volume fraction, v_{iso}, represents water diffusing isotropically with the diffusivity of free water, as in the fluid-filled ventricles or the cerebrospinal fluid. The intra-neurite volume fraction, v_i, represents how much of the remaining space is occupied by the neurites. Water diffuses preferentially along the length of the neurites. As well as defining the angles of anisotropy, this compartment is dispersed by an amount determined by the Orientation Dispersion Index (ODI), which

varies between 0 (stick-like diffusion with complete alignment) and 1 (isotropic, ball-like diffusion). Finally, the extra-neurite environment, v_e, is categorised by diffusion hindered perpendicular to the neurites. Because NODDI requires only two shells of diffusion data, the acquisition can be conducted in clinically-viable times, even for neonates.

In addition to the volume fractions, there are also two free angles that must be fitted. The signal, S(*bval* = b,*bvec* = **g**), is given by:

$$S = v_{iso}S_{iso} + (1 - v_{iso})(v_i S_i + (1 - v_i)S_e) \tag{2.6}$$

In the isotropic volume fraction, v_{iso}, water diffuses isotropically with a diffusivity of $d_{iso} = 3.00\times10^{-3} mm^2 s^{-1}$, the value for free water. $S_{iso} = exp(-b * d_{iso})$. The remaining volume is divided into v_i and $(1 - v_i) = v_e$: respectively, the volume fractions of intra- and extra-neurite compartments. Diffusion in neurites is modelled with cylinders of zero radius with diffusivity in the axial direction fixed at $d_i = 1.70 \times 10^{-3} mm^2 s^{-1}$ in adults, and $2.00 \times 10^{-3} mms^2 s^{-1}$ in neonates [87]. The sticks are dispersed by a Watson distribution as in [164], with the orientation dispersion index ($0 \leq \text{ODI} \leq 1$) representing how dispersed this diffusion is. $S_i = \int_{S^2} f(\mathbf{n}) e^{-b_{\|}(\mathbf{g}.\mathbf{n})^2} d\mathbf{n}$ where $f(\mathbf{n})$ is given by the Watson distribution: $f(\mathbf{n}) = M\left(\frac{1}{2}, \frac{3}{2}, \kappa\right)^{-1} e^{\kappa(\mu.\mathbf{n})^2}$, where M is a confluent hypergeometric function and μ is the mean orientation. κ is related to the ODI as $\kappa = 1/tan\frac{\pi * ODI}{2}$.

The extra-neurite volume fraction, v_e, uses an anisotropic Gaussian diffusion model to represent the space around the neurites. This represents the water being hindered by the presence of neurites, preferentially diffusing parallel to them. It is also dispersed by the ODI. $log(S_e) = -b\mathbf{g}^T \left(\int_{S^2} f(\mathbf{n}) D(\mathbf{n}) d\mathbf{n}\right) \mathbf{g}$.

The signal in NODDI, and compartment models in general, is the linear sum of signals from the different compartments that are present. Whereas conventional fitting techniques optimise the model parameters on a per-voxel basis through a non-linear fit, it is possible to greatly increase the efficiency of the calculation using sparse modelling. This works by using a 'dictionary' of pre-computed signals at a range of angles. The sparse solver chooses a small subset of these signals that combine to represent the measured signal. This is up to four orders of magnitude faster than the original im-

plementation [43]. This increase in speed is not accompanied by an improvement in the model-fitting — the performance tends to be no better than the standard NODDI implementation, so this approach is mainly useful when dealing with extremely large datasets.

2.3.5 Information theory and compartment modelling

It is possible to combine a wide variety of compartments to represent the diffusion signal. There are numerous options for model compartments, ranging from the tensor, ball and stick to more exotic models (e.g. the zeppelin). The wide variety of common model components is summarised in [121]. One method of choosing model compartments could be by choosing based on proximity to some hypothesis, relating to the underlying biology. It could also be done by using a data-driven approach, using an information-theoretic measure to derive which model fits best, as in [60].

In light of these options, it may be useful to build a compartment model in which the data itself influences the choice of modelled compartments. This can be implemented with nested, or hierarchical, models. The 'DIstribution of Anisotropic MicrOstructural eNvironments in Diffusion-compartment imaging' (DIAMOND) [137] model takes this approach, in order to best model the signal within a voxel by also optimising the number of compartments present. DIAMOND permits the compartments to take user-specified forms, for example, a tensor or a stick. For the case of a tensor, these compartments have their own associated FA and MD values. One theoretical reason for using multiple anisotropic compartments within a voxel is the fact that many, if not most, voxels within the brain contain crossing fibres [74].

Measuring the microstructural parameters on a per-compartment basis is now relatively common. The spherical mean technique (SMT) [79] uses clinically-viable diffusion techniques to estimate the microscopic diffusion properties of white matter. This method relies on the fact that the spherical mean of the signal over all gradient directions is independent of how neurites are distributed. The measurement depends *only* on microscopic diffusion processes.

Neither DIAMOND, nor SMT, fix parameters such as the intra-cellular diffusivity, or the free-water diffusivity, in contrast to the NODDI model. In addition, these techniques explicitly model geometries such as crossing fibres, whereas NODDI does

not. However, despite these benefits, there is a paucity of work linking the parameters to observed or theorised histology, and the parameters are more difficult to link to the microstructure.

2.4 Multi-modal compartment models

With the ability of compartment models, such as NODDI, to estimate biological tissue fractions *in-vivo* from diffusion data, it has been an area of active investigation to combine these measurements with information from other MR modalities. Complementary information from differing modalities may utilise the microstructural sensitivity of DW MRI in tandem with the myelin sensitivity of T_2 measurements, for example.

Myelin is close-to-invisible with diffusion MRI, thanks to the extremely short T_2 of the water molecules trapped between the layers of the myelin sheaths. Using T_2 relaxometry allows inference of the distribution of T_2 values in a voxel, and the proportion of the tissue that has each value [127]. By assuming that myelin-bound water accounts for the lowest T_2 values, we can estimate volume fractions of myelin within a voxel.

By combining the axonal volume fraction with the amount of myelin in the voxel, with some simplifying assumptions, it is possible to calculate the ratio of (the inner axonal diameter):(the total diameter of axon + myelin), the *g-ratio*. This has been performed with NODDI and differing myelin-mapping procedures — MCDespot [46], T_2-relaxometry [105] and magnetisation transfer [146]. Because the myelination per axon is more clinically relevant than the bulk quantity of myelin, the *g*-ratio is of interest.

2.5 MRI findings in the preterm population

Disability in the preterm population is very common, with a heterogeneous range of effects. While some deficits present immediately, some only becoming apparent at the start of formal schooling. If it were possible to predict these in early life, it would allow for improved targeting of early intervention and improved prognostication. Quantitative MRI has the potential to provide early markers of cognitive and physical health, which would aid in developing treatment for this group. MRI has made contributions to understanding the preterm brain from early life through to young adulthood. Following

is a brief review of the literature that covers these periods, which are most relevant to the thesis.

For MRI acquired around the time of birth, there are distinct logistical challenges. Subjects are prone to motion, require specialist care, and their brains are far smaller than for adults. Infant-scanning often uses feeding, wrapping and/or sedating infants to achieve good scan quality [100]. Infants require enhanced protection from the loud noises an MRI machine creates, with earbuds, earmuffs and large headphones deployed in order to appropriately dampen the sound. The invention of MR-compatible incubators (e.g. [144]) has made it easier to provide for the complex needs of a premature infant during a scan, although these incubators are costly and uncommon in use. Because of these difficulties, imaging protocols in infants tend to lag their adoption in adults.

Preterm brains have a range of differences from their term-born equivalents. Periventricular leukomalacia (PVL) is common in preterms, accompanied by neuronal/axonal disease. This affects many areas in the brain. This is hypothesised to account for the majority of the neurological effects of prematurity [156].

Preterm brains display common radiological findings of punctate white matter lesions, dilated ventricles, and diffusion extra-high signal intensity (DEHSI). Lesions and dilation are associated with developmental delay [45], while DEHSI does not have strong correlation with deficits. Differences persist in adulthood: FA is lower [58] in major white matter tracts. This difference from healthy controls is proportional to the number of days spent on a mechanical ventilator in infancy. Brain volume differences persist: preterm-born adolescents also have decreased brain volumes and increased size of ventricles [115].

2.5.1 Diffusion Tensor Imaging

DTI has been used extensively to investigate the brains of preterm infants. Hüppi et al published a review on its use in analysing brain maturation in infancy [72]. While white matter DTI parameter values are changing during myelination, there is a two-step sequence of parameters changing *before* the histological appearance of myelin, and then continuing to change *during* myelination. The changes in the *pre*-myelinating period may be due to changes in axon caliber. Regions such as the corpus callosum —

that are not due to myelinate until significantly after birth — may nevertheless show signs of pre-myelination in DTI. The interpretation of DTI parameters is not wholly specific [77]. Similar parameter trajectories may be interpreted as evidence for different maturational processes depending on the brain region.

There are a number of markers of preterm birth that have been found with DTI, some of which are summarised in [110]. These include preterm infants having lower FA in several regions than term-born peers imaged at the same overall gestational age. Infants born at fewer than 28 weeks have more extreme decreases in FA [6]. Rose et al showed that "very preterm" infants tended to have lower FA values than preterm, which were lower in turn than term, in several white matter regions [130].

Tract-Based Spatial Statistics (TBSS) [140] is a skeletonisation technique that allows white matter comparison between groups. Ball et al [12] used an infant-optimised version of TBSS to show a large effect of prematurity, with preterm infants having lower FA values in most of the white matter. The alteration in FA value in preterm subjects was more extreme in infants with greater past exposure to respiratory support, which demonstrates that events in the perinatal period have a persistent impact on DTI measures.

2.5.2 Predicting clinical outcomes with DTI

Differences in preterm and term DW MRI may correlate with future cognitive health, and such measurements would have significant clinical utility. Non-invasive, early measurements would allow interventions to be developed and tested in early life.

Neonatal FA values near birth are associated with early mathematics ability at 5 years of age, and working memory at 7 years, when used in tandem with volumetry [152]. This work did not recruit sufficient controls to investigate these predictive trends in healthy controls. In the term controls that *were* recruited, there was no evidence that the same associations were observed, which the authors attributed to specificity of their method to the preterm group. Another predictive measurement for cognition is described in [13]. This work evaluates the level of thalamo-cortical connectivity, and finds that this correlates with cognitive scores at a later timepoint. In this paper, there was no control cohort, so their analysis is also specific to the preterm cohort. Chau et al [36] associate abnormal development, as measured with DW MRI, with

adverse clinical outcome. In both white matter tracts and the basal nuclei, higher cognitive impairment was linked to a slower increase in FA. Children with severe language impairment had lower FA in white matter tracts.

A review on white matter development in infancy, [52] showed that differences between preterm and term DW MRI scans were predominantly in FA measurements, as opposed to MD, with few white matter approaches showing success in predicting cognition within the preterm cohort. An exception to this is a study investigating TBSS in a cohort of 63 preterm infants [154] . Within this cohort, increased FA values within the corpus callosum (CC) were predictive of higher cognitive scores at two years of age. This study corrected for gestational age at birth and age at scan, but did not include confounds of intra-cranial volume, or the size of white matter tracts. The size of a region, in particular, may change the FA measurements without necessarily being representative of a change in the underlying microstructure. Nevertheless, the CC is one of the better-studied regions of interest and its link with cognition is plausible. In adults born with very low birthweight (most commonly associated with preterm delivery), there are widespread reductions in FA through many of the tracts [58] as determined by TBSS.

As we can see from these studies, while there are definite correlates between MR measurements and later outcome, the predictive power of these is relatively low. Additionally, the findings of specific regions of interest do not tend to generalise well between papers. The lack of concordance between papers is well-summarised in the review by Ment et al [110], and that general trend still continues.

2.5.3 Myelin and MRI

Because myelination is affected by preterm birth, measuring the myelin levels was an early target for MR studies. Barkovich et al [15] found that T_2-weighted sequences correspond to the temporal sequences of brain myelination and are thus useable as surrogates for myelination status. However, the quantification of this observation is an ongoing challenge.

Early in the development of DTI, it was assumed that the FA would depend on the myelination status. It was proposed that diffusion anisotropy was generated by water being hindered in a radial direction (perpendicular to the axon) by the hydrophobic

myelin. However, studies on Shiverer mice, a breed of dysmyelinated mice, and other unmyelinated nerve fibres, have shown that FA is not specific to myelin's presence [9, 21]. While myelin may decrease the radial diffusivity, the packing density of the fibres also changes during myelination, which confounds DW MRI interpretation.

There are observations in diffusion MRI that correspond to a "pre-myelinating" phase [159], before the histological appearance of myelin.

Water trapped in the hydrophobic myelin layers has short relaxation times. These short relaxation times mean that DW MRI is not sensitive to signal from these regions, but T_2 methods may be. By performing T_2-relaxometry, in which multiple T_2 values are measured, a multi-component signal model can be used to estimate the distribution of the T_2 values within a voxel. By assuming that low relaxation times are caused by water trapped in myelin, we can estimate the fraction of a voxel that is taken up by myelin. This measurement has been found to correlate with the percentage of myelin histologically [91, 90]. T_2-relaxometry has also been validated in an MR phantom and used to map the development of perinatal myelin [104].

2.5.4 Using compartment models of DW MRI

The NODDI model has been used to investigate the white matter of infants shortly after full-term birth [87]. This paper showed that the maturation state of different white matter regions could be quantified by using the NODDI parameters, in conjunction with the FA measurements. The authors also fit a model inspired by CHARMED, "CHARMED-light", which had some simplifying assumptions for use in infant data. This model did not fit the data as well as the NODDI model. Counsell et al have demonstrated NODDI parameter changes in the thalamus during early infancy [42], with increasing v_i being attributed to pre-myelinating events. In humans, this is seen as a decrease in the average diffusivity, without a change in the FA. Subsequent events, including actual myelination and membrane proliferation, does bring an increase in FA [52]. Over the perinatal period, myelin is absent in most of the white matter, so the FA changes that are observed may relate (not exclusively) to pre-myelination.

Nossin-Manor et al [116] used Magnetisation Transfer Ratio, DTI and T_1 scans to attempt to investigate myelination more thoroughly. MTR was chosen because of its relationship with myelin content. However, in their study, they found that MTR

parameters were also sensitive to the density of other axonal components (including neurofilaments and microtubules), and thus the technique was not specific to myelin alone.

2.5.5 Measuring microstructure and morphology in the cortex

The findings of McKinstry et al [101] helped to highlight the potential of diffusion imaging for investigating neuronal structures. They investigated cortical development using diffusion MRI, and in particular, the primary diffusion direction. They showed that the infant's cortical structure is aligned radially during the pre-term window (26-36 weeks EGA), and that this radiality diminishes rapidly. In this same time period, other transient structures were segmented by using diffusion tensor imaging in infants born at 24 and 25 weeks gestation [95].

Within cortical grey matter, the FA value depends on the cortical depth [151], measured *in-vivo* in human subjects. Fixed tissue has been used to investigate the region-specific microstructure [1]. This work found common patterns in FA mapped as a function of cortical depth for different subjects, and that these profiles were different for the primary motor and primary somatosensory cortices (among others). While this level of detail is not feasible in *in-vivo* studies, this study shows the potential of diffusion-weighted MRI for investigating the cortex.

Trivedi et al [150] used DTI with post-mortem foetuses to investigate how FA changes in the cortex as a function of gestational age. The FA rises with age in the occipital, parietal, temporal and frontal lobes before reaching a peak and declining. The time and maximum value of that peak depend on the lobe, with FA peaking latest in the temporal lobes. They also analysed protein expression from tissue samples to show that this change in diffusion parameters was related to the migration of neuronal cells from the germinal zone. In terms of microstructure, the increasing FA is linked to the formation of radial glial cells, and the decrease is linked to the growth of dendrites. The rate of microstructural maturation correlates with psychological development at 2 years of age [14], with this paper also showing regionally-dependent rates of FA and MD change for preterm infants.

These studies represent a blossoming interest in cortical microstructure as measured by diffusion imaging. However, the use of multi-compartment models has not

been widely adopted or investigated. The utility of diffusion measurements as markers of health is still an active area of interest.

There is evidence that in brain development, the thickness of the cortex depends on the underlying white matter microstructure as measured with DTI [73]. This paper found that in childhood and early adulthood, the cortex thins and the underlying white matter correspondingly increases in FA. This connection between cortical grey matter and the white matter underlying it is also observed in very preterm infants [142]. Here, the authors found that the maturation rates depended on the cortical region (in this case, hand-labelled regions, including the primary motor cortex or the prefrontal area). The relative rates of parameter change in cortical grey matter and its associated white matter had a region-specific pattern in the cortex.

The morphology of the cortical surface is affected by some genetic diseases, such as Williams syndrome [59]. However, cortex- and lobe-wide measurements of folding were unable to distinguish diseased, preterm-born cortex from term-born [138], even with testing 22 distinct measures. Instead, gyrification index and sulcal depth were able to separate these groups. While this study did not find that a global measure of cortical morphology was a good marker of brain injury, the brains marked as injured did not have a common phenotype. Even though this work could not distinguish diseased from healthy brains, it may still be possible to subtype diseased subjects with this type of analysis. Indeed, the sulcation ratio varies over the cortical surface [108], and white matter connectivity, measured with tractography, correlates with the sulcation ratio of the cortical surface which it underlies.

2.5.6 Quantifying the 'Radiality Index' in the cortex

While the cortex has underlying anisotropy in its structure for adults, it wasn't until the advent of parallel imaging, with high acceleration factors, that this could be measured *in-vivo* [70]. The FA values in the cortex are between 0.05 and 0.20, but the direction is noticeably radial. This radiality was found to depend on the region of the cortex [7], with diffusion in the crowns of gyri oriented normally to the cortical surface compared with the sulcal folds. The motor cortex in particular showed higher radiality than other regions. The radiality was calculated using a cortical surface mesh to compute the normal direction to the cortex, and DTI, to establish the principal eigenvector for diffusion.

The radiality is defined as the inner product of the two. Radiality has been measured in the newborn infant, showing higher radiality in anterior than posterior regions [107].

Adult cortical radiality has been further explored in [103], studying *in-vivo* and fixed human tissue, and the cortex of an anaesthetised macaque. They again found that the motor cortex had particularly high radiality values. Radiality and FA did not have a strong correlation, which suggests that the radiality was not caused by cortex/white matter partial volume.

2.6 Partial volume in DW MRI

2.6.1 The confound of partial volume

DW MRI commonly uses voxels of roughly 2.5mm in dimension, significantly larger than for structural scans, meaning that partial volume (PV) is a common artefact in some anatomical regions. Diffusion parameters are commonly reported after being averaged across a region-of-interest, for instance in [143, 129, 149]. A given diffusion parameter is averaged over a given neuroanatomical structure. For some large, contiguous, regions, partial volume may have little effect, as there are many voxels that are entirely within the given region to analyse. However, preterm brains are smaller than their term-born peers at all points in the lifetime, and thus even in these regions, not accounting for PV may bias the measurements.

The ROI-based approach allows for parameter values in anatomical regions to be compared against each other. These methods rely on high-quality segmentation to ensure that regions of interest correspond to each other. While these are useful in regions that are large, the averaging effect of looking at a large region is a downside, if the differences we seek are more subtle. For instance, the corpus callosum is often broken down into smaller regions as in [62] in order for effects to be localised. These sub-regions may be informed by neuroanatomical prior knowledge. It is also possible to derive regions from the data itself, using clustering algorithms, as in [135].

The partial volume effects of the CSF, when it neighbours white matter, can artifactually influence the measurements [157]. During development, if partial volume is ignored, the increasing size of a region may in itself cause FA changes that have nothing to do with microstructure. The diffusion parameters within structures such as the fornix — a narrow white matter structure, surrounded by cerebrospinal fluid — might

not be measured well by this approach, especially at typical diffusion resolutions [111]. Because of the large scale of diffusion MRI voxels relative to the fornix many, and perhaps all, voxels will contain partial volume. This partial volume affects the ability to interpret the parameters of diffusion parameter models. For instance, the size of the fornix may confound parameter estimation by introducing varying amounts of partial volume in different subjects or at different timepoints (for example, due to atrophy). In order for the measured diffusion parameters to accurately represent microstructure, we must remove the confound of partial volume.

2.6.2 Existing correction techniques for partial volume

Partial volume is particularly problematic with CSF, especially in the cortex. One method of dealing with this is to use a fluid-attenuated diffusion scan, as in [14]. Here, this was used to validate that measurements of cortical grey matter diffusion parameters were unchanged when free water was included. These hardware techniques need building into the pipeline at an early stage, and cannot be applied retrospectively.

There are also techniques for removing the impact of free water from a scan computationally. "Free Water Elimination" (FWE) [124] was developed to remove the impact of free water from a scan with only one b-value. This technique fits a model of a free-water component (isotropic, with a set diffusivity) and a free tensor compartment. This model was further verified in [111]. One of the reasons for using only one b-value is the increase in scan time with more b-values. However, since this time, multi-shell diffusion imaging has become more common. Multiple b-values allow for the inference of compartments with different diffusivities on a per-voxel basis, without requiring the spatial regularisation of FWE.

Another potential technique is to use super-resolution, to estimate higher-resolution data from lower. For true super-resolution, small regions would then be resolvable without the partial volume. 'Image Quality Transfer' [5] uses high-resolution data from the "Human Connectome Project" (HCP) [153] to train the prediction of a higher-resolution scan from lower-resolution. The approach is also used to infer parameter maps of the NODDI model from a single-shell of diffusion. This is important for analysing older datasets. A model-based super-resolution of DW MRI was proposed in [155]. Despite some successes with these techniques, it is by no means a

solved problem. Validation is especially lacking in subject populations, who may have heterogeneities that confound the process.

2.7 Longitudinal studies

Some of the cohorts studied in this thesis have been followed over time, having imaging and psychological data from multiple timepoints. The advantage of longitudinal scanning is that it allows the inference of per-subject confounds, which is especially important in such a heterogeneous population as preterm subjects. This lack of independence between measurements needs accounting for in any statistical analysis.

2.7.1 Linear mixed-effects models

Mixed-effects models incorporate both fixed and random effects. Fixed effects quantify the population-average parameters of a model. Random effects depend on the subject and allow the model parameters to vary per-subject. An early example of linear mixed-effects models, utilised on an infant population, is in [123], where the authors showed that the FA was the most effective DTI measurement at discriminating between tracts in the infant. They established this by performing paired tests on the fixed effects.

Using paired tests can also help with regional discrimination on the surface of the cortex, as in [28]. In this paper, the authors registered cortical surfaces into a common space, before fitting mixed-effects models to patches of the cortex. These regions were generated by the data. This showed that the utility of linear mixed-effects models could be extended beyond summary statistics on a region, and into mapping values intuitively, over a region. Of course, it is also possible to use the models on summary measures of parameters. This technique relies upon a good registration between the surfaces of subjects. The folding cortex in the preterm infant population, and heterogeneity in general, means it is much harder to establish correspondence between surfaces than for mature brains.

2.7.2 Non-linear mixed-effects models

Mixed-effects models may be extended to use a non-linear function. For example, growth curves are intuitively non-linear, as the rate of growth tends to zero during development. This type of modelling has been used to build normative curves for neurodevelopment, using DTI [133, 132].

In [133], the authors quantify the rate, delay and asymptote of a Gompertz function, for maturation within the white matter in the developing brain. By using this statistical formulation, they quantified both subject-specific and population curves. In addition to popularising this technique, they showed that the parameters of the curves were significantly different between different regions in the brain.

Young et al. used both non-linear and linear mixed-effects models to study the maturation of preterm subjects from birth until four years of age [163]. They found no effect of sex in any analysis, or of GA at birth (range:24-32 weeks). This is surprising, given previous findings of earlier birth leading to worse outcomes.

Both linear and non-linear mixed effects models have, therefore, been used successfully in preterm imaging. Because of the longitudinal nature of some of the datasets presented, these effects will be useful in removing the confound of correlation between subjects imaged multiple times.

Chapter 3

Measuring white matter microstructure in the preterm period

3.1 The Sparks Project

The Sparks Charity (Registered Charity #1003825) exists to fund pioneering children's medical research. This charity issued a grant to fund an investigation into brain development in the preterm period using MRI. This provided resources to recruit up to 50 preterm subjects to be scanned at two timepoints: once when stable after birth, and once more at term equivalent age (40 weeks estimated gestational age). These infants were to be followed into early childhood, with regular psychological evaluations occurring until two years of age, with the aim of discovering any indicators of future health status provided by the scans taken during the perinatal period. The infants underwent the same set of scans at term and preterm timepoints. Between the two timepoints of scanning, there is a broad range of maturation on the micro- and macro-structural level within the infant brain.

3.2 MRI acquisition

Infants were excluded if they had abnormal cerebral ultrasound, or if either the diffusion acquisition or the structural acquisition was unusable due to patient movement. Informed parental consent was obtained for all infants and the study was approved by the local research ethics committee.

MRI data was acquired on a Philips Achieva 3T MRI machine. The infants were imaged when spontaneously asleep after feeding, without sedation, in an MR-

compatible incubator with a neonatal specific head coil (lmt-medicalsystems.com). Informed parental consent was obtained for all infants and the study was approved by the local research ethics committee.

The T_1-weighted scans used a 3D MP-RAGE at a resolution of 0.82x0.97x1.0 mm^3 (reconstructed to 0.82 x0.82 x0.5 mm^3) at TR/TE =17/4.6ms, acquisition duration 462s. The diffusion-weighted sequence had 54 diffusion directions: 6 reference volumes at b = 0 smm^{-2}, 16 at b = 750smm^{-2} and 32 at b = 2000smm^{-2}. Resolution was acquired at 2.0x2.0x2.0mm and reconstructed to 1.75x1.75x2.00 mm^3. T_R was 9s and T_E was 60ms, with a total acquisition time of 703s.

Because of the level of subject movement, it was necessary to use a scanning sequence that is economical in terms of time. Our two-shell diffusion sequence is performed over a short timescale and thus is suitable for this population.

3.3 Overview

Adverse outcome in the preterm population is associated with white matter damage as revealed by DW MRI and DTI. However, a particular value of a DT parameter such as FA or MD can represent a range of microstructural conditions. The NODDI model is a multi-compartment, biophysical model, that uses data from multiple diffusion "shells" to fit parameters relating to geometric properties and neurite density [165]. This model has been used within the infant brain at term [87], and this approach shows greater specificity than the DT model [165]. Kelly et al showed that 7 year-olds born preterm have lower FA and higher ODI than term-born controls [80], with neonatal brain abnormalities predicting these characteristics. These children showed no abnormality in axon density.

Using NODDI parameters, we investigate how microstructure changes in white matter regions of interest for VPT infants during the preterm period. These infants were recruited as part of the SPARKS cohort (see Section 3). The specificity of NODDI parameters may help to determine imaging biomarkers of cognitive health, and facilitate earlier and more effective therapeutic intervention. The longitudinal nature of the scans allows us to establish normative NODDI values for the preterm period. Total

3.3.1 Contribution

Work in this chapter formed the basis of an abstract, presented at ISMRM, 2014 as a poster (Appendix B.3, [11]).

3.4 Methods

3.4.1 Data Collection and Processing

The data was acquired as described in Section 3.2. We removed motion-corrupted volumes and eddy-current corrected the remaining data, rotating the b-vectors and modulating by the expansion/contraction of the transformation [76]. We fitted the diffusion tensor using non-linear least squares [3]. For this Chapter, we had usable scan data from 13 infants. There were 21 scans collected. Two were discarded due to subject motion, leaving 6 longitudinal datasets and 7 single-timepoint scans (5 at term).

To segment the brain images, we use a neonatal atlas [117] with 122 regions. We used the FA maps for each subject to register to the atlas, initialising with an affine transform. For the non-rigid transformation, we used a b-spline registration technique implemented in niftyreg [113], using normalised mutual information as the cost measure. We applied this single non-rigid transformation to all of the other diffusion parameter maps (NODDI and DTI).

From this labelling of the regions of interest, we compute the mean of each parameter, in each region. The atlas also labels the tract system for each region. The region names that we use in this study, and their abbreviations, are listed in Table 3.1, along with the tract membership.

3.4.2 Fitting the NODDI model

We fitted the model by non-linear least squares after initialising using the diffusion tensor model and a grid search, using the NODDI Matlab Toolbox [1].

NODDI has similarities with the CHARMED model, such as the volume fractions. While CHARMED has a minimum of twelve free parameters per voxel [8], a reduced version, CHARMED-light, has been proposed and compared with the NODDI model's parameter estimates. The volume fractions were similar in the white matter of neonates [87]. The NODDI model has the advantage of modelling grey and white

[1] http://www.nitrc.org/projects/noddi_toolbox

Abbreviation	Region Name	Tract
ACR	Anterior corona radiata	Projection
ALIC	Anterior limb of internal capsule	Projection
Cau	Caudate nucleus	Deep Grey Matter
CC	Corpus callosum	Commissural
CGC	Cingulum cingular part	Limbic
CGH	Cingulum hippocampal part	Limbic
CP	Cerebral peduncle	Projection
EC	External capsule	Association
Fx	Fornix	Limbic
GP	Globus pallidus	Deep Grey Matter
IFO	Inferior fronto-occipital fasciculus	Association
PCR	Posterior corona radiata	Projection
PLIC	Posterior limb of internal capsule	Projection
PTR	Posterior thalamic radiation	Projection
Put	Putamen	Deep Grey Matter
RLIC	Retrolenticular part of internal capsule	Projection
SCR	Sagittal stratum	Projection
SFO	Stria terminalis	Association
SLF	Superior corona radiata	Association
SS	Superior fronto-occipital fasciculus	Projection
ST	Superior longitudinal fasciculus	Limbic
TAP	Tapetum	Commissural
Thal	Thalamus	Deep Grey Matter
UNC	Uncinate fasciculus	Association

Table 3.1: This table displays the abbreviation, the region name, and the tract that the region is in. Deep grey matter also features, as a comparison.

matter, and has added information about the dispersion in the diffusion. These measurements may highlight the dynamics of cortical and other grey matter maturation. This unified model for brain tissue is suited to the quickly changing microstructural landscape of the infant brain.

3.4.3 Statistical Analysis

We first computed the mean for each parameter in each region, we plotted these values both as functions of age. We also plotted values as functions of other parameters, in order to investigate clustering patterns within the data.

In this chapter, we aim to test for regional differences using pairwise testing of the NODDI and DTI models. In [87], differences are established between two regions using t-tests. However, for longitudinal data, with some subjects having multiple scans, this approach must be modified. DTI has been investigated on a longitudinal basis

in preterm infants, employing mixed-effects models [123]. We propose fitting nested models to the two regions of interest, and then using an analysis of variance to determine the best of these hierarchical models. This will be performed for each pair of regions. The motivation behind this approach is to add model complexity, and evaluate whether this added complexity helps fit the data, in terms of some information criterion. This determines the model with the best trade-off between fitting the data, and having an appropriate number of parameters.

For each pair of regions in the brain, we fit the following models. We use R-like notation for describing the models. $\sim$ means "depends on", $(1|ID)$ is a random intercept that depends on the subject (this random effect accounts for intra-subject correlation).

1. $parameter \sim (1|ID)$: This model fits a constant that depends on the subject being examined. There are no terms that depend on gestational age, or the regional interest.

2. $parameter \sim t + (1|ID)$: there is a dependence on gestational age, but the regions cannot be distinguished.

3. $parameter \sim Region + (1|ID)$: the regions have different parameter means, but neither shows a time-dependence.

4. $parameter \sim t + Region + (1|ID)$: the regions are separable, and there is a time dependence, but the time-dependence is the same for both regions.

5. $parameter \sim t * Region + (1|ID)$: the regions have different slopes and values.

This was implemented using R version 3.2.1 (2015-06-18) – "World-Famous Astronaut", using the "lme4" library [19]. We recorded the model with the lowest AIC for each pair of regions, and plotted the results in a grid.

It would be surprising if models 1 or 3 were chosen often, because they are independent of time. The microstructure and diffusion parameters are changing throughout the brain over the time period of this experiment. Model 2 would suggest that the regions have identical time-courses, and no differences between the regions. This is also unlikely, given the findings of [123]. We therefore mainly expect to see models 4 and 5.

3.4.4 Laterality of ROI measurements

Because regions of interest are on both hemispheres of the brain, we could test for an effect of 'hemisphere' by including it as a variable in the above equations. However, as a preliminary investigation, we used t-tests to establish whether differences between hemispheres were significant, accounting for multiple comparisons. We found that there were no significant differences, and so we combined hemispheres prior to the above testing.

3.5 Results

3.5.1 Longitudinal parameter changes in the white matter

We successfully implemented the pre-processing, data processing and quality control. The scans were inspected visually for registration to the atlas template, and we found that the registration was performed successfully. An example of the T_1-weighted and diffusion parameters for one infant are shown in Figure 3.1.

We plot the changes in parameter values over time in Figure 3.2. In the white matter regions, the FA increases while MD decreases. In the NODDI model, the v_{iso} remains relatively low in most tracts, while the v_i increases and ODI decreases.

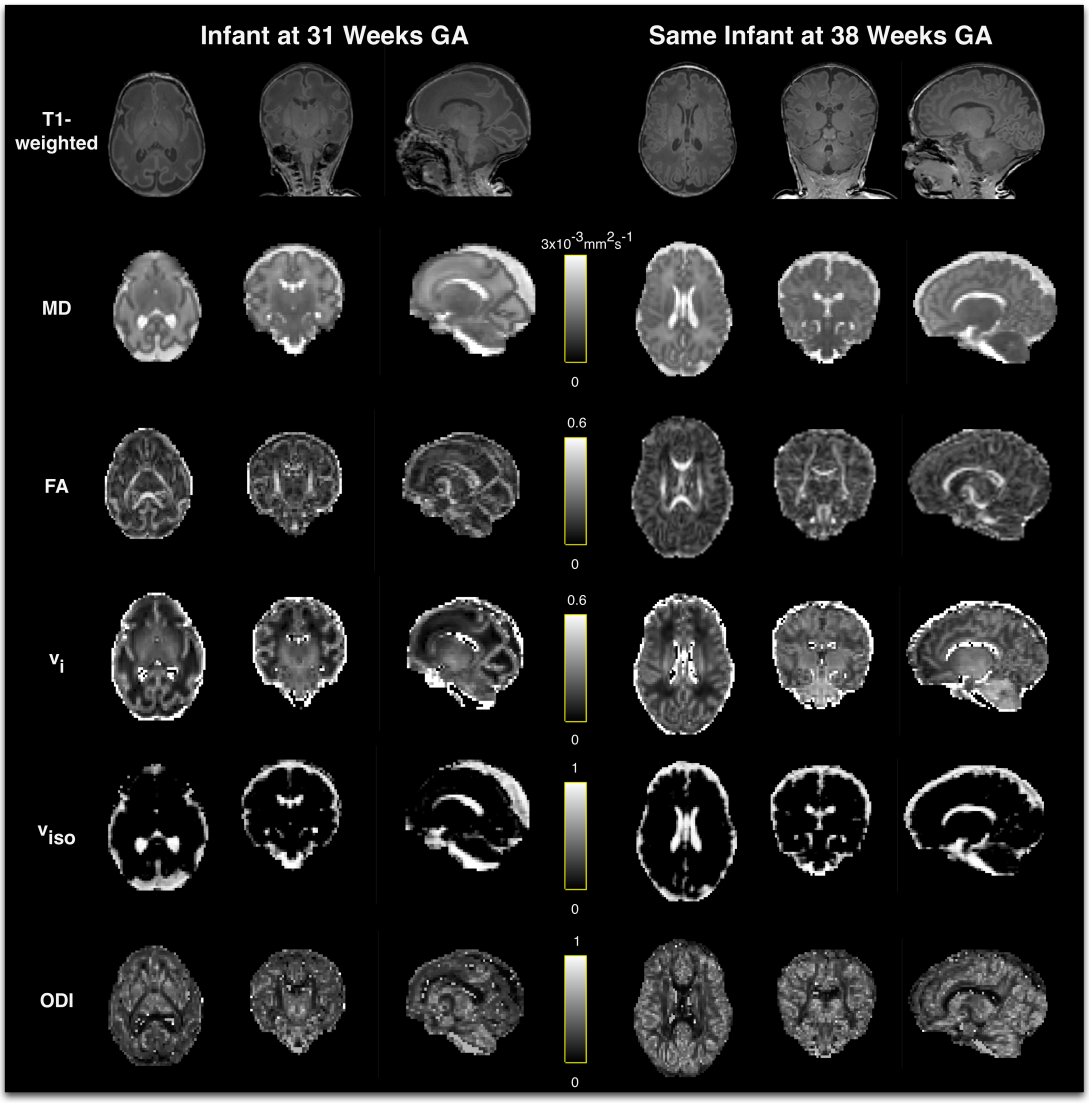

Figure 3.1: The parametric maps for an infant at pre (left) and term (right)-timepoints. In the white matter tracts, there is an increase in FA between timepoints. This is accompanied by a reduction in the ODI. The FA values in the cortex decrease noticeably between timepoints and the ODI increases. The v_i increases in general between timepoints

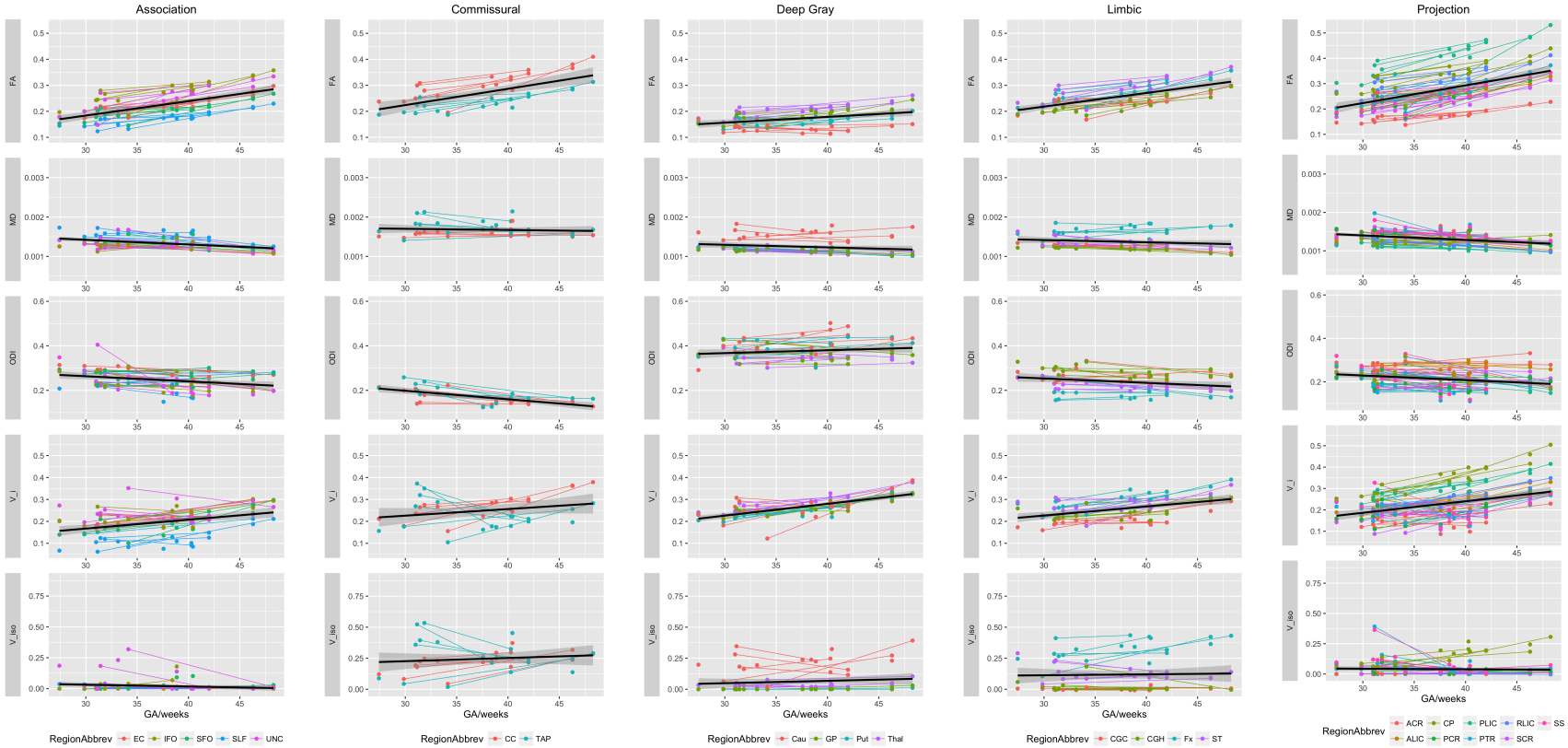

(a) (b) (c) (d) (e)

Figure 3.2: We plot the mean parameter value, across both hemispheres, for each region of interest. Coloured lines connect longitudinal measurements within a given region. Black lines are obtained by fitting a line to all the data (not with a mixed-effects model). We group the data by tract.

3.5.2 Trajectories of diffusion parameters.

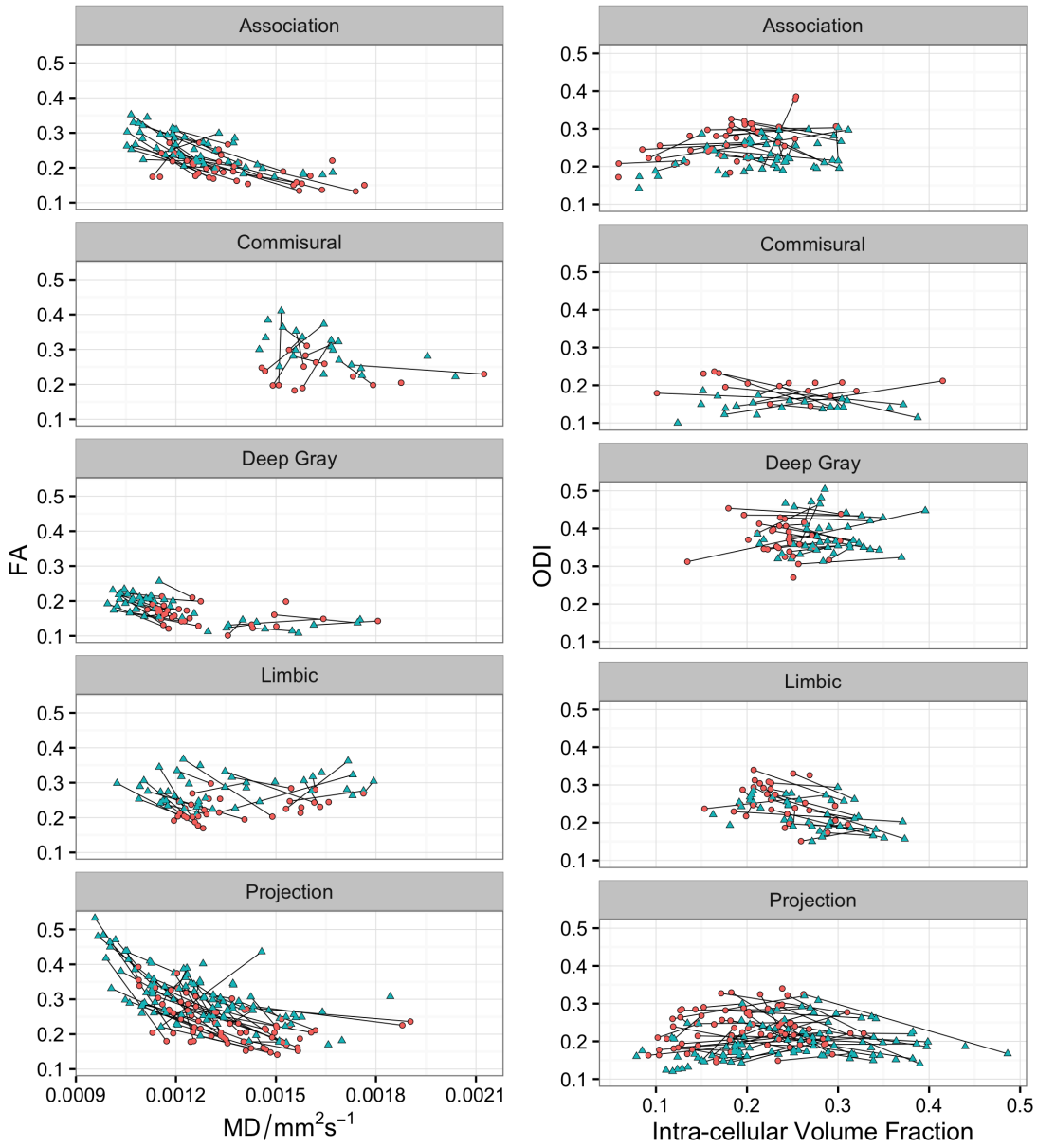

Figure 3.3: These plots display the relationship between parameters for DTI (left) and NODDI (right). Lines connect longitudinal measurements, at the preterm and term timepoints, within the same region. Blue triangles are the term datapoints, and the red circles are the preterm timepoint. There is one value per region in Table3.1, per subject.

In Figure 3.3, we plot the NODDI and DTI parameters against each other, for each of the tract systems from Table 3.1. There are differences between preterm and term timepoints. Within the association tracts, the MD decreases and the FA increases. Using the NODDI model, this manifests predominantly as a decrease in the ODI. In the commissural tracts, the FA increases, which is, again, represented as a decrease in ODI.

Within the limbic tracts, the FA increases, while the ODI decreases and the v_i increases. The projection tracts decrease in MD and increase in FA, which is represented by ODI increasing in the NODDI model. Finally, the deep grey matter decreases in MD and FA increases as the preterm period goes on. This change is represented predominantly as a change in v_i in NODDI, in contrast to the white matter regions.

3.5.3 Comparing DTI and NODDI effect sizes

To compare the sensitivity of DTI and NODDI parameters, we computed Cohen's d for each of the regions. We did this using paired samples (using only the longitudinal results) and display the absolute values of d in Table 3.2. We also averaged the values across the tracts.

Although the number of subjects is not especially large, some clear trends can be seen. Across the white matter tracts, FA has higher effect sizes than v_i ($p = 2.55 \times 10^{-3}$) and ODI ($p = 3.86 \times 10^{-6}$) as computed by two sample t-test. In the grey matter, DTI and NODDI parameters have statistically indistinguishable values for effect size.

3.5.4 Pairwise testing of regions

In Figure 3.4 we plot a diagram to show which statistical model best represents the data. We see that for the majority of region pairings, model 5 has the lowest AIC. This model has different slopes and values for the two regions being tested. The different diffusion parameters support different statistical models from each other in many of the cases. In particular, the FA selects model 5 most frequently, and MD often selects model 4 (the regions being tested having indistinguishable slopes).

3.6 Discussion

This study utilises the NODDI and DTI models in tandem to investigate white matter maturation in the preterm period. This study agrees with previous findings that FA increases and MD decreases in the white matter. In the NODDI model, the v_i increases in white and grey matter regions. The ODI decreases over the preterm period for the white matter, which may relate to the underlying reorganisation and retraction of axonal pathways during maturation [94]. It stays relatively constant for the deep grey matter. The decrease in MD throughout the brain does not have a straightforward correlate within the NODDI model. The decreasing diffusivity may affect intra- and extra-cellular space

		MD	FA	ODI	v_i
Region	Tract	|Cohen's d|	|Cohen's d|	|Cohen's d|	|Cohen's d|
EC	Association	1.26	1.48	0.85	1.15
IFO	Association	0.57	1.44	1.07	0.80
SFO	Association	1.20	1.02	0.21	1.17
SLF	Association	1.09	1.61	0.07	0.85
UNC	Association	0.79	2.00	1.16	0.06
CC	Commissural	0.32	1.42	1.19	1.19
TAP	Commissural	0.50	1.34	1.81	0.29
Cau	Deep Grey Matter	0.11	0.16	1.16	0.63
GP	Deep Grey Matter	1.11	1.38	0.69	1.06
Put	Deep Grey Matter	1.50	0.82	0.60	1.37
Thal	Deep Grey Matter	1.67	1.56	0.20	1.77
CGC	Limbic	0.70	0.94	0.22	0.71
CGH	Limbic	0.97	1.79	1.17	1.19
Fx	Limbic	0.75	1.67	0.50	1.83
ST	Limbic	1.15	1.45	0.90	0.83
ACR	Projection	0.77	1.29	0.00	0.77
ALIC	Projection	1.65	1.09	0.25	1.49
CP	Projection	0.21	1.50	0.70	2.16
PCR	Projection	1.53	1.57	0.43	0.71
PLIC	Projection	1.67	1.52	0.86	1.58
PTR	Projection	1.25	1.53	1.16	0.12
RLIC	Projection	1.68	1.31	0.59	1.62
SCR	Projection	1.82	1.58	0.26	0.96
SS	Projection	1.12	1.45	1.40	0.12
		Mean |Cohen's d| (standard error)			
		MD	FA	ODI	v_i
	Association	0.98 (.13)	1.51 (.16)	0.67 (.22)	0.81 (.20)
	Commissural	0.41 (.09)	1.38 (.04)	1.50 (.31)	0.74 (.45)
	Deep Grey Matter	1.10 (.35)	0.98 (.31)	0.66 (.20)	1.21 (.24)
	Limbic	0.89 (.10)	1.46 (.19)	0.70 (.21)	1.14 (.25)
	Projection	1.30 (.18)	1.43 (.05)	0.63 (.15)	1.06 (.23)

Table 3.2: In this table, we present Cohen's d for each region, and averages over each tract system. Effect sizes of over 0.80 are deemed 'large', 0.20-0.50 'medium' and 0-0.10 'small'.

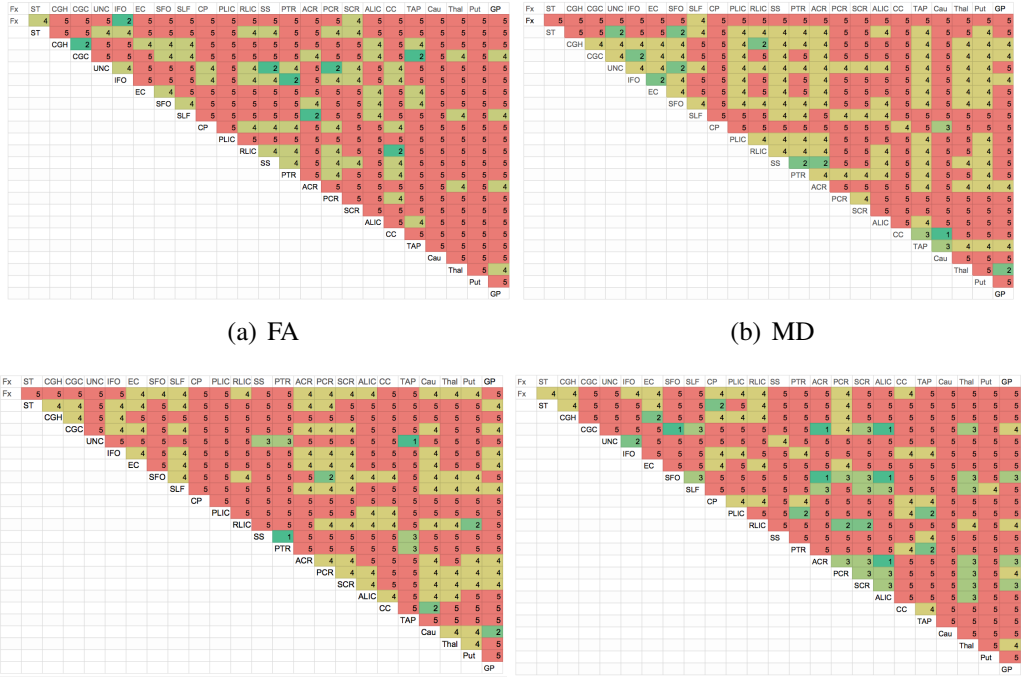

(a) FA (b) MD

(c) v_i (d) ODI

Figure 3.4: In this figure, we display which of the models from Section 3.4.3 applies for each of the parameters. Most regions can be separated by pairwise testing. Region abbreviations are the same as in Table 3.1. Regions have significantly different parameters for models 3, 4 and 5.

in the same fashion, which would not change v_i. In the PLIC, we observe high FA values, which is attributable to myelination and fibre alignment. In NODDI, this region has high v_i, which could reflect reduced extra-cellular space caused by the presence of myelin.

While NODDI may provide complementary information to DTI in the white matter, there is no evidence here that this information increases the sensitivity to maturational events.

We performed pairwise testing between regions in order to investigate whether NODDI could separate regions, as in [87]. Including a longitudinal component made it easier to separate regions, which allows greater insight into the spatio-temporal patterns of growth. These patterns are important markers of tract integrity and overall health. The objective of the pairwise testing is to determine whether the chosen diffusion model has properties that are useful in distinguishing tissue types. Tissues have different microstructure, which should be reflected in the measured parameters. In general, according to Figure 3.4, DTI and NODDI both separate parameters well. For

some comparisons, such as the corpus callosum and the thalamus, model 5 is optimal for every parameter. In 3.4(a), the FA separates the deep grey matter from white matter regions more easily than other parameters. It does not seem that NODDI is more able to separate two given regions than DTI. This is concordant with the effect sizes being greater, in general, for white matter regions with the DTI model than with NODDI. For these regions, there is no evidence here that NODDI is superior for measuring microstructural change.

One limitation of the presented work is that the chosen atlas is not longitudinal, having just one labelled image. A multi-atlas technique would account better for the natural variability of brain images, especially in our heterogeneous cohort. Additionally, the atlas is more similar to term brains than to preterm, meaning that the younger time points won't be as well-registered to the template. However, although the brain changes rapidly in the studied period, white matter structures are much more established than a feature like the cortical folds. In terms of visual inspection of the registration results, it appears that white matter tracts were well-registered at each timepoint. Developing a multi-subject atlas is outside of the scope of this work.

Another consideration is to what extent the fixed parameter of the intra-axonal diffusivity affects the measured parameters. Fixing the parameter is at odds with the fact that the axial diffusivity decreases during the preterm period, as the amount of water in the brain decreases. It would be plausible to fit and use a time-dependent diffusivity in the model-fit. The main issue with this approach would be in determining the necessary diffusivity on a subject-by-subject basis. This would be similar to using a spherical deconvolution technique, [78], but this requires nominating voxels to act as 'typical' white matter voxels. This would be problematic, because different regions are maturing at different rates. Although it would be possible to select the intra-axonal diffusivity by including it as a free parameter in the model, fitting this extra parameter may make the model-fitting intractable or less stable.

In addition to the model-fitting problems, maturation also affects the macrostructural geometry. It is not clear whether macrostructure affects microstructural parameter readings, but there is some evidence that this would occur, in part because of reducing partial volume due to growth. Future work could test this, discussed more in Section 10.2.3. In future, we also plan to investigate whether these diffusion parameters have

correlates with cognitive and motor outcomes throughout childhood. We will also investigate multi-modal modelling, as other MRI modalities may have complementary information to improve DW MRI.

3.7 Conclusions

In this chapter, we have demonstrated how tissue properties change in the preterm period, using the NODDI model. White matter tends to increase in v_i, while ODI decreases. It is not clear that NODDI parameters provide additional value in terms of explaining the microstructure to DTI parameters. However, the bio-physical nature of the NODDI parameters does, at least, complement the DTI representation. The grey matter regions, in particular, merit further examination: we cover them next.

Chapter 4

Using NODDI to measure cortical maturation in the preterm brain

4.1 Introduction

In this chapter, we use the NODDI model [165] to analyse the changes in the cerebral cortex and the thalamus, both grey matter regions, in 12 of the subjects from the Sparks dataset (Section 3.2). We showed region-dependent changes in NODDI parameters over the preterm period, highlighting underlying changes specific to the microstructure.

Longitudinal changes in the brain, as measured by MRI, may have important cognitive correlates. In the presented work, we calculate changes in diffusion parameters in the grey matter. We combine state-of-the-art signal modelling and image processing in order to derive how these microstructural parameters coincide with known developmental processes. These sensitive measures may aid in predicting patient outcomes in this at-risk population.

Here, we establish normative NODDI values for the preterm population in the cortex and thalamus, and quantify microstructural, longitudinal changes over the preterm period.

4.1.1 Contribution

Work in this chapter was originally presented at ISMRM 2014, as an oral presentation (Section B.3[10]). The work was then extended and published in NeuroImage (Section B.1[2]). It was the first time time that NODDI parameters were evaluated in both the cortical and thalamic grey matter as a function of age in preterm infants.

4.1.2 Hypothesis

DTI changes in the cortex are related to growth of dendrites and other microstructural changes [101]. This hinders diffusion, reflected by reductions in MD and in FA [14]. We predict that this change will manifest as an increased ODI over the preterm period, because the diffusion becomes more dispersed as the dendrites and axons are elaborated. We also predict v_i to rise because of increasing density. In terms of v_{iso}, we know that the water content in the brain is decreasing, and thus the diffusivity will also decrease. Therefore, as the diffusivity becomes farther from the value for free water, v_{iso} will decrease.

The nucleic substructures of the thalamus have formed by 24 weeks gestation [48]. Thus, we expect the fibres to retain similar geometry, and hence similar ODI between the timepoints. There is a decrease in radial diffusivity [11] which is related to the histological knowledge that the thalamus is myelinating during the preterm period [68]. In other studies using NODDI to explore white matter characteristics in newborns, it was shown that v_i is related to the myelination status in the posterior limb of the internal capsule [87]. Therefore, we would expect an increase in v_i in the thalamus over the preterm period. This increase was noted in [42]. We expect v_{iso} to be small at both timepoints.

4.2 Methods

4.2.1 Subjects

In this particular study, twelve infants were included, with mean estimated gestational age (EGA) of 25.9 $\pm$ 1.0 weeks at birth. Seven of these had the full data acquisition at pre- and full-term timepoints, so there were 19 sets of scans in total. All infants in this study were born at $<$ 28 weeks completed gestation and their characteristics are summarised in Table 1. Informed parental consent was obtained for all infants and the study was approved by the local research ethics committee.

Table 4.1: This table presents the subjects in the experiment. *'s, †'s denote twins. N/A refers to missed scans (d,k at preterm) or scans that haven't yet taken place (l at term). The column '%D' refers to the percentage of diffusion-weighted scans that were included after diffusion pre-processing.

Subject Identifier	EGA at Birth (Weeks, Days)	Birthweight (grams)	Sex	EGA at scan 1	Quality Control (QC)	%D	EGA at scan 2	QC	%D
a	26+1	784	M	33+1	yes	93	40+1	yes	93
b*	26+4	903	M	34+2	T_1 motion	N/A	48+2	yes	98
c*	26+4	922	M	34+2	T_1 motion	N/A	48+2	yes	89
d	25+2	776	M	N/A	N/A	N/A	37+4	yes	91
e†	25+1	730	M	31+3	yes	94	42+0	yes	98
f†	25+1	760	F	31+0	yes	83	42+0	yes	91
g**	27+1	1038	M	30+6	yes	94	46+2	yes	93
h**	27+1	880	F	29+6	yes	94	46+2	yes	80
i‡	26+2	940	M	31+6	yes	91	40+2	yes	100
j‡	26+2	1095	M	34+4	yes	46	40+2	yes	80
k	23+6	680	M	N/A	N/A	N/A	38+6	yes	67
l	25+4	956	M	27+3	yes	93	N/A	N/A	N/A

4.2.2 MR Acquisitions

The data acquisition is detailed in section 3.2.

4.2.3 Neurite Orientation Dispersion and Density Imaging (NODDI)

The NODDI model is introduced in Section 2.3.4. We fit the data as detailed in Section 3.4.2. In this chapter, the values labelled 'v_i' are actually (1-v_{iso})v_i. This is so that the parameter value refers to the proportion of the voxel being taken up by intra-neurite space. It is worth noting that v_{iso} values are near zero in most WM and GM tissue, so the two measurements will be similar.

4.2.4 Diffusion Preprocessing

An underlying assumption of fitting a diffusion model is that a voxel's signal comes from the same place in the anatomy. For bulk motion during the protocol, common in the neonatal population, there will be displacement in the images which can be corrected by registration. If a subject moves during an acquisition, there is significant signal dropout. We manually identify affected volumes by their signal dropout and remove them. Imaging artefacts can also cause errors in alignment which also require correction.

To align the images we adopt an image registration strategy inspired by [10]. Affine registration to reference volumes ameliorates eddy-currents as well as correcting for bulk motion. While some techniques register to the reference (b= 0) values, this means that the contrast in reference and floating images are drastically different. To register to a target with a similar contrast, we generate 'synthetic' reference images. Our pre-processing algorithm is presented in (Figure 4.1) and achieves this in two steps. After bad volumes are removed (1), each volume is registered to the groupwise average of all of the b=0 images (2). We then fit the diffusion tensor model and use the model to produce synthetic images, for each b-value and gradient direction. Each raw image is then registered affinely to its synthetic partner (3). Because these were constructed after registration to the b=0 images, registering these can simultaneously correct for distortion and motion between acquisitions. From the transformations, we rotated the b-vectors and modulated by the Jacobian determinant [77], assuming that

the largest part of the rotation in the affine transformation was due to bulk motion [93]. All registrations are carried out using NiftyReg [120] [119].

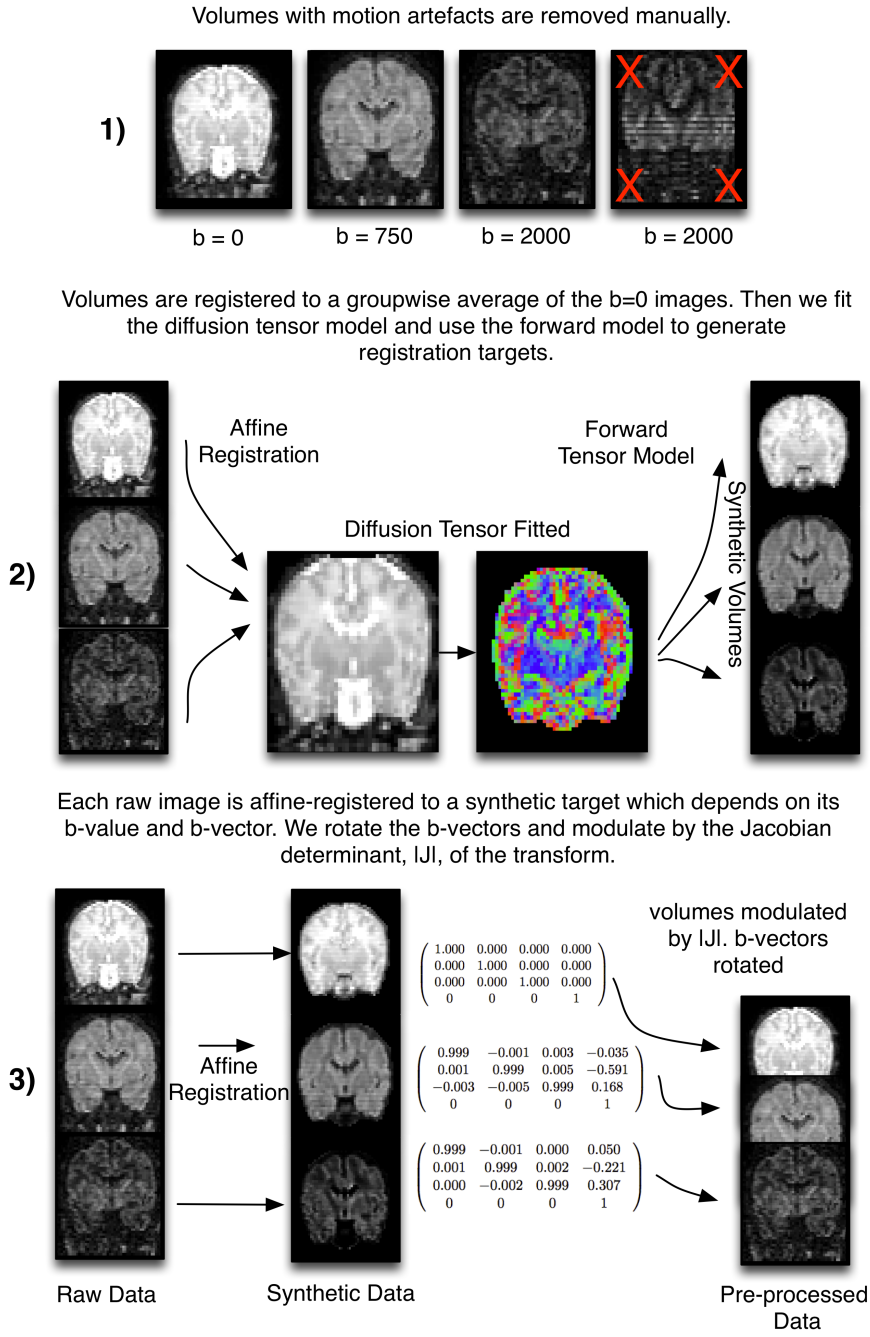

Figure 4.1: The pre-processing pipeline. High b-value images have markedly different contrast from the $b = 0$ images. Thus, to ensure each image has a suitable registration target, we generate these using the diffusion-tensor model. We use the forward model to generate the registration targets.

4.2.5 Segmentation

In order to analyse the NODDI parameter maps, we require anatomical labels in the diffusion space. Image segmentation is difficult in neonates for reasons including poor image contrast, lower SNR, the increased prevalence of motion artefacts and patient heterogeneity. The smaller size of the brain, compared to adults, also means partial volume effects are more common. Here we outline our segmentation approach. To segment the diffusion images, we ruled out segmenting the images in the native diffusion space because the resolution and contrast are inadequate.

To segment the T_1-weighted structural images, we used the AdaPT algorithm [33] which is optimised for a preterm subject group. It uses a probabilistic Gaussian mixture model, initialised with a 6-class 4-D probabilistic atlas specific to the neonatal population [84]. We manually corrected brain masks in order to initialise the segmentation. The tissue classes are: white matter (WM); cortical grey matter; cerebellum; deep grey matter; cerebrospinal fluid (CSF) and brainstem. In order to segment the thalamus, we used segmentation propagation [35] to fit a population-specific neonatal atlas [64] to the T_1-weighted data, generating a 50-label map for each subject from which we took the thalamus. The segmentations for the longitudinal infants at preterm and term timepoints are shown in Figure 4.2.

We registered the T_1 to diffusion space rigidly and propagated the segmentation. However, because diffusion images have magnetic susceptibility artefacts, the true transformation is non-linear in nature. Susceptibility distortions occur in regions of high differential in magnetic susceptibility, such as the occipital and frontal cortex [65]. It is important to note that on deforming the diffusion space to its correct anatomical dimensions, the diffusion information from each voxel cannot be retrieved. The susceptibility artefact means that many voxels' signal is compressed into fewer, leading to characteristic bright regions. This signal effectively averages across several voxels, which will span multiple tissue classes. Therefore it is important to disregard these areas in the analysis.

To identify regions of susceptibility distortion for exclusion, we compare the tissue segmentation in diffusion space to the MD map. The MD has good contrast for the CSF/cortex boundary and so we identify slices where the segmentation fits poorly by examining the segmentation overlaid on the MD image. We manually edit the masks

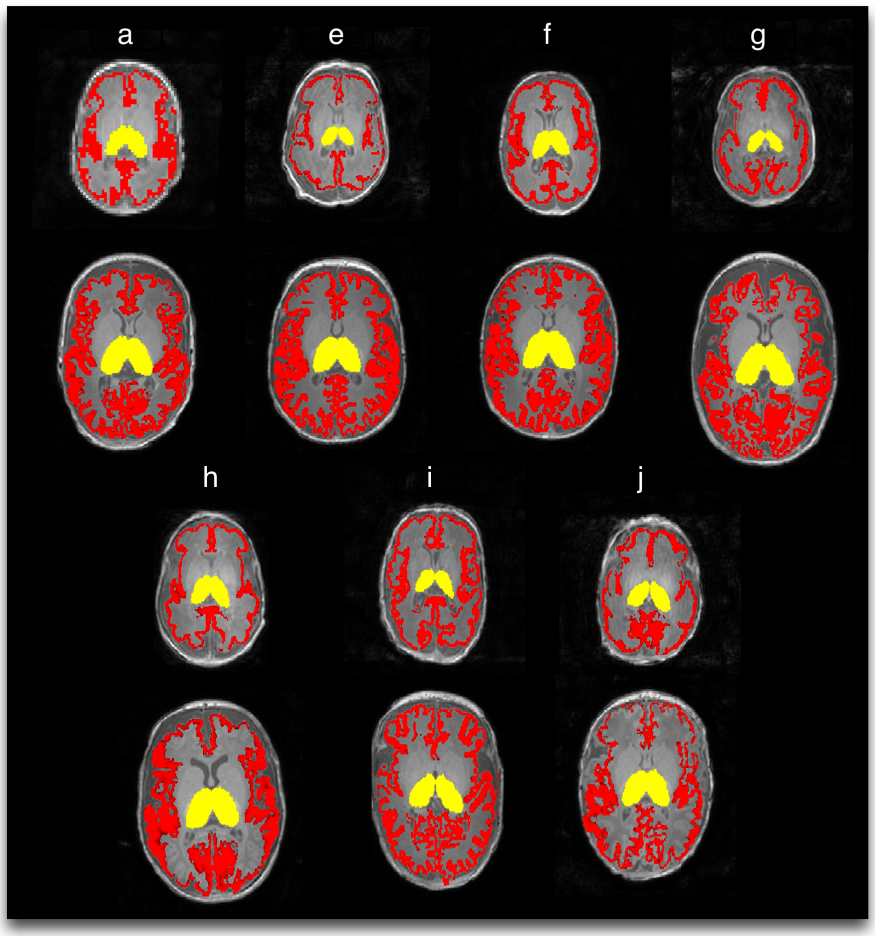

Figure 4.2: The segmentations at preterm (top) and term (bottom) timepoints of the thalamus (yellow) and the cortex (red).

to exclude the regions of the cortex where there the segmentation is incorrect, which has been caused by susceptibility distortion. Doing this, the major deformations are especially prevalent in the occipital and frontal cortices as expected [65].We show an example where the excluded regions are highlighted (Figure 4.3). We also exclude voxels from the analysis where v_{iso} exceeds 50% because this implies the tissue label for this voxel is wrong.

4.2.6 Cortex and Partial Volume

For the infants in our study, the cortical layer is 1-2 mm thick. Thus, due to the voxel size, there will be significant partial volume effects in the cortical region. It is unlikely that the observed parameters will reflect only the changes in the cortex. However, the v_{iso} component, in principle, will remove the effects of isotropic diffusion, for example at the cortex-CSF boundary. In the WM-GM regions, the fit will model diffusion data

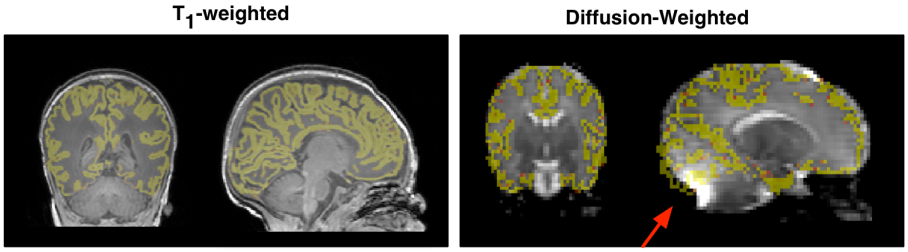

Figure 4.3: The segmentations still fit well in most cortical regions after being registered to diffusion space. However, in regions with susceptibility distortion (arrow) there is a shift in cortical boundary. Diffusion signal in this region comes from a greater range of locations in physical space. We manually exclude the regions that fall outside of the brain in the diffusion image.

coming from both tissue types.

4.3 Results

4.3.1 Parameter Maps

We fitted the NODDI and DTI models for each infant brain (Figures 4.4, 4.5). The FA maps show the expected pattern of contrasts, with high values in the cortex at the preterm timepoint. This high-anisotropy rim is no longer apparent by term-equivalent age. The MD is high in regions of CSF. In terms of NODDI parameters, the v_{iso} component is high in regions of cerebrospinal fluid - outside of the brain and in the ventricles. Well defined and highly-directional white matter areas, such as the corpus callosum (CC), tend to have the highest v_i values, in both 30- and 40- week scans. The v_i values in the cortex are lower than in the CC but appear as high-value regions compared to the adjoining white matter. There is a general increase in contrast over the preterm period. ODI is low in the corpus callosum and white matter projection tracts. At the term timepoint, the cortex has greater contrast from surrounding matter than at the preterm point. By excluding voxels in which $v_{iso} > 0.5$, the cortex had 8%(pre) and 4%(term) of voxels removed while the thalamus had 3%(pre) and 2%(term).

4.3.2 Cortical Results

We combined the data from all longitudinal subjects for analysis. The histograms of the parameters at term and preterm timepoints are shown in Figure 4.7. We reproduce the result that the FA and MD both decrease over the preterm period [14]. With the NODDI model, these changes manifest predominantly as changes in the ODI. Fitting a normal

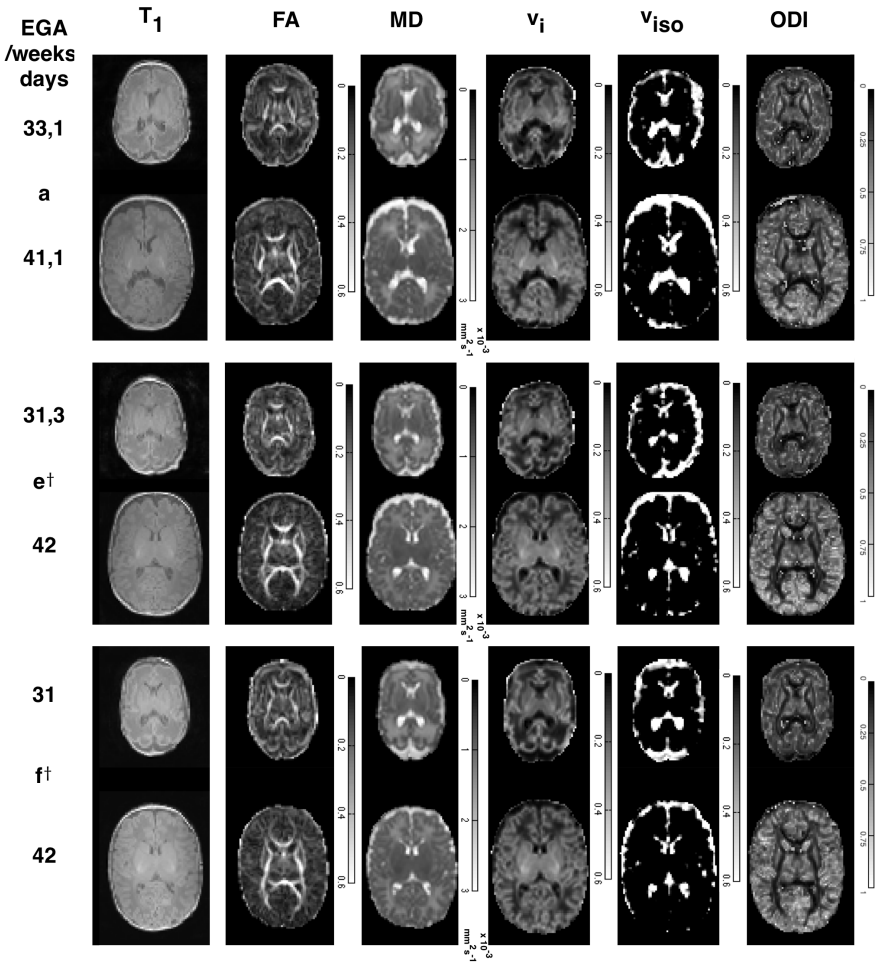

Figure 4.4: Parameter maps for infants at preterm and term timepoints.

distribution to these histograms, the mean of the ODI increases from 0.298 $\pm$ 0.001 to 0.436 $\pm$ 0.001 (note that these errors are the confidence interval for the mean after fitting a Gaussian, not the standard deviation of the distribution). The v_i has a small change, from 0.231 $\pm$ 0.001 to 0.239 $\pm$ 0.001. We also plotted results individually for each infant summarised in these graphs, in Figures 4.6 and 4.8.

4.3.3 Thalamus Results

Figure 4.7 displays the histograms for the thalamus. In the thalamus, the MD decreases and the FA increases during the preterm period, as in [11]. There is an increase in v_i from 0.241 $\pm$ 0.001 to 0.312 $\pm$ 0.001. The ODI remains constant — from 0.344 $\pm$ 0.003 to 0.342 $\pm$ 0.002. We also plotted results individually for the thalamic GM in

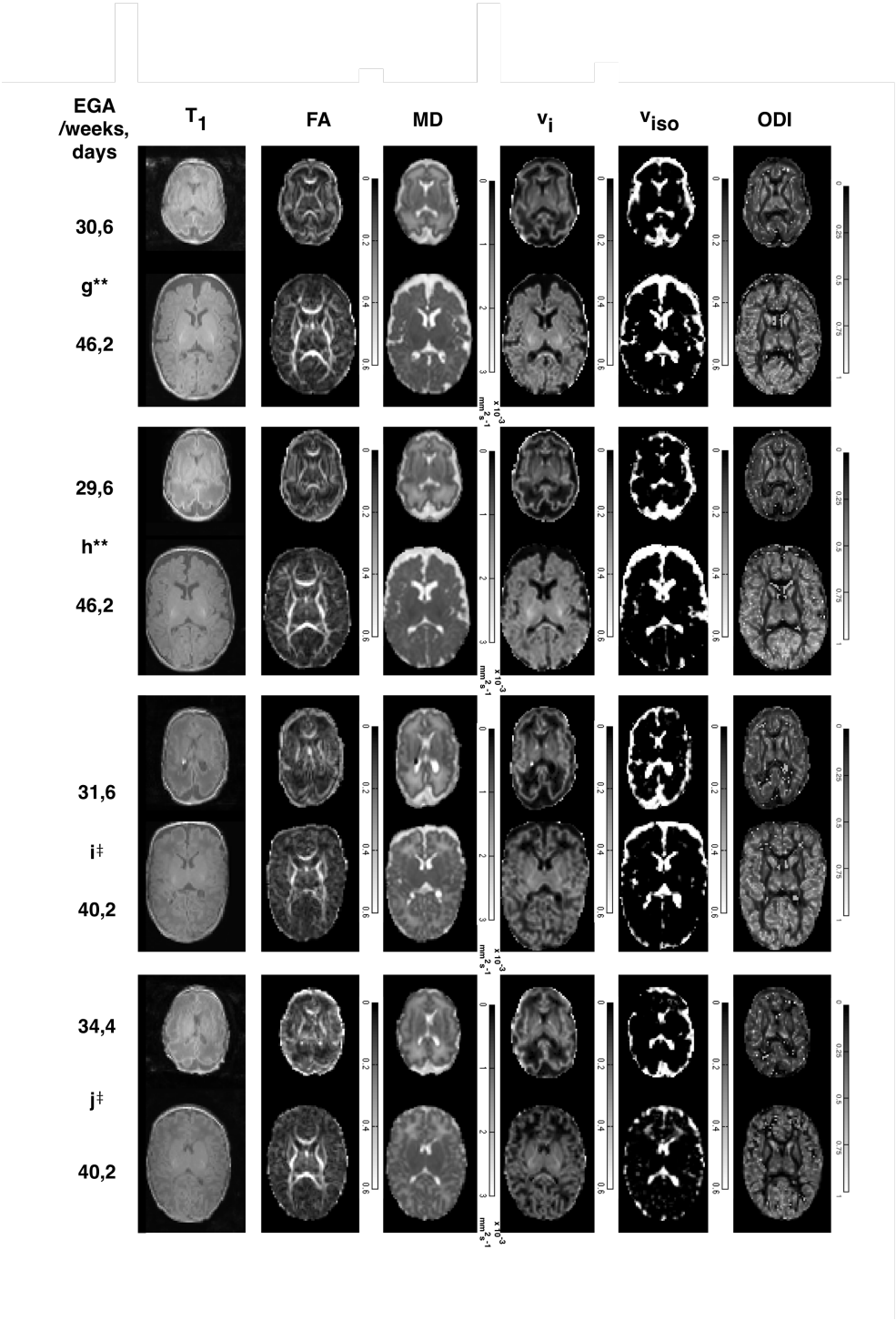

Figure 4.5: Parameter maps for infants at preterm and term timepoints.

Figure 4.8.

4.3.4 Cross-sectional Analysis

To include the data from infants with only one timepoint with the longitudinal subjects, we plotted the means of the parameters as a function of gestational age (Figure 4.9).

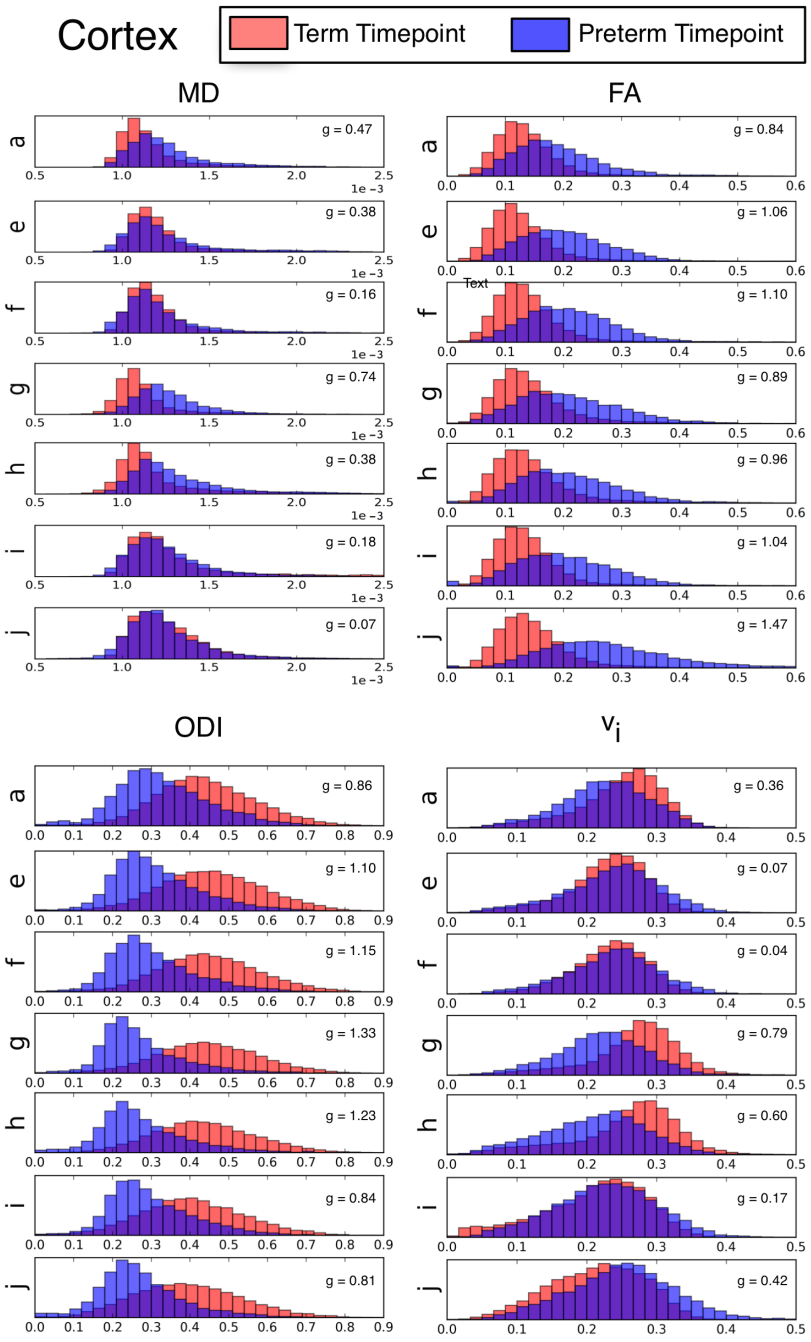

Figure 4.6: Histograms for the longitudinal subjects of parameter values at the two time-points for the cortical grey matter. The y-axis represent the number of voxels. The x-axis is the parameter value. The means of the data are included in Figure 4.9. The absolute value of Hedge's g (a measure of effect size) is in the legend. All subjects show significant changes in each parameter with $p < 0.001$, although some effects are small.

The confidence intervals on the mean were calculated by assuming a normal distribution on the parameters, which is supported by visual inspection (Figure 4.7).

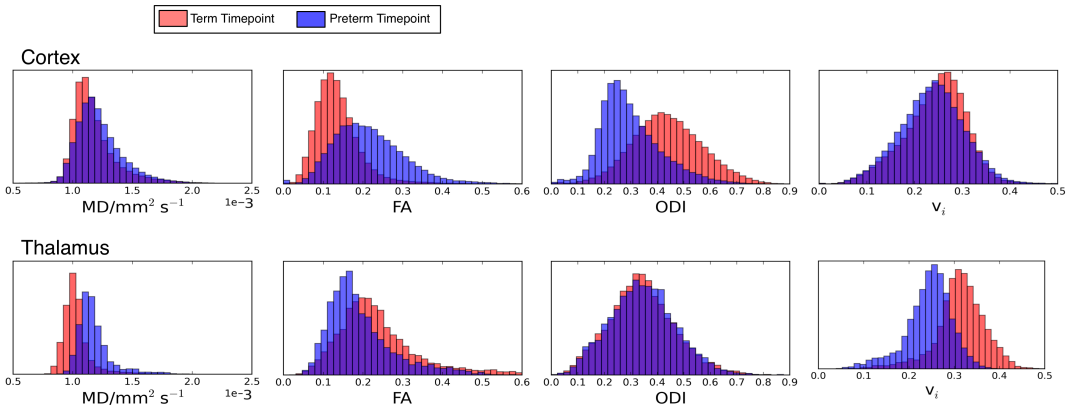

Figure 4.7: Histograms of parameter values at the two time-points for the cortical grey matter. The y-axis represent the number of voxels (normalised so that the area of preterm and term infants are equal). The trends and values for the parameters depend on the region. Here, we have pooled all the subjects' data.

In Figure 4.9 we can see that the trends represented by the histograms seem to hold for the subject pool as a whole. To analyse the trends, we performed a linear regression on each dataset and calculated the 95% confidence interval on the slope, to see whether the slope confidence interval included 0, which we will denote as 'not changing'. In the thalamus, the MD decreases, the FA and v_i increase and the ODI and v_{iso} do not change. In the cortex, the MD, FA and v_{iso} decrease while the ODI increases. The v_i does not change.

4.4 Discussion

4.4.1 The Cortex

We observed the changes we predicted in Section 4.1.2 in v_{iso} and ODI but not in v_i. Of the 7 longitudinal subjects, all demonstrated the trends in v_{iso} and ODI. These changes correspond to a reduction in FA over the same timescale. Thus changes in the FA correspond more closely with orientation dispersion than with v_i. Although there is an increasing cellular density during this period it does not appear to show in the v_i measurement. There may be other microstructural elements confounding the measurement, or the v_i may not be particularly sensitive to this change.

Although there was not significant evidence of an increase in v_i, looking at Figure 4.9, infants b, c, g and h have the largest gestational ages at the term scans and higher v_i values. This suggests a non-linear change in the parameter, with a decrease preceding

an increase. However, more subjects would be needed to support this assertion.

4.4.2 Thalamic GM

We predicted and observed an increase in the v_i for each pair of scans, indicating sensitivity to myelination status. While the ODI does not show evidence of change, the increase in v_i supports the hypothesis that the NODDI model is sensitive to the geometry of the surroundings. In this case, we interpret the increase in v_i as being caused, at least partially, by the myelin filling the extra-cellular space.

4.4.3 Cross-Sectional Data

Combining the measurements from all subjects allows some of the trends to be shown more clearly (Figure 4.9). In the thalamus, the trends are linear, as in [11]. We interpret the combination of NODDI and DTI parameters to show that the thalamus is myelinating during this time-period, with the differences being seen most clearly in the v_i values. The values in the cortex show some evidence of non-linearity, as in [14], where the piecewise linear fit has a break at approximately 38 weeks for the FA measurements. From weeks 35-50 in our data, there is an increase in v_i. This may be related to the cellular density. This cross-sectional aspect is an area of future interest as we acquire more infants and controls.

4.4.4 Utility of the NODDI Model in the Preterm Population

When interpreting DTI measures, similar combinations of FA and MD can be interpreted in differing ways depending on the anatomy. For example, high FA can represent a diverse array of microstructural conditions. The NODDI parameters, being compartments with biophysical inspiration, are more specific in their relation to the underlying microstructure.

In both the cortex and the thalamus, there are concurrent changes in the FA and in the MD. Both regions have a decreasing MD, which is a general feature of early brain maturation. The FA changes occur in the opposite direction for the cortex versus the thalamus. In the cortex, the ODI increases while the v_i's change does not significantly differ from 0. This suggests the major changes occurring are to do with geometry and a more complex microstructure. In the thalamus, the changes are reflected as an increase in v_i — which, in this case, could reflect a decrease in extra-cellular space due to the

development of myelin. The parameter changes depend on the local tissue type as well as general maturational trends.

In terms of the practicalities of scanning infants, acquiring multiple shells of diffusion data in a suitable timeframe remains a technical challenge. The scans we have presented in this work demonstrate a good compromise between image quality and scan duration. From Table 1 we can see that of the 12 subjects that we present data from, 7 of these had good data from both time-points. There were a further two infants rejected because of brain abnormality. The cortical segmentation worked well in the T_1-weighted data. Although this requires more of the scans to go well, there is no practical way of segmenting in the diffusion images. There remain issues with the segmentation being moved to diffusion space, especially in dealing with susceptibility artifacts.

4.4.5 Limitations

In this study, we have presented data from 4 sets of twins. Twinning is a major cause of preterm birth and we did not analyse the twins as a separate sub-group. Data from twin pairs shows less variation than from unrelated individuals, which may reduce the generalisability of the results.

Although v_i seems to correlate with myelination status, much as with the DTI model, the parameters may not be specific to myelin alone. For example, the v_i may be affected by the packing of the fibres that may change independently of myelination. The water trapped in myelin cannot be directly imaged by DW MRI and thus we are relying on the geometry of the diffusion to infer myelin indirectly. Thus, when interpreting results, it is still necessary to know the underlying biological processes.

In the NODDI model, we fixed the axial diffusion parameter at 2.00 x 10^{-3}mm^{2}s^{-1} as in [87], in contrast to the adult value of 1.70 x 10^{-3}mm^{2}s^{-1} from the original paper [165]. We believe that this value is representative for the cohort. In terms of its physical meaning, it represents the diffusivity along neurite tissue, which is different between adults and neonates — but also between preterm and term subjects. Preterm infants have higher diffusivities, so the choice of a constant value for both timepoints is a compromise. While in theory, the value could vary for each subject, this would add another parameter to the NODDI model and may reduce comparability

between subjects. It would be an interesting avenue of future work to investigate the effects of varying the axial diffusivity on the volume fractions and ODI, albeit out of the scope of the current work.

4.4.6 Future Work

Different areas of the cortex have different functional roles. Therefore, abnormalities of development in a given cortical region may manifest as associated functional defects at a later date. In addition to microstructural changes, the morphology of the cortex may also be different. In future, we will combine morphology measurements with the diffusion data, as in [108], in order to build a complete picture of perinatal growth. We will also investigate imaging correlates of the results of psychological testing in infancy.

4.5 Conclusions

In this study we have calculated NODDI parameters in the developing brain. We produced whole-brain maps of the parameters and analysed them on a region-of-interest basis. Using a multi-compartment diffusion model extends the work that has been performed using the DTI model. The thalamus and cortex show different trends in development, which relate to underlying differences in microstructural development. NODDI allows a more biologically-motivated interpretation of the diffusion data, which is important for defining robust developmental biomarkers in this cohort.

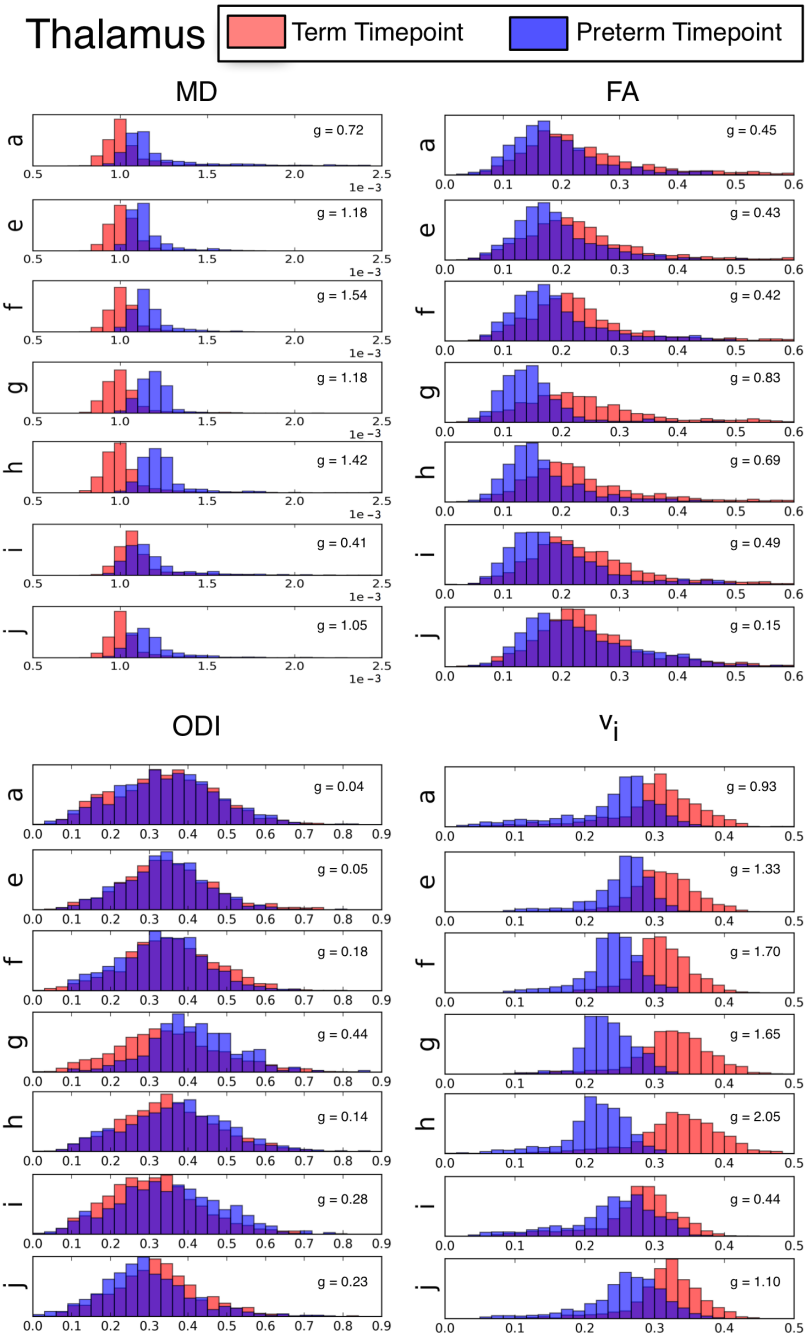

Figure 4.8: Histograms for the longitudinal subjects of parameter values at the two time-points for the thalamus. The y-axis represent the number of voxels. The x-axis is the parameter value. The means of the data are included in Figure 4.9. The absolute value of Hedge's g is in the legend. All changes in parameters from preterm-term timepoints are significant at $p < 0.001$ except in the ODI: $p = 0.38, 0.34, 0.0023$ for subjects a, e and h respectively.

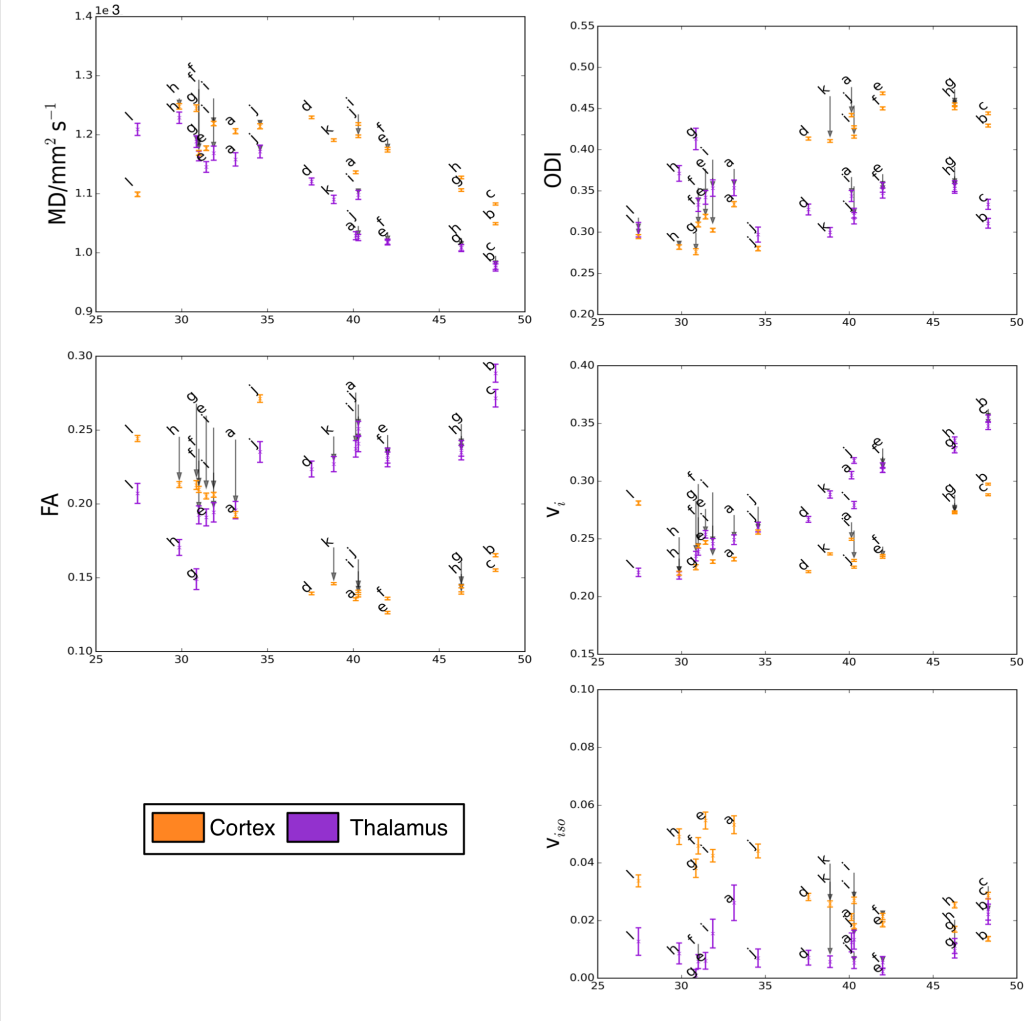

Figure 4.9: For each infant, we plot the confidence interval on the mean against gestational age for cortical and thalamic voxels. Datapoints are labelled with the letter of the infant (Table 1). The parameter changes over time agree with the trends in Figure 4.7. The authors recommend viewing this diagram electronically for clarity.

Chapter 5

Longitudinal measurement of the developing thalamus

5.1 Summary

As a neuronal relay centre, the thalamus is critical for effective cognitive function. Therefore, development of white matter connections between the thalamus and cortex is vital. By non-invasively examining the state of the thalamus we can monitor development in the preterm period. To track the development we develop a novel registration technique to combine data from multiple modalities, in order to derive the transformation from a preterm scan, to a scan of the same infant at term-equivalent age. By measuring the changes in diffusion parameters over this period on a per-voxel basis, we hope to provide unique insight into neurodevelopment.

In order to study longitudinal development, we require a good mapping for the thalamus at different timepoints. Common registration methods experience difficulties including a lack of T_1 contrast for the internal structures of the thalamus and the morphological changes in the thalamus. In this work we exploit complementary information from multiple MR modalities to improve biological plausibility. We use the structural computational connectivity to the cortex, as defined by probabilistic tractography, to generate sub-thalamic labels which should correspond to each other over the preterm period. Using this technique, our multi-modal registration retains the spatial arrangements of the different thalamic labels between the two timepoints. We use this registration to infer changes in microstructural parameters derived by fitting the Neurite Orientation and Dispersion Index (NODDI) model [165] to the data.

5.1.1 Contribution

In this work we present a multi-modal registration technique that allows us to map, for the first time *in-vivo*, the rates of change of microstructural characteristics in the preterm period. Because of the critical importance of the thalamus to cognitive and developmental health, these maps may aid in identifying healthy and abnormal development in this at-risk population. This work was presented at MICCAI 2014 (Section B.2[6]).

5.2 Methods

5.2.1 Data

The data acquisition is detailed in 3.2.

5.2.2 Image Segmentation

To investigate thalamic connections to the cortex, we segmented the thalamus and produced labelled cortical regions. Neonatal image segmentation is difficult relative to the adult population because of poor image contrast, lower SNR and the increased prevalence of motion artifacts. We use segmentation propagation [35] to fit a population-specific neonatal atlas [64] to the T_1-weighted data, generating a 50-label map for each subject. We then extracted the thalamus, and anatomical labels of the cortical regions. To segment the cortex itself, we used a probabilistic Gaussian mixture model approach initialised with a 6-class 4-D probabilistic atlas specific to the neonatal population [84], on intensity maps of the T_1 images. We corrected unsatisfactory segmentations manually. By combining the regional labels with the grey matter segmentation, we parcelated the cortex into frontal, temporal, occipital and parietal grey matter regions. These integer labels were propagated to diffusion space by affine registration of the T_1-weighted image to the diffusion space.

5.2.3 Multi-Compartment Diffusion Data

To account for the high instance of motion and other imaging artifacts, it is necessary to remove some acquired diffusion volumes. To identify these, we took the spatial derivative of the sum of the signal across each slice in the direction perpendicular to the imaging plane. We removed volumes where the derivate value was an outlier and afterwards, checked manually and removed any further volumes that had significant

artifacts. To bias-field correct the images, we registered each b>0 volume to the mean of the 6 $b = 0$ images using affine registration.

To improve the alignment of the diffusion weighted images, we fit a diffusion tensor to these data and generated synthetic registration targets with the diffusion tensor model. Thus, each volume has a registration target depending on the b-vector of the acquisition and the *b*-value, reducing the influence of diffusion-induced contrast change on the registration. The data is registered using an affine transformation to these targets and the diffusion tensor model is fitted again. The b-vectors are rotated and the signal is scaled according to the Jacobian determinant of the transformation.

NODDI is a technique for modelling the signal from a twin-*b*-value diffusion acquisition to yield greater microstructural sensitivity than DTI measures, such as fractional anisotropy (FA) and mean diffusivity (MD) [165]. For more details, see Sections 2.3.4 and 3.4.2.

5.2.4 Longitudinal Infant Registration

In order to exploit the longitudinal data, registration must define a reliable, anatomically plausible longitudinal mapping of the preterm thalamus to the term thalamus for each subject. To guide this registration we segment the thalamus into regions using probabilistic tractography from thalamic voxels to target cortical masks [24]. This results in a sub-thalamic labelling depending on projections to the cortex. We constrain registration to map regions with similar projections onto one another.

From the probabilistic tractography, we obtain a percentage in each voxel relating to each of the 8 cortical labels. We use this number to represent the proportion of the voxel connecting to each lobe. This approach is similar to [30], which used tractography to define a probability distribution across thalamic voxels, which represented their relative chances of reaching a given cortical lobe. We use this information to drive the registration, so that similar patterns of connection are maintained at preterm and term age. The method we use for non-linear registration is based on a cubic b-spline parametrisation of the transformation [131]. The spline parametrisation is, in our framework, used to define a continuous stationary velocity field over the space of the input images. Through a scaling-and-squaring approach, the field is exponentiated to yield a deformation field. Forward and backward transformations are optimised con-

currently to ensure symmetry. The obtained forward and backward transformations are the inverse of each other because we use a stationary velocity field. Within the current experiment, the spacing between the cubic b-spline control points is set to 2.5 voxels width and the bending energy of the velocity field is used to regularise the transformation. The segmentation of the thalamic sub-areas is used to drive the registration within a multi-channel approach, where each channel corresponds to the fuzzy membership of projecting to a certain cortical endpoint. Because these are treated as probabilities, we use the symmetric Kullback-Leibler divergence (KLD) as a similarity measure and we weight the contribution from each of the 8 channels equally. The KLD is suitable for matching probability distributions. The registration thus aims to finding the single transformation that maps best each fuzzy membership from the scans acquired at 30 weeks, to its equivalent in the scans acquired at term equivalent age. The pipeline of the techniques used in this paper is summarised in Fig 5.1. The probability maps show the correspondence between the sub-thalamic regions at 30 and 40 weeks, which we aim to map onto each other in the registration.

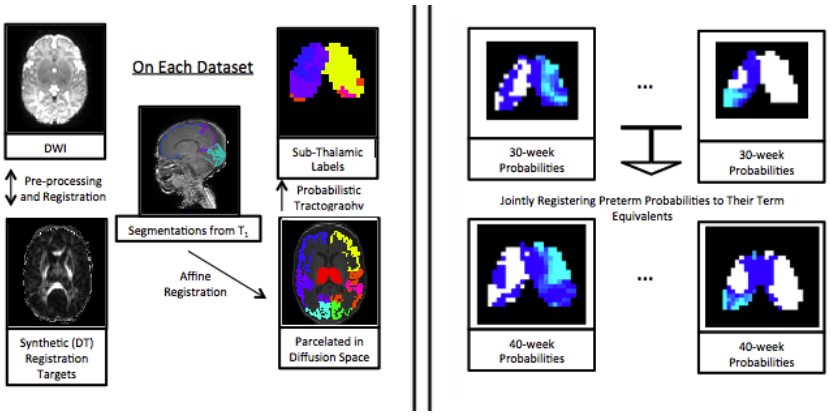

Figure 5.1: The sequence of processing steps. For each timepoint, the steps on the left-hand side are performed independently. On the right there are some of probability maps (blue-light blue) overlaid on the mask of the thalamus (white). For each timepoint, there are 8 probability maps for connection to distinct cortical regions. A single transformation is calculated to jointly map the probabilities to each other.

5.3 Results

5.3.1 Thalamic and Cortical Segmentations

The cortical segmentations for a representative infant are shown for the preterm timepoint (Fig 5.2a) and at term equivalent age (Fig 5.2b). The broad patterns of the thala-

mus remain visually consistent and maintain the distinct homotopy previously seen in adults and primates. We verified the cortical and thalamic segmentations visually.

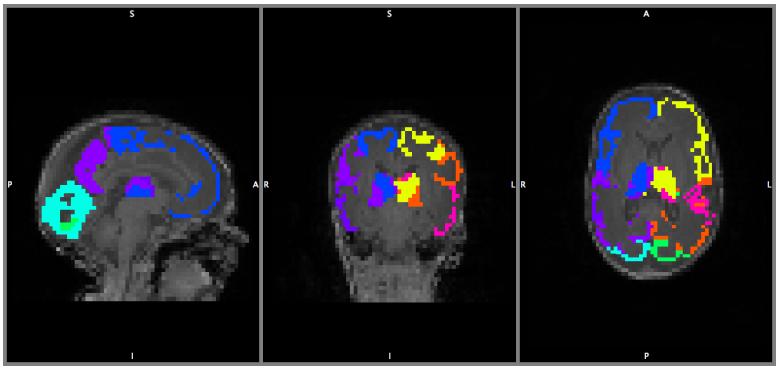

(a)

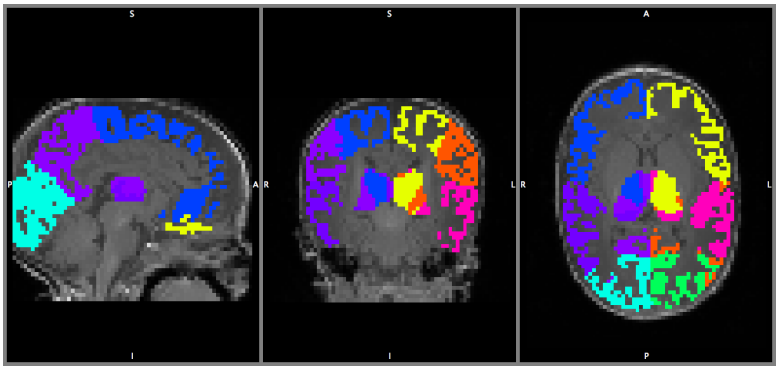

(b)

Figure 5.2: For (a) and (b), the Thalamus (centre), labelled by colour according to which cortical region it is most likely to project to. (a) is at 31.4 weeks, (b) is at 42.0 EGA. Note the similarities in the thalamic labels between the two timepoints.

5.3.2 Cortical and Thalamic volume change

The average volumes of the cortical regions, and the thalamic subregions that principally project to them (Fig 5.3), show the growth of the cortical regions in every subject, with the thalamus also expanding in volume. The thalamic regions display different growth rates, with the region projecting to the frontal cortex increasing in volume most; the frontal cortex has the greatest volume increase. The projections to the occipital cortex occupy a small proportion of the thalamus, because the volumes are taken after finding only the most likely projection in each region. Due to the small physical space occupied by the infant thalamus, we interpret this as a partial-volume effect.

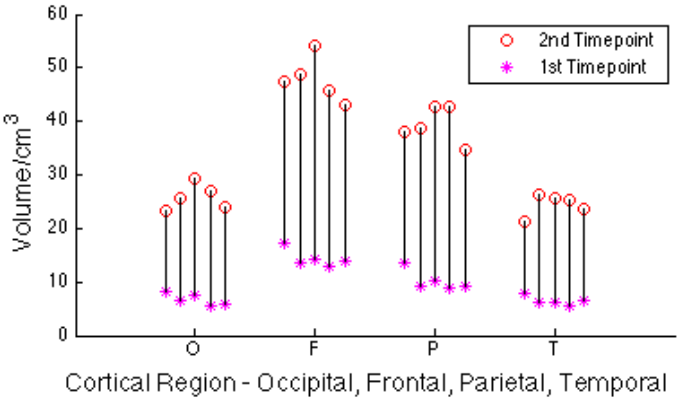

(a)

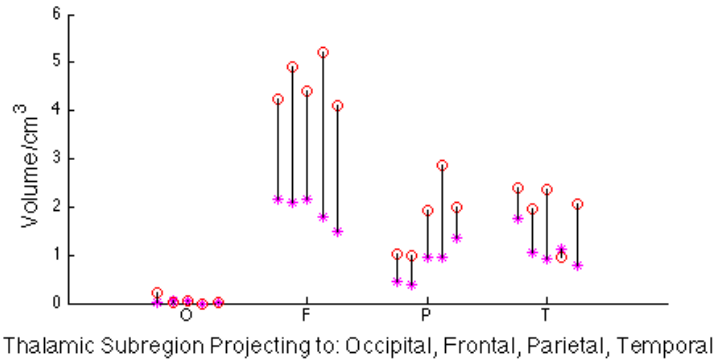

(b)

Figure 5.3: For each infant we plot the cortical volumes for each region (a) and the thalamic subvolumes that project to the cortical regions (b).

5.3.3 Longitudinal change in NODDI parameter maps

We have explained the necessity of a thalamic registration including information from the diffusion-weighted scans. Using these transformations, we can now show parameter change maps from the registered data (Fig 5.4).

These maps are generated from subtracting the registered preterm parameters from the term parameters. In terms of DTI parameters, the mean diffusivity shows little regional pattern. The FA decreases in the posterior portions of the thalamus, which project mainly to the temporal cortex. In terms of the NODDI parameters, the ODI seems to be closely related to the FA - there is high dispersion where there is low FA. More interestingly, all infants show significant increases in v_i, which suggests an increase in cellular density. Thus, as the volume of the region increases, the cellular density increases significantly. Infant (d) has a higher magnitude of change for v_i, which is likely to be because the infant had the longest time between scans (4 weeks greater

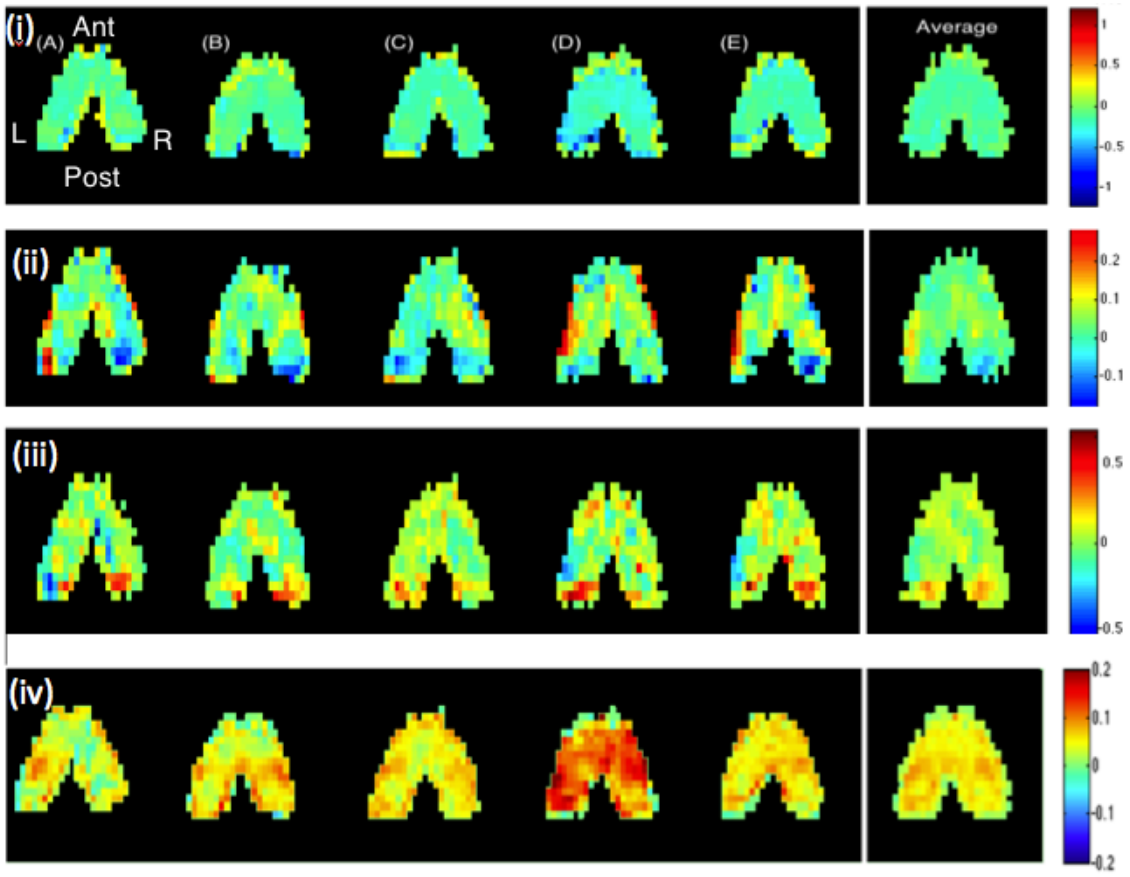

Figure 5.4: The maps of parameter change in the thalamus for each infant. (i) is MD in $10^{-3}mm^2s^{-1}$, (ii) is FA, (iii) is ODI, (iv) is v_i

than the next). For this infant, the thalamic and cortical volumes have increased a similar amount to the other infants, suggesting that the bulk growth and microstructural growth may not be entirely synchronous. On average, the changes happen mainly in the middle of the image, which projects to the frontal cortex. Thus the different diffusion parameters seem to highlight growth rates in different sections of the thalamus, which has the potential to identify specific future neurological deficits.

5.4 Discussion

The registration we have defined assumes that the probability of a thalamic region being linked to a particular cortical region as given by the tractography is meaningfully related to how the physical connections in the voxel are arranged. Thus, similarity between timepoints is defined by a similar distribution of probabilities to a given cortical mask region. However, there is no guarantee that the probabilities reflect the mix of connections in the actual brain, although comparable adult studies indicate that they

do. If the probabilities are meaningful, an interesting extension would be to treat these probabilities as memberships to different tissue classes. Thus we could investigate the distributions of NODDI parameters in different thalamic regions.

In future, we could explore a joint registration that segments and registers the thalamus concurrently, based on information from both timepoints. The registration could be compared with known embryology/histology and the predictions of structural organisation tested. In this chapter, the choice of cortical regions was influenced by the atlases available. It would be of interest to add the motor cortex as a target region due to the prevalence of motor-related disabilities in this cohort. From 30-40 weeks EGA, inter-hemispheric connections are being established [82] and future work will examine this. Also, we will use orientation information from the diffusion data to infer the local changes in principal orientation.

To test the growth parameters as early markers of cognitive function, the infants in this study will be followed up with psychological and neuromotor testing. The cortical regions have known functional properties and so a growth disturbance in a certain part of the thalamus is hypothesised to indicate a corresponding specific deficit. To make the work comparable to other work using diffusion-based segmentation of the thalamus [41] we would have to consider a different labelling of the cortex. In [41], the authors have the labels: frontal/temporal; occipital/parietal; motor and somatosensory. Using an atlas with more cortical labels, or manually labelling the cortex, would allow us to further subdivide the thalamus and probe its structure more deeply.

In this work we have demonstrated the correspondence between the sub-thalamic labelling at two timepoints during development. The similarity in the probabilities linking various cortical regions motivates a registration technique that uses this information. We utilised information from tractography and intensity information from T_1-weighted scans in order to constrain the registration by known anatomical priors - i.e. that the spatial pattern of connections remain relatively unchanged in the preterm period. We used this mapping to plot the changes in parameters derived from the diffusion imaging. The high developmental importance of the thalamus suggests that monitoring its development has the possibility of providing early markers of future cognitive health. By mapping local changes in the thalamus and using registration designed especially for this region, this work may lead to more specific functional predictions in this vul-

nerable population.

Chapter 6

Calculating the *g*-ratio *in vivo*

6.1 Overview

While DW MRI is sensitive to microstructure, it is not sensitive to all elements that are present within an imaging voxel. The presence of myelin cannot be reliably inferred from diffusion parameters, but it can be inferred using quantitative T_2 measurements. Here, we propose a method to calculate the *g*-ratio, a measurement of myelin concentration per axon, that combines these modalities.

6.1.1 Contribution

In this chapter, I discuss work that I undertook with Dr Andrew Melbourne. We were jointly responsible for deriving the formula for estimating the *g*-ratio. Some of the work in this chapter was presented at MICCAI 2013 (Section B.2[7]), concerning the calculation of the Myelin Water Fraction (MWF). The work on the *g*-ratio was initially presented at MICCAI 2014 (Section B.2[5]), before being extended and published in HBM (Section B.1[1]). I had a role in editing all of the manuscripts, and I was responsible for pre-processing the diffusion data. The journal paper is appended, in Appendix C. It contains substantial work on magnetic resonance spectroscopy, which is outside of the scope of this thesis.

6.2 Theory

6.2.1 Multi-compartment T_2 measurements

In a given imaging voxel, there are a range of T_2 values. The effect of a contributing compartment can be represented by fitting a single exponential curve to multi-echo

or multi echo-time (TE) data, which has been used to generate quantitative maps of T_2 [66]. Here, we assume that tissue composition can be described by a continuous set of compartments, each with its own associated T_2 distribution undergoing exponential decay.

$$S(n) = \int m(T_2) e^{-n\mathrm{TE}/T_2} dT_2 \tag{6.1}$$

Components with short T_2 are associated with myelin water. This provides a measurement of myelin content, the myelin water fraction — v_{mwf}. This is defined as the proportion of magnitudes, $m(T_2)$, with a $T_2 < 50ms$ [127].

$$v_{mwf} = \frac{\int_0^{50ms} m(T_2) dT_2}{\int_0^{\infty} m(T_2) dT_2} \tag{6.2}$$

6.2.2 Deriving the *g*-ratio

While the bulk amount of myelin may be a useful measurement in its own right, myelin has a fundamental role in insulating axons. An increased level of myelin in a given region may relate to more myelin per axon, or it could mean that there are more axons, with similar levels of myelin. The *g*-ratio is the ratio of internal axonal diameter to the total nerve diameter (axon+myelin), which relates to the electrical properties of axons. For a fibre of constant external diameter, the conduction velocity for impulse propagation is maximised for g-ratio values of 0.6-0.7 [139]. More recent computational estimations of optimal g-ratio have shown that the values are lower in peripheral fibres than for CNS [37]. These estimates are supported by empirical measurement of the *g*-ratio in a range of mammalian species (for instance, the cat has ratios of 0.65-0.77 for its fibres, calculated by electron microscopy [71]). In humans, myelin is an important contributing factor to diseases affecting cognition [61].

To estimate the *g*-ratio, we propose combining measurements from the NODDI model and the T_2 relaxometry. From NODDI, we obtain v_i, the intra-axonal volume fraction, and from relaxometry we estimate v_{mwf} , the volume fraction occupied by myelin water. A myelinated axon has axon radius r_i, and axon+myelin radius r_{out}, with the *g*-ratio being $\frac{r_i}{r_{out}}$. To calculate the *g*-ratio, we consider a cross-section with n parallel axons, modelled as cylinders of unit length. The intra-axonal space is equivalent to:

$$v_i = n\pi r_i^2 \tag{6.3}$$

$$v_{mwf} = n\pi(r_{out}^2 - r_i^2) \tag{6.4}$$

$$\text{Rearranging: } g = \left(\frac{v_{mwf}}{v_i} + 1\right)^{-\frac{1}{2}} \tag{6.5}$$

This can be evaluated, as we can calculate both v_{mwf} and v_i. This model formulation treats axons as having identical diameters, and all of the axons in a region have the same g-ratio. These are simplifications of the underlying structure.

6.2.3 A multi-modal, multi-compartment model

We now have a compartment model that includes a component that is not represented in DW MRI, by using complementary information from T_2 relaxometry. We extend the NODDI model [165] and use a four-compartment tissue model [4].

$$S_{total} = \underbrace{v_{mwf}S_{mwf}}_{\text{Myelin Signal}} + \underbrace{v_i S_i + v_e S_e + v_{iso} S_{iso}}_{\text{NODDI}} \tag{6.6}$$

The model compartment for S_{mwf} describes signal associated primarily with myelin and is estimated by T_2 relaxometry. Because we can now evaluate what fraction of a given voxel is occupied by tissue that is invisible to DW MRI, we can correct our estimates of the NODDI volume fractions. We multiply by $(1 - v_{mwf})$, so that estimated volume fractions will be reduced to reflect better the proportion of a voxel they occupy. We use a '$'$' to denote the estimate from diffusion alone, such that $v_i = (1 - v_{mwf})v_i'$. This facilitates the investigation of to what extent the myelination accounts for increasing v_i in the developing thalamus and other structures. If it is all due to myelin, we would expect the corrected v_i to be constant over time. Note that in previous chapters, we have measured v_i', as there was no correction from the v_{mwf}.

6.3 Methods

6.3.1 Data collection

For this chapter, we used data from 42 preterm infants from the Sparks cohort (Section 3.2). Two were excluded for abnormal cerebral ultrasound, and 3 for motion during

the acquisition. No infants in this study were graded as having moderate or severe injury, according to a white matter scoring system [161]. The remaining 37 (10/27 M/F) preterm infants comprised 15 infants with data acquired at both timepoints, four infants with data acquired at the preterm timepoint, and 18 infants with data acquired at only the term timepoint. Gestational age at birth was 26.27 ± 2.10wks. Seven of these (5/2 M/F) infants had usable longitudinal data. Imaging was carried out on a 3T Phillips Achieva.

The diffusion acquisition is described in Section 3.2. For T_2, whole brain 32-echo multi-component quantitative T_2 imaging was acquired at 1.2x1.2x3mm^3 resolution using a 2D GraSE acquisition at 12ms TE and resampled into the diffusion imaging space.

6.3.2 Estimating the myelin water fraction, v_{mwf}

Here, we use a multiply-refocused echo train MRI acquisition. Because the B_1 is heterogeneous, there is a corresponding heterogeneity in the flip angle α, which produces stimulated echoes along the train. This B_1-inhomogeneity causes the refocussing to be imperfect These echoes can be modelled and corrected for with the Extended Phase Graph (EPG) algorithm [127] to estimate the local refocusing angle. In earlier work, we extended this to use a prior generated from T_1 and FA images, to iteratively solve for α [105]. However, this was not necessary in this Chapter, as we found high spatial homogeneity from estimating α with the EPG. The flip angle was $\geq 90\%$ of the applied angle at all points, which is not expected to adversely affect the fitting [127].

6.3.3 NODDI parameters and regions of interest

In the thalamus, we observed that v_i increased during the preterm period, during a known period of myelination (as in Chapter 4). As discussed, an increase in myelin will raise the measured value of v_i, even if there is no corresponding increase in the number or size of axons. In order to investigate what proportion of the changing v_i is caused by this myelination, we conducted a region-of-interest study within the thalamus. Thalamus segmentations were carried out using the method described in Section 4.2.5, using a preterm-specific segmentation algorithm [33].

The posterior and anterior limbs of the internal capsule (PLIC and ALIC) are regions of interest that we have also previously looked at with DW MRI. The PLIC

myelinates earlier than the ALIC, and it may be possible to perform a similar analysis as in the thalamus, to establish to what extent increasing v_i is due to myelin. We also look at the splenium and genu of the corpus callosum, as they are important in development.

In this chapter, NODDI parameters are fit using NiftyFit [109], rather than the NODDI toolbox.

6.4 Results

6.4.1 Maps of myelin water fraction

We display maps of the myelin water fractions (as defined by Equation 6.2) for a preterm and term timepoint of the same subject in Figure 6.1. In the preterm timepoint (34 weeks 4 days), there is some evidence of myelination in the brainstem. By the term timepoint (40 weeks 2 days) there is more myelin in the brainstem, and the thalamus has also myelinated significantly.

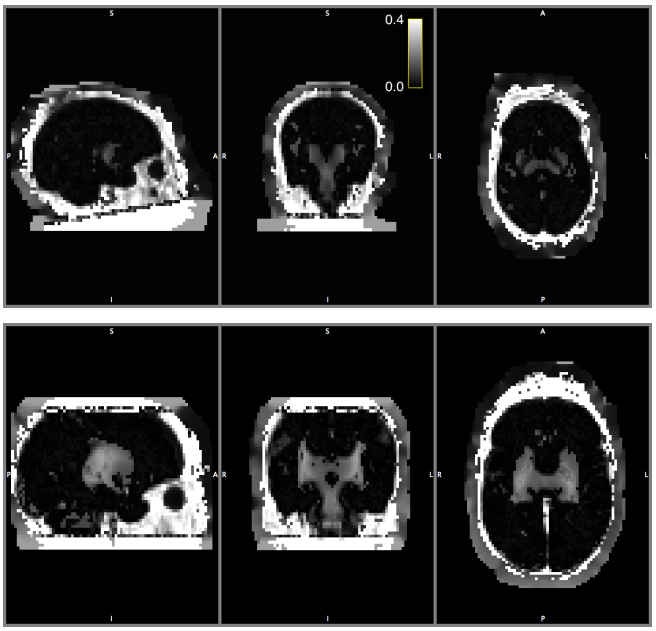

Figure 6.1: This Figure displays the estimated v_{mwf} for a preterm and term timepoint of the same infant (infant 7 in Table C.2. The high-intensity regions outside of the brain are an artifact of the fitting procedure.

6.4.2 Regions of interest

Here, we focus on the utility of the g-ratio in exploring regions of interest we have addressed in previous Chapters. We show the white matter regions of interest in Figure 6.2.

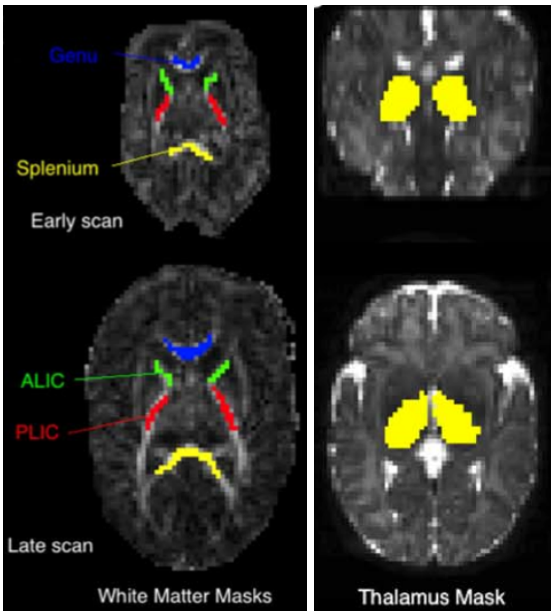

Figure 6.2: The regions of interest for a subject at preterm (top) and term timepoints. The white matter regions are shown on the left, and the thalamus on the right. Figure adapted from Section B.1[1], with permission of Dr Andrew Melbourne.

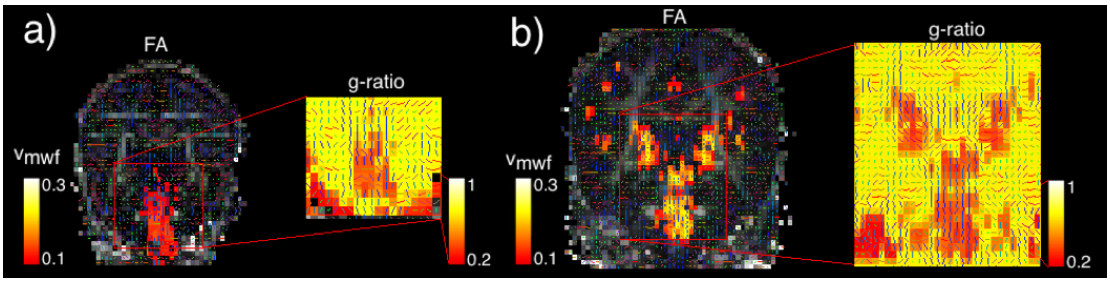

Figure 6.3: Maps of the myelin water fraction and the g-ratio on one of the longitudinal subjects at preterm and term timepoints. Figure reproduced from Section B.2[5], with permission of Dr Andrew Melbourne.

In Figure 6.3, we observe that v_{mwf} is increasing in the brainstem during maturation. The g-ratio is close to unity in unmyelinated regions, as expected.

6.4.3 Longitudinal diffusion and v_{mwf} changes in the thalamus

We display parameter estimates for longitudinal infants in Table C.2. Thalamic T_2 decreases from an average of 203 ± 7ms to 181 ± 7ms (correlation coefficient ρ=-0.84, $p \leq 0.001$). The short T_2 component, associated with myelin, increases in volume fraction from 0.05 ± 0.02 to 0.11 ± 0.02 (ρ=0.87, $p \leq 0.0001$).

We used the correction strategy described in Section 6.2.3 to estimate the intra-axonal volume fraction, while ignoring space occupied by myelin. This suggests that myelination alone does not explain the increase in v_i' in the preterm thalamus, account-

ing for less than a third (0.27 ± 0.06) of the observed change. The g-ratio decreases over time.

Infant	EGA (wks)	v_i'	v_{mwf}	Corrected v_i	g-ratio	T_2 (ms)
1b	26.14					
1p	33.14	0.189 (0.0032)	0.0586 (0.0025)	0.178 (0.003)	0.874 (0.005)	203 (2)
1t	40.14	0.241 (0.0026)	0.115 (0.0027)	0.213 (0.0024)	0.823 (0.0039)	177 (1.9)
2b	25.14					
2p	31.43	0.188 (0.0028)	0.0678 (0.002)	0.175 (0.0026)	0.857 (0.004)	197 (1.1)
2t	42	0.245 (0.0021)	0.132 (0.0028)	0.213 (0.0019)	0.806 (0.0038)	175 (1.5)
3b	25.14					
3p	31	0.175 (0.0026)	0.0289 (0.0011)	0.17 (0.0025)	0.926 (0.0029)	204 (1.2)
3t	42	0.242 (0.0019)	0.11 (0.0024)	0.215 (0.0018)	0.829 (0.0034)	172 (1.7)
4b	27.14					
4p	30.86	0.166 (0.0039)	0.0353 (0.0012)	0.16 (0.0037)	0.908 (0.0034)	208 (0.76)
4t	46.29	0.258 (0.0023)	0.115 (0.0026)	0.228 (0.0021)	0.832 (0.0035)	178 (2.3)
5b	27.14					
5p	29.86	0.154 (0.0026)	0.045 (0.0019)	0.147 (0.0025)	0.88 (0.0047)	215 (1.3)
5t	46.29	0.264 (0.0025)	0.109 (0.0034)	0.235 (0.0024)	0.842 (0.0046)	186 (2.8)
6b	26.29					
6p	31.86	0.183 (0.0037)	0.0712 (0.0023)	0.17 (0.0034)	0.849 (0.0049)	194 (1.7)
6t	40.29	0.216 (0.0026)	0.0899 (0.0033)	0.197 (0.0025)	0.84 (0.0052)	192 (2.8)
7b	26.29					
7p	34.57	0.191 (0.0037)	0.0394 (0.0016)	0.183 (0.0035)	0.911 (0.0037)	200 (1.4)
7t	40.29	0.248 (0.0022)	0.0846 (0.0026)	0.227 (0.0021)	0.863 (0.0038)	185 (2.4)

Table 6.1: Thalamic parameter values for multi-modal MRI. Data is shown at birth (b), early scan (p) and late scan (t). Confidence intervals on the mean are shown in parenthesis. Corrected v_i values are shown after using the correction strategy described in Section 6.2.3. This table is reproduced from (Section B.1[1]) with permission of Dr Andrew Melbourne.

6.4.4 Plotting white matter parameter changes longitudinally

In Figure 6.4, we plot the longitudinal changes in the white matter regions of the PLIC, ALIC, genu and splenium. This contains results for both the longitudinal and cross-sectional parts of the cohort.

The PLIC has increasing v_i ($r = 0.93 p < 1 \times 10^{-7}$) and v_{mwf} (r = 0.86, $p < 1 \times 10^{-8}$) and decreasing T_2 (r = -0.41, p=0.026) with rates of 1%/wk, 0.8%/wk and -1.67ms/wk respectively. The ALIC has slower measured increases in v_i (0.5%/wk, r=0.75 $p < 1 \times 10^{-4}$) and v_{mwf} (0.2%/wk, r=0.72 $p < 1 \times 10^{-5}$). Although measurements of both v_i and v_{mwf} are significantly lower in the ALIC than the PLIC, the difference in growth rate is found to be significant for v_i but not for v_{mwf}.

The genu and splenium of the corpus callosum have similar parameter values (Figure 6.4), and both have low v_{mwf}. The genu increases significantly in v_i and v_{mwf} (v_i: 0.8%/wk r=0.58, p=0.015) (v_{mwf}: 0.1%/wk r=0.52, p=0.004), and decreases in T_2 (-

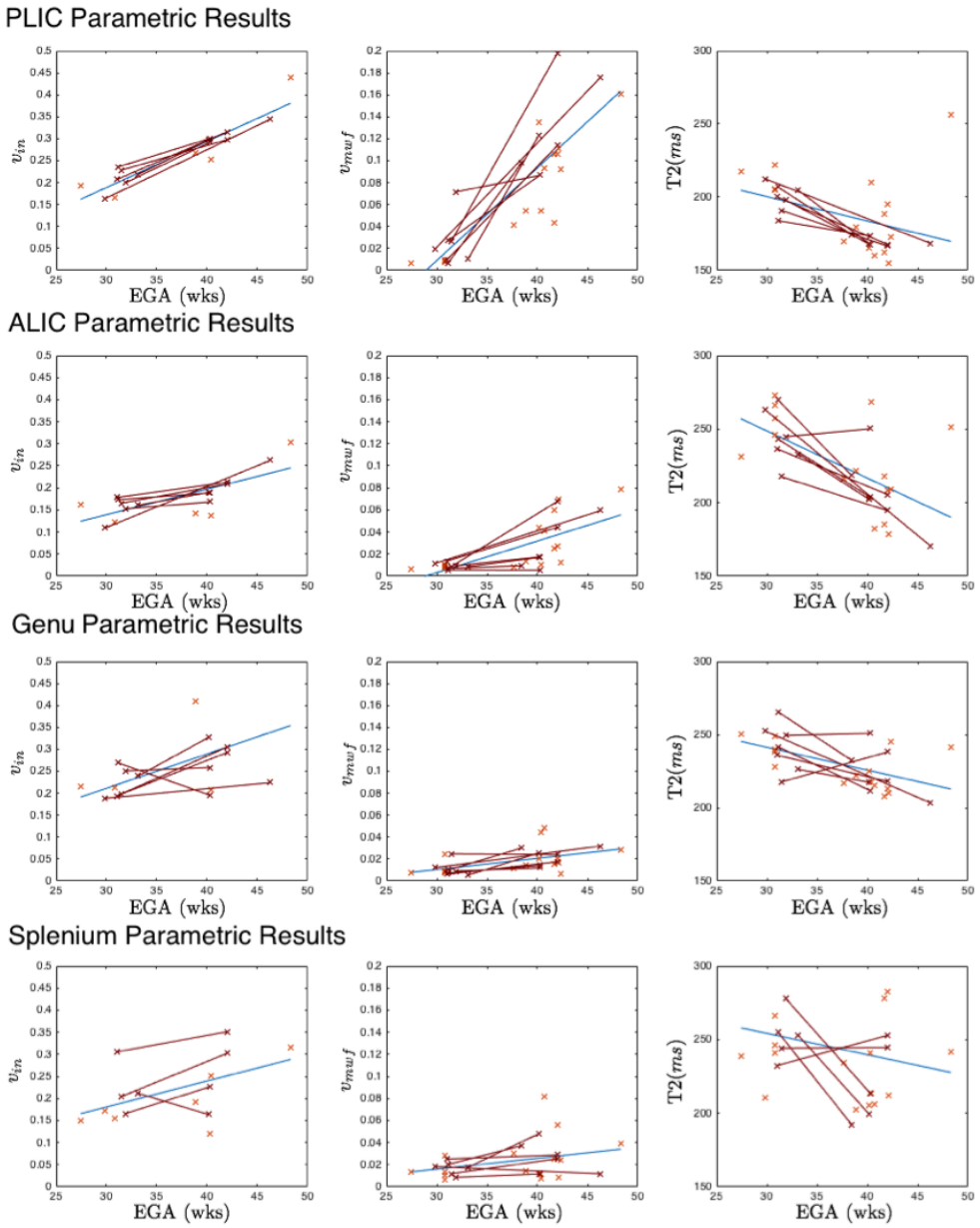

Figure 6.4: Here, we plot the ROI average values for the corrected intra-axonal volume, v_i, v_{mwf}, and T_2. Longitudinal data are shown in red, connected intra-subject by red lines. Cross-sectional data is shown in blue, with a blue trend line. This table is reproduced from (Section B.1[1]) with permission of Dr Andrew Melbourne.

1.35ms/week, r=0.55,p=.002). Changes in the splenium all take the same sign, but are not significant. The changes in the genu are larger than for the splenium, but this difference is not significant.

6.5 Discussion

In this work, we have shown that acquiring measurements of g-ratio is feasible in a neonatal population. We have calculated a 'corrected' intra-axonal volume fraction, that properly accounts for space that is taken up by myelin water. We have used this on longitudinal and cross-sectional data to examine regions of interest.

In the thalamus, we showed in Chapter 4 that there was a significant increase in v_i', with no corresponding change in ODI. In this Chapter, we have shown that myelination accounts for approximately one third of this observed change. The remaining change could be because of increasing axonal density, or other changes in the composition of the tissue.

In the white matter, the contribution of myelination to measured values of v_i' is low, because there is little myelin except in the PLIC. The change in v_i' can be attributed more to proliferation in axons and glial cells. The v_{mwf} values in the PLIC are high, commensurate with early myelination in this region, in contrast to the ALIC. In the splenium and genu of the corpus callosum, there were no statistically significant differences in the rates of parameter change, in contrast to other work [123]. However, the baseline of our measurements is relatively narrow, and there is insufficient data to make strong claims about regional differences in trend.

In analysing the trends over the regions of interest, the data can only support a linear model. This is partly because the data points are not evenly sampled (by the design of having two timepoints, ages in the range $\sim$35-38 weeks have no data). Also, the wide variance in parameter values and rates of change between subjects introduces challenges. Overall, it is certain that the true maturation pattern is not linear. This has been shown in similarly-aged infants [14], but there is also a logical component: there is no myelin in many regions at birth, and no linear fit can incorporate the time period before which myelination begins. To reliably map out a more intuitively plausible non-linear curve (e.g. the Gompertz curve [134]) would require more data and a better distribution of gestational ages in the study to reliably plot a non-linear model.

The low number of infants scanned in this study is, as alluded to, a major limitation. Apart from obvious challenges in infant recruitment and scanning, it is unfeasible to image given subjects many times in their stay in the NICU. Although MRI is virtually harmless, there is still significant disruption involved in preparing for a scan, even

in an MR-compatible incubator.

In terms of the model, the simplicity of our g-ratio estimation does not necessarily agree with known histology. In reality, there is a distribution of g-ratios and of axon calibres. One method of modelling the distribution of g-ratio estimates is explored in [158]. There is, though, a trade-off between how well a model adheres to reality, and its interpretability.

In this chapter and published work, we have furthered the use of multi-modal models of diffusion and complementary modalities. Work further investigating the relations between histology and the g-ratio, as in [146], would increase the confidence in the measurements. However, there is a clear purpose to combining complementary modalities.

Chapter 7

Measuring the radiality index in preterm infants

7.1 Introduction to the cohort

This dataset, acquired from Washington University in St Louis, was originally obtained intended to measure the effects of caffeine, delivered within the NICU as a neuroprotective agent. While the caffeine trial did not show any effect on infant growth, the infants in the cohort happened to be in two distinct conditions within the NICU. Some of the infants were in open wards, and some in private wards. These were distributed by chance (because of ward crowding), and not by financial means. These infants showed a difference in language processing, with infants in private wards showing worse language processing skills (findings not yet published).

This cohort has been used to investigate cortical folding measures [138] and to investigate the synchrony in maturation in [142]. There are also a range of publications in preparation about the effect of the NICU environment on auditory development.

7.1.1 Contribution

This work is *in-press* as "Investigating the maturation of microstructure and radial orientation in the preterm human cortex with diffusion MRI. ", expected to be published 2017 in NeuroImage.

7.2 Introduction

For preterm infants, birth occurs during a critical time in neurodevelopment. This disruption has wide-ranging effects, with preterm infants showing reduced development

of the cerebral cortex by term equivalent age [2]. During early development, cortical neurons migrate radially outwards, on glial cells, towards the pial surface. This populates the cortex [32] and causes a highly directional, coherent, columnar microstructural environment, which can be seen with DTI as tensors with high FA, oriented radially to the cortical surface [102]. In subsequent growth within the cortex, cross-connections develop, as dendrites and axons elaborate and obscure the underlying radial structure. In DW MRI, this manifests as a longitudinal reduction in FA [102], and less-aligned diffusion tensors. Following approximately 25 weeks gestation, a large majority of cortical folding and growth of cortical connections occurs. The cortex produces gyri and sulci, which occurs mostly postnatally for preterm infants. While the folding does not, in itself, change the microstructure, there are effects on DW MRI measurements, with microstructural maturation correlating with local cortical growth [14]. Gyrification of the cortex will cause more partial volume effects between the cortical grey matter, and either the underlying white matter or the outlying cerebrospinal fluid (CSF). CSF in particular has different diffusion properties to tissue, and so removing the confound of CSF partial volume is important.

In recent times, technological aspects of DW MRI have advanced significantly. There is increasing sensitivity to diffusion (characterised by the b-value), more directions in a scan, and improved resolution. These improvements have spurred recent interest in diffusion within the cortex — both in terms of the DTI parameter values, and the directionality of water diffusion. DW MRI can now detect that the average direction of cortical diffusion is radial, even in adults [103]. This study defined the "Radiality Index", which measures how orthogonal to the cortical surface the principal diffusion direction is. The orthogonal direction is called the "surface normal", and the radiality index is defined mathematically as the magnitude of the inner product of the principal direction of diffusivity with this surface normal vector. This radiality index was shown to correspond with known histology, and was shown to be greater than the value that would be expected by randomly-aligned tensors (0.5) in all except small regions of the cortex. In addition, Truong et al [151] have shown that the DTI parameters and the radiality index have a dependence on cortical depth that is detectable *in vivo*. In infants, it has been shown using the ball-and-stick model that radiality after preterm birth is higher (≥ 0.5) towards the anterior cortex, while it is ~ 0.5 in other regions [107].

In addition to improvements in the DW MRI acquisition, there have been advances in modelling the diffusion signal. With more diffusion data, it is possible to fit multiple compartments within a single voxel, so that the signal is a linear combination of the diffusion signals from structurally different environments. For example, the signal within white matter adjacent to the CSF could be modelled as combining an anisotropic tissue compartment with an isotropic tensor (ball) of fixed diffusivity [25]. The "DIstribution of 3D Anisotropic MicrOstructural eNvironments in Diffusion-compartment imaging" (DIAMOND) model [137] is an example of this approach. DIAMOND enables the assessment of the relative signal fraction of each compartment, as well as compartment-specific characteristics such as the compartment fractional anisotropy (cFA), and the compartment mean diffusivity (cMD).

While some advanced diffusion models have been used in the preterm population [87, 57], this richer characterisation of the microstructure has not yet been fully explored. In this manuscript, we quantify the trajectories of development for cortical radiality as a function of the cortical region. By using structural and diffusion-weighted MRI in tandem, we present the first longitudinal assessment of the radiality index in preterm infants. DIAMOND offers an explicit modelling of partial volume to deal with small brains and changing cortical convolution, while the tensor component in the model can be used to assess the principal direction without the confound of CSF. Measuring the deviation in growth patterns may be of use in clinical prognosis.

In this work, we quantify the longitudinal changes in radial diffusion within the preterm cortex for the first time *in-vivo*. These measurements are of interest as an insight into general neurodevelopment, as well as further elucidating our knowledge of possible effects of prematurity.

7.3 Methods

7.3.1 MRI acquisition and participation

We use infants born at fewer than 34 weeks completed gestation, recruited from the St Louis Childrens Hospital Neonatal Intensive Care Unit (NICU) between 2007 and 2010. These infants were scanned at up to four different age intervals postnatally: $<$30, 30-31, 34-35, and 38-40 weeks gestational age. The average gestational age at birth was 26.9 ± 2.1 weeks, with the range being 23-33 weeks. Due to health complications and

challenges inherent in scanning infants, not all of the scans were performed — of 105 surviving infants with no intra-ventricular haemorrhage, 89 subjects had useable MRI data from one more more scanning sessions. Of these, 37 had data from a single point in time; a further 37 were scanned at two timepoints, 12 had three timepoints and 3 were scanned at all four timepoints. Images were acquired when infants were resting or asleep, after feeding, wrapping and delivery to the MRI machine as outlined in [100]. Studies were approved by the Washington University Human Studies Committee.

The MRI was acquired with a 3-T Siemens TIM Trio system (Erlangen, Germany) using an infant-specific, quadrature head coil (Advanced Imaging Research, Cleveland, OH, USA). The structural scans were a T_2-weighted fast spin echo sequence (repetition time (T_R) 8500 ms, echo time (T_E) 160 ms, $1\times1\times1\text{mm}^3$ voxels) and a rapid gradient echo T_1-weighted acquisition with resolution of $1\times1\times1$ mm^3 voxels (T_R/T_E:1500/3ms).

The diffusion acquisition consisted of 48 gradient directions with b-values ranging to cover values from 0 to 1200 s/mm^2. The acquisition parameters were: T_R 13,300 ms, T_E 112 ms, 1266 Hz/Px bandwidth, 128 mm field of view (FoV), $1.2 \times 1.2 \times 1.2$ mm^3 voxels. Total acquisition was approximately 60 minutes in duration. The b-values were: 0, 0, 0, 75, 80, 85, 150, 160, 171, 225, 240, 257, 300, 320, 342, 375, 400, 428, 450, 480, 514, 525, 560, 600, 600, 640, 675, 685, 720, 750, 771, 800, 825, 857, 880, 900, 942, 960, 975, 1028, 1040, 1050, 1114, 1120, 1125, 1200, 1200, and 1200 mm^{2}s^{-1}. We inspected each acquired volume and discarded those with significant motion artifacts from movement during the acquisition, removing an average of 3.0 ± 3.5 volumes per infant. We co-registered the scans affinely to an average $b = 0$ image in order to eddy-correct and to correct for motion between acquisitions.

The data processing pipeline is illustrated in Figure 7.1, with each step being detailed below.

7.3.2 Image Segmentation

As intermediate steps in this investigation, we produced a surface mesh of the cortex and labelled the cortical lobes for each subject. The cortical mesh was computed from a probabilistic segmentation of the cortical grey matter. For this, we initialised a preterm-specific segmentation algorithm [33] with a probabilistic atlas of the develop-

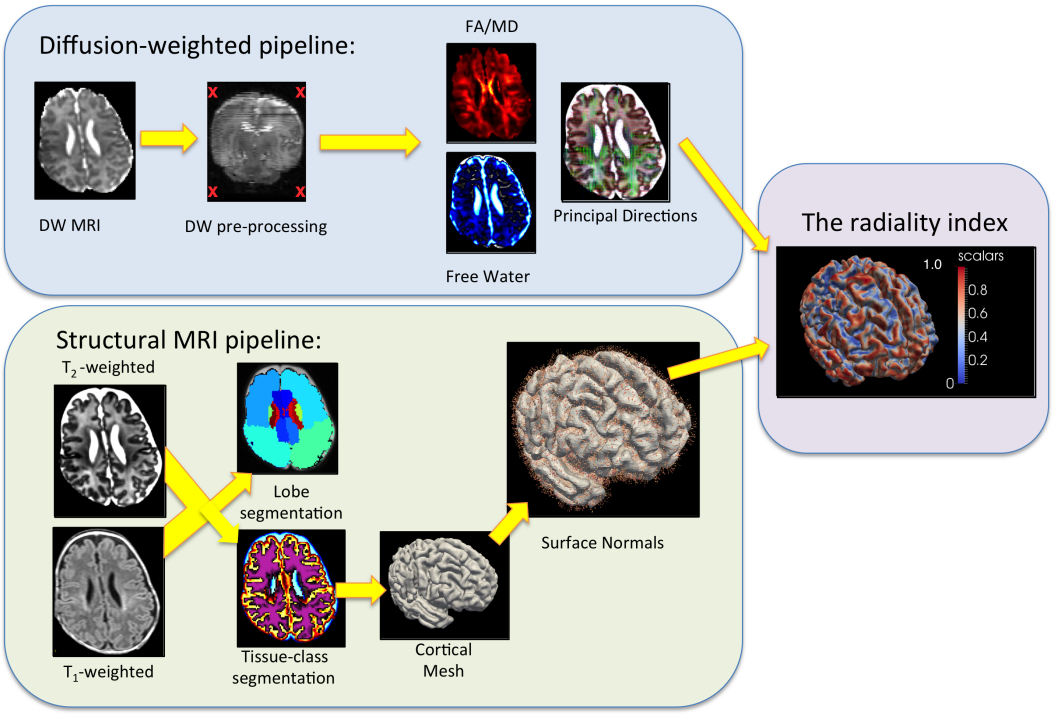

Figure 7.1: The data-processing pipeline. Within-subject, within-timepoint, data was aligned into the space of the T_2-weighted image. The tissue-class segmentation used priors from an age-specific atlas to initialise an expectation-maximisation segmentation on the structural image. This segmentation was split into hemispheres, and we extract the largest connected component of the white matter and cortex segmentations, to ensure that the topology was correct. We then used CRUISE to generate a cortical surface. The normal vectors were calculated from the triangular faces, a random subset of which is shown in the 'surface normals' above. The diffusion data was processed using DIAMOND to generate free-water maps and a tensor map for the tissue component, and also with DTI.

ing brain [85]. This was performed on T_2-weighted data, because of the high contrast between cortex and white matter, and produced a segmentation of the brain into white matter, cortical grey matter and CSF. We further segmented the brain into the occipital, parietal, frontal and temporal lobes using Geodesic Information Flows (GIF) [34], using a newborn atlas [64]. We combined the tissue segmentation with the maps of the lobes to produce cortical segmentations with a lobe label, to investigate diffusion parameters on a regional basis.

7.3.3 The DIAMOND model

The outlying cerebrospinal fluid has a large impact on diffusion readings in the cortex. To explicitly model this partial volume, we could have employed the ball-and-stick model [23] to assess the diffusion orientation in each voxel. However it does not provide diffusion characteristics of the tissue compartment, because the stick parameters are fixed and identical throughout the brain. By contrast, DIAMOND provides both:

1. the diffusion principal orientation to calculate the radiality index, and

2. the compartment-specific parameters (cFA, cMD) similar to those of DTI, to evaluate microstructure properties.

We used the DIAMOND model [137] with two compartments: an isotropic diffusion compartment with fixed diffusivity to model CSF contamination, and an anisotropic tissue compartment to model diffusion within the tissue. DIAMOND models the anisotropic diffusion compartment with a statistical distribution of diffusion tensors to account for the heterogeneity of the underlying microstructure. Assessing the average tensor of the distribution allows characterisation of the average diffusion characteristics in the compartment, from which compartment-specific parameters (compartment FA and compartment MD, denoted cFA and cMD respectively) can be inferred. Moreover, DIAMOND provides an index describing the intra-compartment heterogeneity, based on the concentration of the distribution of tensors. Other multi-compartment models often require higher b-values (for example, NODDI [165] recommends including b-values of 2000mm^{2}s^{-1} for infants), and so were unsuitable to our data.

7.3.4 Calculating the Radiality Index

The radiality in a given voxel was determined from two separate measurements. One is the principal diffusion direction, which we compute using both DTI and DIAMOND. This results in a radiality index for each model, to compare DIAMOND and DTI for this application. The other is to calculate vectors that are locally normal to the cortical surface (pointing outwards). A high radiality index arises when this surface normal is approximately collinear with the principal diffusion direction, and lower when the directions diverge.

To calculate the cortical mesh of the cortical surface, we used implicit surface

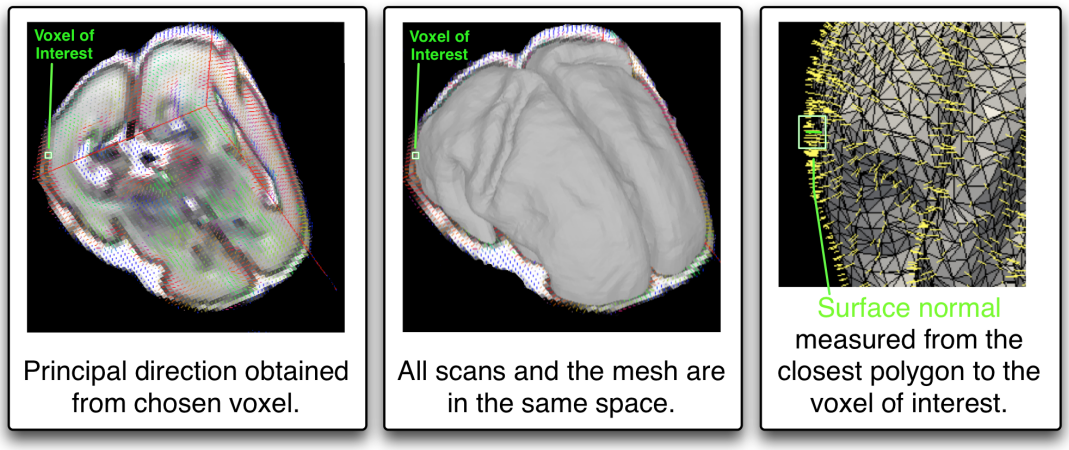

Figure 7.2: This figure demonstrates the process for acquiring the principal diffusion direction $\mathbf{v}$ and surface normal $\mathbf{r}$ for a given voxel. For a given voxel of interest, we first determine $\mathbf{v}$ by fitting the desired diffusion model (leftmost panel — note that this view is displaying information on 3 axes, not one slice). We then identify the closest triangular mesh face to this point, using the surface mesh. By taking the cross-product of any two edges of this triangular face, we obtain $\mathbf{r}$. In calculating $|\mathbf{r}.\mathbf{v}|$, it is not important to ensure that $\mathbf{r}$ faces outwards, because the diffusion acquisition only tells us about water diffusion along a line segment, not in a particular direction.

evolution (CRUISE) [67] on the tissue segmentations, and topology-corrected the mesh with a fast-marching algorithm [20]. The surface mesh inherently defines a normal vector at each triangular face (the direction is given by taking the cross-product of any two edges of each triangle).

For each voxel in the diffusion parameter maps, the radiality index is given as:

$$\frac{|\mathbf{r}.\mathbf{v}|}{||\mathbf{r}||||\mathbf{v}||} \tag{7.1}$$

This is the magnitude of the dot product of the radial vector nearest the voxel $\mathbf{r}$ with the principal eigenvector of the diffusion tensor, $\mathbf{v}$, normalised by the vector lengths. This process is illustrated in Figure 7.2

The small size of the infant brain, relative to the scanning resolution, introduces challenges in computing a surface normal for each voxel in the cortex. We were aiming to measure the changes within the cortical tissue caused by maturation, without the confound of morphological change. To compute the radiality within a voxel, we must ensure that the tissue is homogeneous (i.e. no partial volume with another, folded, part of the cortex) and that the surface normal is coherent at that point (i.e. the surface is

relatively flat within the voxel). To eliminate the partial volume with cortical tissue, we excluded regions in the sulci. The sulci not only have more partial volume, but are also more curved than the gyri, so excluding these provided more coherent orientations of the normals. To perform this masking, we computed the mean curvature over the cortical surface, and analysed regions only where the surface was convex (mean curvature <0). This means that we ignored the radiality in the sulci, in favour of having a flatter surface and more reliable radial vectors.

7.3.5 Statistical Approach

For data analysis, it was necessary to account for missing data, the unbalanced sampling of time-points, and correlations in data from the subjects who are scanned longitudinally. To do this, we used models with fixed and random effects — known as mixed models. This type of modelling has been used to build normative curves for neurodevelopment, using DTI [133, 132]. Fixed effects quantify the population-level effects, while random effects allow the model parameters to vary on a per-subject basis.

In order to analyse which effects were significant in the models, we used backwards elimination of non-significant effects of a linear mixed-effects model. For a given diffusion metric y, in a given cortical lobe, of subject i at time t, we fitted a model that included available subject information: the sex (S_i), gestational age at birth (GA_i), the estimated gestational age (t) and the hemisphere the measurement was taken in (H). The random effect is an intercept that varies on a per-subject basis (b_i) and ε is an error term.

$$y_i(t) = \alpha_0 + \alpha_1 S_i + \alpha_2 H + \alpha_3 GA_i + \beta t + b_i + \varepsilon \tag{7.2}$$

To compensate for multiple comparisons with the 6 diffusion parameters we analysed ($\{$DTI/DIAMOND$\}$ $\times\{$FA/MD/Radiality$\}$), we fixed the threshold for including fixed effects at $0.05/6$ (Bonferroni correction). We performed all data analysis in R (v3.2.1), using the package "lmer" (v1.1.12) [19]. We used "lmerTest" [88] for performing the backwards elimination.

7.4 Results

The automatic segmentation and subsequent mesh generation produced cortical meshes for all timepoints in the study. For an example of typical longitudinal progression in this study, see Figure 7.3.

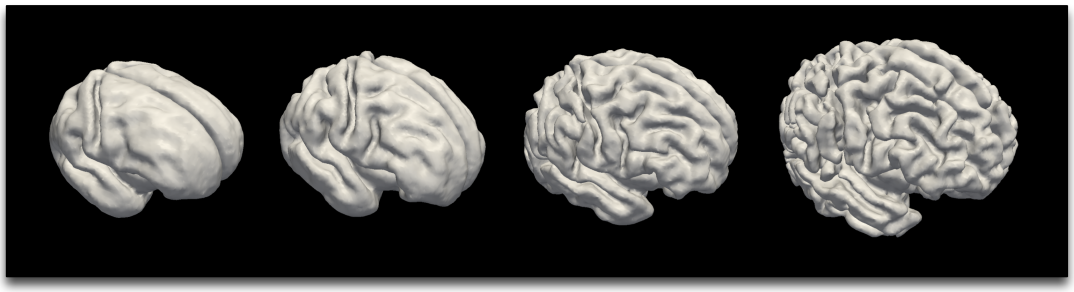

Figure 7.3: This figure displays the cortical mesh at four timepoints for the same infant. The infant was born at 28 weeks estimated gestational age (GA), and these scans are, from left-right, at 28, 30, 33 and 38 weeks GA respectively. The cortex has progressed from broadly flat to highly convoluted during the ten postnatal weeks between images.

For all of the regions and diffusion parameters tested, the elimination of non-significant effects removed the effects of sex, hemisphere and gestational age at birth. Thus, for each parameter and in each region, the preferred model was a linear model that depended on time. The parameters for the model are shown in Table 7.1.

	Intercept±SE (at 27 weeks)	Slope±SE (per week)	Intercept±SE (27 weeks)	Slope±SE (per week)
	cFA		FA	
Frontal Lobe	0.175 ± 0.003	-0.0089 ± 0.0003	0.168 ± 0.002	-0.0033 ± 0.0002
Occipital Lobe	0.159 ± 0.004	-0.0089 ± 0.0004	0.194 ± 0.004	-0.0058 ± 0.0004
Parietal Lobe	0.177 ± 0.003	-0.0094 ± 0.0003	0.180 ± 0.002	-0.0053 ± 0.0002
Temporal Lobe	0.191 ± 0.003	-0.0107 ± 0.0003	0.187 ± 0.003	-0.0049 ± 0.0004
	cMD/10^{-3}mm^{2}s^{-1}		MD/10^{-3}mm^{2}s^{-1}	
Frontal Lobe	1.13 ± 0.008	-0.0024 ± 0.0009	1.37 ± 0.009	-0.0098 ± 0.0009
Occipital Lobe	1.12 ± 0.011	-0.0032 ± 0.0010	1.41 ± 0.013	-0.0111 ± 0.0014
Parietal Lobe	1.18 ± 0.008	-0.0054 ± 0.0008	1.38 ± 0.008	-0.0140 ± 0.0008
Temporal Lobe	1.10 ± 0.009	-0.0029 ± 0.0010	1.40 ± 0.009	-0.0124 ± 0.0001
	DIAMOND Radiality		DTI Radiality	
Frontal Lobe	0.961 ± 0.008	-0.0189 ± 0.0008	0.898 ± 0.008	-0.0126 ± 0.0009
Occipital Lobe	0.952 ± 0.009	-0.0323 ± 0.0008	0.859 ± 0.009	-0.0206 ± 0.0009
Parietal Lobe	0.945 ± 0.008	-0.0227 ± 0.0008	0.891 ± 0.008	-0.0158 ± 0.0008
Temporal Lobe	0.901 ± 0.008	-0.0190 ± 0.0009	0.844 ± 0.008	-0.0124 ± 0.0008

Table 7.1: This table shows the coefficients for the models of the diffusion parameters. Note that for each of the diffusion parameters, the preferred model took the form of $y_i(t) = \alpha_0 + \beta t + b_i + \varepsilon$, and thus effects from hemisphere, GA at birth, and sex were not found to contribute significantly to the model fit. In this table we display the intercept at 27 weeks (α_0) and the slope β.

Figure 7.4 shows that fractional anisotropy decreased for both the DIAMOND and DTI models. The slopes were greater in magnitude (see Table 7.1) for the DIAMOND model ($p < 10^{-7}$ for all regions, using a t-test) than the DTI model.

For mean diffusivity, the DTI model had a significantly greater intercept than the DIAMOND model's cMD ($p < 10^{-9}$) for all regions). The slope was of greater magnitude for the DTI model ($p < 10^{-9}$) for all regions). See Figure 7.4, and Table 7.1.

In Figure 7.5 we present the cortical radiality for the DTI and DIAMOND models during the preterm period. The frontal and temporal lobes decrease at statistically indistinguishable rates from each other ($p = \{0.93|0.86\}$ for $\{$DIAMOND$|$DTI$\}$ respectively), but significantly lower rates than the parietal lobe and the occipital lobe ($p < 10^{-4}$). The occipital lobe decreased with the largest rate for both DIAMOND and DTI ($p < 10^{-4}$). The DIAMOND model had a greater rate of decrease than the DTI model in all regions ($p < 10^{-8}$), which is consistent with DIAMOND reducing the impact of CSF contamination. The intercepts were higher in DIAMOND ($p < 10^{-7}$) than for DTI.

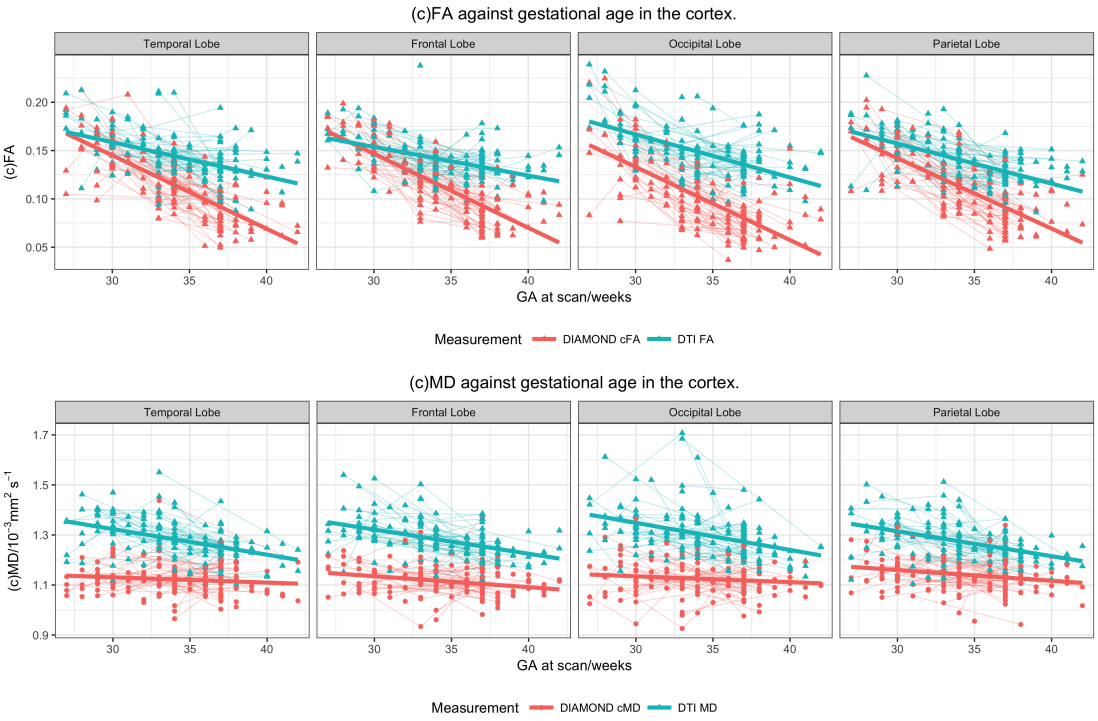

Figure 7.4: The mean values for (c)FA and (c)MD in the DIAMOND and DTI models. Dashed lines connect longitudinal measurements from the same infant. The trend lines are the population trends from the linear models in Table 7.1, which were modelled by extracting the coefficients from the model fits, and predicting with random effects set to 0.

7.5 Discussion

Because cortical folding and neuronal elaboration are broadly complete for infants delivered at term, preterm MRI offers a unique chance to image these maturational processes *ex-utero*. The rapid changes in the cortex during the perinatal period are critical events in neurodevelopment. In this work, we have evaluated the radiality index and diffusion tensor parameters in preterm infants on a longitudinal basis. We have shown a decrease in cortical radiality, cFA and FA in each lobe of the cortex, with region-specific rates. None of the models showed any sex-dependence, in agreement with [163].

In terms of diffusion tensor parameters, both DTI and DIAMOND showed expected reductions in (c)FA, which is theorised to relate to elaboration of the microstructural environment and consequent reduction in anisotropy [102]. The MD decreased significantly more in the DTI model than for the cMD, which could be attributed to the DIAMOND model having an explicit model of CSF partial volume. This feature allows the DIAMOND model to remove the confound of CSF partial volume in the

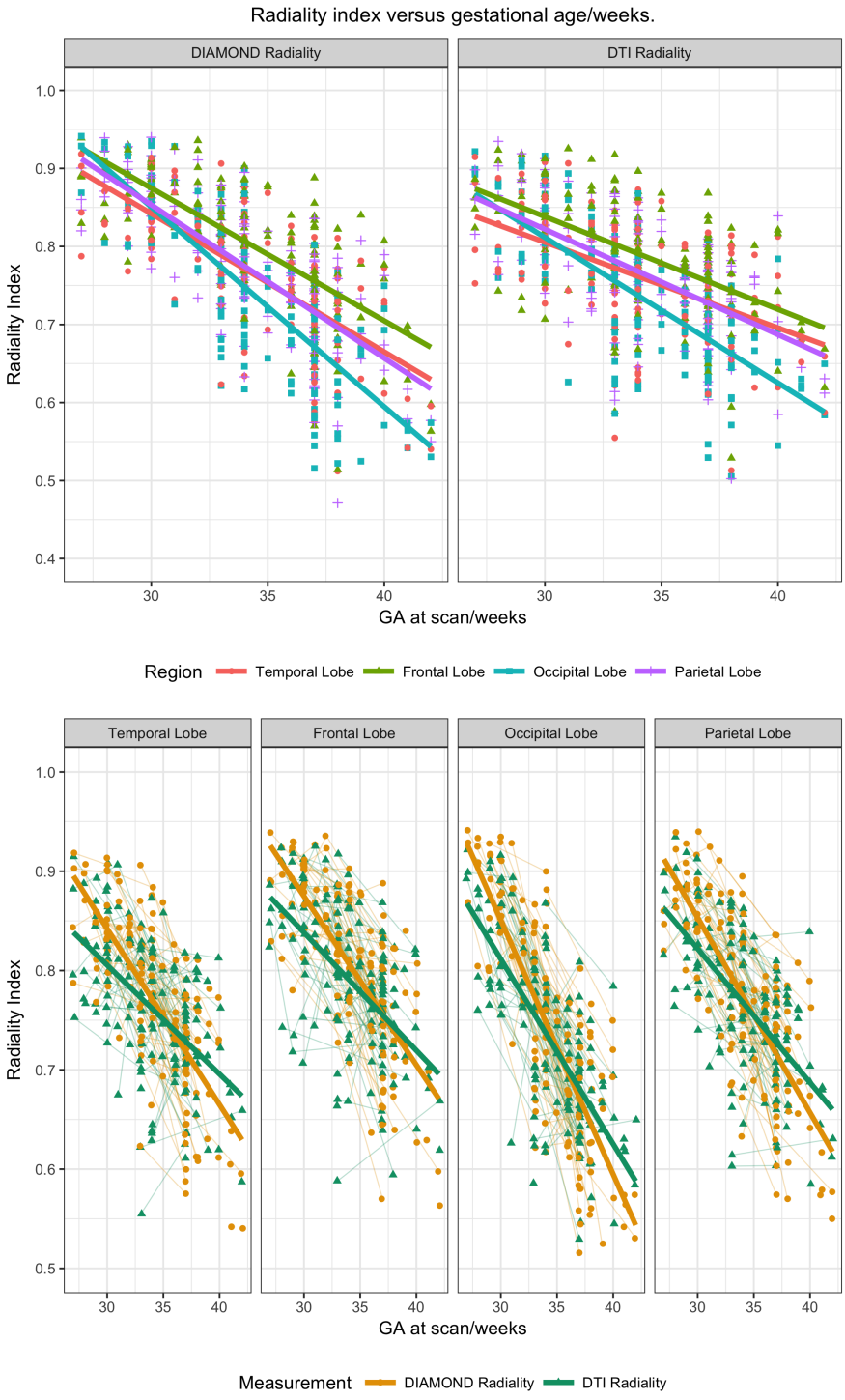

Figure 7.5: The mean values for the radiality index for DIAMOND and DTI models in each lobe. Bold lines are linear trendlines, with parameters from Table 7.1. DTI and the DIAMOND model show similar trends in radiality (top figure), with the rate of change being greatest for the occipital lobe. The DIAMOND model shows significantly greater changes than the DTI model over the time period for each region.

cortex, and examine only the tissue.

The radiality index is close to unity at early timepoints in the study for both DIAMOND and DTI, reflecting the highly-ordered and radial nature of the supporting glial cells. As the cortex matures, overlying fibres are added to this radial substrate. We suggest that the reduction in measured radiality reflects, at least in part, this microstructural change. At early timepoints, the extra-cellular water is hindered orthogonal to the fibres, and thus has a principal direction of diffusivity that augments the radial structure of the intra-cellular compartment. This extra-cellular space reduces significantly in development, which contributes to the measured decline in radiality. We found that the rate of change of radiality depends on the lobe, with the occipital lobe having the highest rate of change. None of the MD, cMD, FA or cFA had the greatest rates of change in the occipital lobe, which is evidence that the radiality index is not solely reflecting these known parameters, and thus that this parameter provides complementary information to traditional diffusion measures.

In [49], the authors graded the "gyral development score" as a function of GA. They found that the medial occipital area develops fastest, while the frontal lobe (minus the area of the central sulcus) and anterior part of the temporal lobe develop slowest. The parietal lobe, the posterior part of the temporal lobe, and the occipital lobe (minus the medial area) were in between. This fits with our finding with the radiality index: that the occipital lobe develops the most rapidly, and the frontal and temporal lobes have the smallest rate of change. This also suggests that breaking down the cortex into smaller regions of interest would also be of interest. The fact that our measured rates correlated with trends in gyrification is also in agreement with the finding that microstructural maturation is concurrent with local macrostructural growth [14].

7.5.1 Comparing DIAMOND and DTI

Comparing the values for the DIAMOND and DTI radialities, we observed that the DIAMOND model measured higher radialities at early timepoints, and lower at later timepoints than DTI. This could, perhaps, be attributed to an increased sensitivity to the structure by using the multi-compartment formalisation of DIAMOND. Being able to explicitly model the partial volume is important within the rapidly-folding cortex.

The cFA reached a lower value than the FA by term-equivalent age, which was not

expected. It is likely that the DIAMOND model is more able to account for measurement noise than the tensor formulation, which is an advantage in the low SNR regime of the infant cortex. This could be because of the spatial regularisation in the fitting of the DIAMOND model, which acts to reduce spuriously high FA values caused by noise.

For the fractional anisotropy and radiality, DIAMOND displayed significantly higher changes in parameter values than the DTI model. However, the changes in cMD were significantly lower in magnitude than in the DTI model. This is likely to be because of less partial volume with CSF, so some fraction of the observed MD change is likely to be spurious.

7.5.2 Limitations

The radiality calculated at each voxel depends on many factors, including the accuracy of the cortical mesh, the quality of alignment between modalities, and the diffusion-weighted data at a given voxel. The radiality is bounded between 0 and 1, with values expected to be near to 1 in much of the brain (entirely radial diffusion). Thus, errors are, especially at early time-points, expected to *underestimate* the radiality, causing the bias in the error to be time-dependent.

Despite the concurrence in radiality change with development, relating the parameter directly to the microstructure is challenging. While the intuitive picture is of radiality decreasing as cells are added to the cortex, we know that these fibres are being added to a persistent radial substrate. Because this direction persists, we may have expected that the radiality would be constant throughout development. Some element of the reduction in radiality may be because the restrictions lead to more attenuation in all directions, and hence a noisier signal, which may perturb the principal direction of the diffusion model. However, it is highly implausible that this confound would cause the major finding of the large reduction in cortical radiality from 27-42 weeks gestational age.

Several scans had some evidence of motion artifacts. While all data was individually inspected for quality, different infants had different numbers of diffusion volumes. Similarly, there are some cortical meshes with unphysical folds or ridges introduced by the algorithm. However, any automatic procedure will have some errors against the

gold-standard of manual segmentation, but manual segmentation would have been impractical and time-consuming for this number of scans. While these issues affect the presented work, this does not detract from our overall findings of large reductions in cortical radiality during development.

In terms of statistical approach, other work in this domain has used *non*-linear mixed effects models, often with parameters that have biophysical interpretations [133, 132]. These nonlinear models require a much greater longitudinal range that that available to us, and thus, a linear model is appropriate, and can be seen as a local approximation to a non-linear curve. While adult radiality values could be used as a fixed asymptote, this would make too many assumptions about both the parameter values throughout childhood, and the comparability of this method to published work on adults, which uses different acquisitions and processing pipelines.

7.5.3 Future Work

We could extend our work in measuring radiality in large regions of the cortex to smaller regions of interest, such as in [103, 47]. We did not, partly because automatic segmentation tools for cortical analysis of infants lag their adult counterparts, owing in part to the peculiar difficulties, so the labels are not available. It would also have the downside of reducing the statistical power available to compare the regions by reducing the number of voxels in each.

While the current work characterises a cohort of preterm-born infants, more investigation would be required to use an individual's radiality scores as a basis for prognosis. Future work could go further in defining normal values for this index, and correlating scores with clinical outcome.

Although our DW acquisition had a high resolution, the b-value was limited to $\leq 1200\text{mm}^2\text{s}^{-1}$. Higher b-values may warrant using a more sophisticated model of diffusion within the cortex. An intuitive model would be a directional component oriented radially, that is augmented by an oblate disk orthogonal to this axis, representing the new fibres. This type of model would separate contributions to the radiality as coming from radial fibres or perpendicular additions. Our model has, however, the advantage of being comparable to other radiality studies.

7.6 Conclusions

In this manuscript, we have produced the first analysis of the change in cortical radiality in preterm neonates, as imaged by DW MRI. During the preterm period, the geometry of water diffusion matures rapidly from its almost entirely radial state at 27 weeks gestational age. The radiality index shows promise as an early marker of cortical development, and offers a quantification of the observed decrease in directional coherence. The DIAMOND model offers increased sensitivity to these changes when compared to the DTI model.

Chapter 8

Microstructure in the EPICure cohort

8.1 Details of the EPICure cohort

The EPICure study group is a consortium of clinicians and scientists who authored a study of all the infants born extremely preterm in the UK during 1995. This cohort has been followed since birth, with a wide-ranging and thorough set of psychological and physical examinations. It is only now, at 19 years of age, that the group have had MRI scans. This cohort was important in establishing the difficulties of growing up after extremely birth [160], through early childhood [98] and into adulthood.

8.1.1 MRI acquisition

Recruitment was open to all infants born extremely preterm in the UK and Ireland from March to December, 1995, as described in [160]. This study was continued to collect psychological, physiological and other markers of subject health and development, including at 6, 11, 16 and 19 years of age. These measurements were compared with a matched cohort recruited from school classmates. EPICure@19 is the source of the MRI scans we examine in this study, performing MRI on this cohort for the first time at age 19.

Individuals were imaged using a Philips 3 T Achieva. The 3D T_1-weighted volume was acquired at $1\times1\times1$ mm^3 isotropic resolution (TR/TE = 6.78/3.06 ms) We acquired diffusion MRI in three shells, with 6 at 300, 16 at 750, 32 at 2000, and 4 at b=0 s mm^{-2}. We eddy-corrected the data via affine registration to the b=0 images, and corrected the data for susceptibility artifacts with acquired field maps.

8.2 Purpose

Impairments that originate in the preterm period have been linked to alteration in tissue microstructure in the brain, as measured by diffusion MRI. The white matter of preterm-born adults shows differences in DTI parameters at all stages of development when compared to term-born controls. We extend diffusion tensor analysis to utilise a multi-shell diffusion acquisition, and analyse the parameters derived by using the NODDI model. We discuss the differences in preterm white matter (WM) in terms of the orientation dispersion (ODI) and intra-cellular volume fraction (v_i).

Both the DTI and NODDI models are applicable in the cortical grey matter (GM), which has received less research attention than white matter. Here, we investigate the effects of prematurity on DW MRI parameters. Because the differences in the preterm brain are prevalent throughout the white matter, we expect there to be some difference also in the grey matter. We also extend this investigation to whether alterations in diffusion parameters are correlated between the white and grey matter.

Because low IQ is a common consequence of preterm birth, it would be of widespread interest to investigate whether tissue structure, as measured by DW MRI, has correlates in intelligence. Here, we use the NODDI model to investigate whether the parameters can predict IQ.

8.2.1 Contribution

This chapter builds upon work that was presented at ISMRM 2016 (Section B.3[7]).

8.3 Methods

8.3.1 Data Analysis

We acquired diffusion MRI as detailed in Section 8.1.1. For this chapter, we analysed 65 (38:27 female:male) nineteen year-old subjects, and 47 term-born controls (29:18 female:male). Three preterm subjects were excluded due to ventriculomegaly. We eddy-corrected the data via affine registration to the b=0 images, and corrected the data for susceptibility artifacts with acquired field maps. We fitted the diffusion tensor model with weighted least squares, and the NODDI model using the NODDI toolbox.

To investigate the spatial patterns of difference between subject and control groups within the white matter, we used Tract-Based Spatial Statistics (TBSS) [140]. This

technique registers diffusion parameter maps into a common space, in which "Skeletonized" tracts are created for white matter. At each voxel in this skeleton, for each subject, TBSS searches perpendicularly from the tract to find a representative parameter value. In this manner, the skeleton has one value per subject at every point. We then use threshold-free cluster enhancement to find clusters of significant difference between preterm and control subjects, implemented in FSL [141]. This is performed on NODDI and DTI parameter maps, and total brain-volume is included as a covariate.

To analyse the cortical grey matter, we used a region-of-interest approach. We segmented the the T_1 images with Geodesic Information Flows [34], using an atlas from *Neuromorphometrics, inc.*. We then rigidly register this segmentation to the diffusion data in order to propagate these labels to the diffusion space. Rigid registration is valid, because of the susceptibility-correction of the DW MRI.

Within these regions of interest, we calculated the mean of the diffusion parameters. To ensure that the segmentation was not highly affected by partial volume in the cortical regions, we excluded voxels with $v_{iso} > 0.1$, and also rejected voxels with $< 90\%$ cortical tissue probability, thus utilising information from NODDI parameters and structural segmentation. To compare the region of interest statistics between preterm and term groups, we used a two-sample t-test for the means. We calculated the effect size of differences using Cohen's d, which is defined as $d = \frac{|\bar{x}_1 - \bar{x}_2|}{s}$, with the $\bar{x}$ being the standard deviation for the pooled data.

8.4 Results

8.4.1 White matter results

In white matter tracts, there are widespread differences between preterm and term subjects (Figure 8.1). FA is higher in term-born subjects in the corpus callosum, and there are increases in MD for the preterm subjects. There were no regions of increased MD in term subjects. For the NODDI parameters, there are several regions of increased ODI for term-born subjects, and decreases in the forceps minor (not pictured). In the forceps minor, this lowered ODI in term-born subjects corresponds to a raised FA. However, the regions of increased ODI in term-born subjects do not tend to occur in regions of FA differences, but tend to co-occur with the MD being lower. The v_i does not show any differences in the tracts between preterm and term subjects, and hence the map is

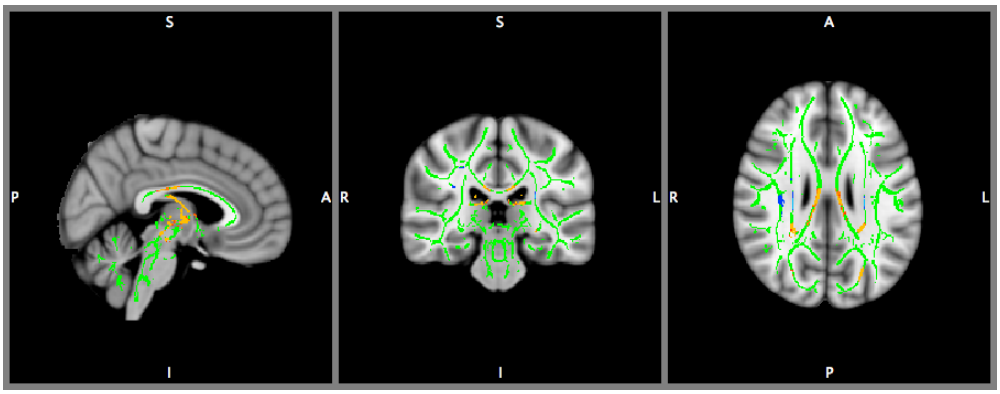

(a) FA

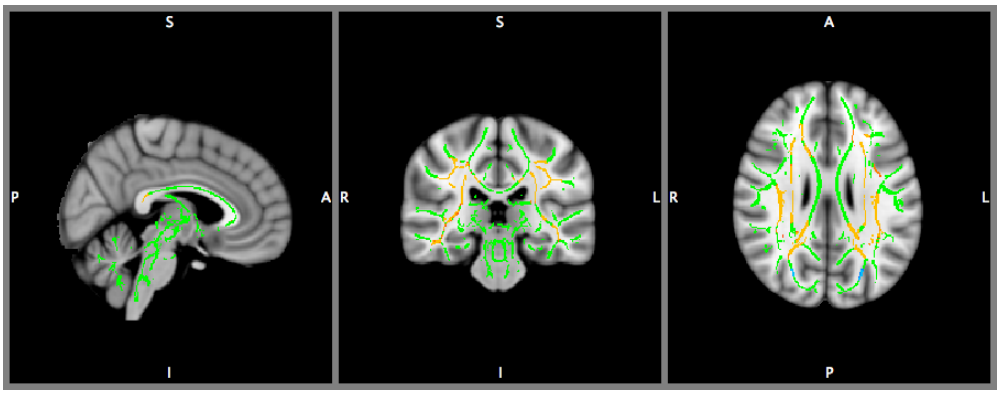

(b) ODI

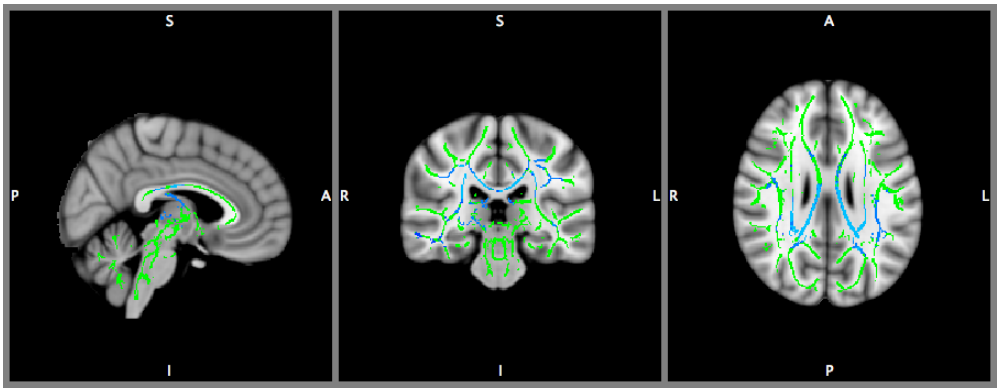

(c) MD

Figure 8.1: Blue: preterm significantly > control. Orange: preterm significantly < control at $p < 0.05/6$ (Bonferroni-corrected). Green: skeleton mask. Regions in the FA maps that are significant (top) appear to be related to those in ODI, with increased FA correlating with decreased ODI. The v_i maps are not shown, as there are no regions of significant differences between groups.

not shown here (it is just the green skeleton).

8.4.2 Cortical grey matter results

The segmentations for the cortical grey matter were conducted successfully, by visual inspection, for both term and preterm subjects (Figure 8.2).

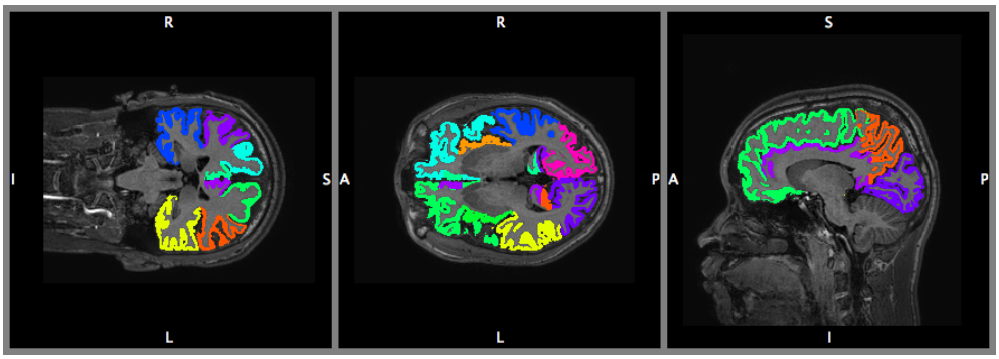

(a) Preterm Male Subject

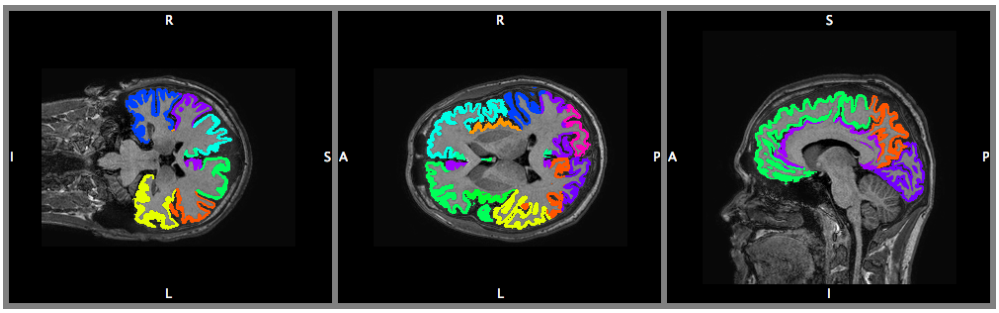

(b) Term Male Subject

Figure 8.2: The cortical segmentations are displayed for a preterm and a term subject.

We display the results for cortical GM in Figure 8.3. Term and preterm subjects showed no significant differences in mean diffusivity, or in the intra-cellular volume fraction. In the FA values, the preterm subjects had higher means in general than term-born peers. In the cingulate cortex and insula, these values were statistically significant to $p < 0.05$ for ODI and FA. We did not observe significant differences in v_i or MD.

We report effect sizes, measured by Cohen's d, in Table 8.1. While v_i and MD have no significant differences, the effect sizes for ODI are larger on average than for FA.

8.4.3 Investigating correlations between WM and GM

In Figures 8.1 and 8.3, we observed that the general trend is that preterm-born adults to have lower FA/higher ODI in the white matter, and the opposite in the cerebral cortex. We decided to investigate whether these trends appeared in tandem within subjects. To do this, we selected two regions that were indicative of this general trend — the body

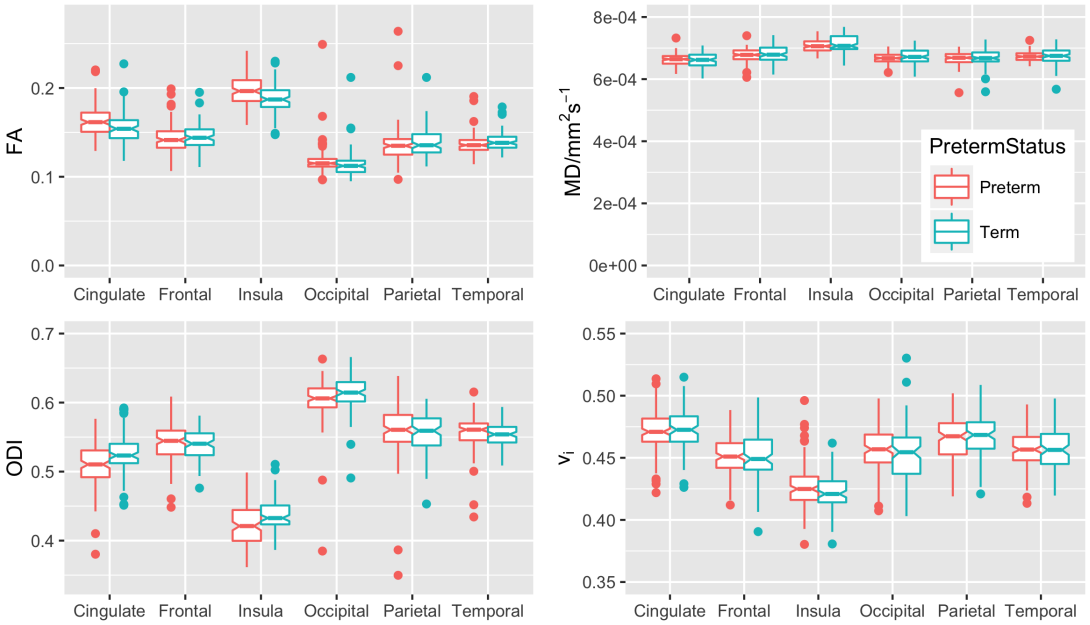

Figure 8.3: We display the data in box plots. The notches correspond to confidence intervals, and neighbouring boxes with non-overlapping confidence intervals are significantly different with $p < 0.05$. In both MD and v_i, there are no significant differences between preterm and term subjects. There are differences for the FA and ODI parameters (see Table 8.1).

Region	Parameter	p-value	Cohen's d
Cingulate	FA	*0.0012*	0.45 (small)
Cingulate	ODI	*2.7e-05*	-0.58 (medium)
Frontal	FA	0.32	-0.13 (negligible)
Frontal	ODI	0.16	0.18 (negligible)
Insula	FA	*0.00012*	0.53 (medium)
Insula	ODI	*6.5e-05*	-0.54 (medium)
Occipital	FA	0.075	0.24 (small)
Occipital	ODI	*0.0058*	-0.37 (small)
Parietal	FA	0.42	-0.11 (negligible)
Parietal	ODI	0.52	0.082 (negligible)
Temporal	FA	0.04	-0.28 (small)
Temporal	ODI	0.14	0.19 (negligible)

Table 8.1: We display here the p-values and Cohen's d for the regions of cortical GM with FA and ODI. The effect sizes are larger in magnitude for the ODI measurement than for FA. * denotes significance at $p \leq 0.05/6$ (Bonferroni-corrected)

.

of the corpus callosum, and the insula. We plotted the means of the parameters for each subject for these regions. If the correlation between parameters is negative, it will indicate that abnormal values in the white matter are correlated with abnormal parameter values within the cortex. If there is no correlation, it suggests that abnormalities within

brain tissue are independent, and that abnormality does not tend to be global within an affected subject.

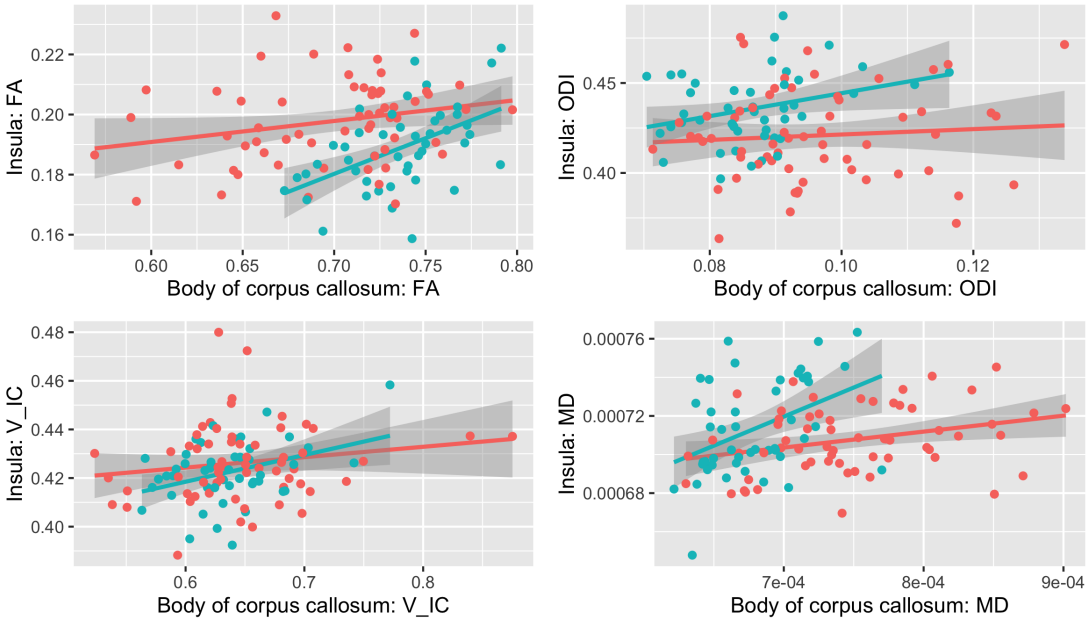

Figure 8.4: We investigate whether there are correlations between the Insula and the Corpus Callosum (body). Red is preterm, and blue is term. No plots have a negative correlation, and the term controls show a positive correlation in FA and MD.

To investigate whether the same subjects were displaying the trends of increased FA/decreased ODI in the white matter, and the inverse in the cortex, we plotted the relationship in Figure 8.4. While preterm and term subjects display clear separation in the expected parameter values, there is no evidence of a negative correlation. In fact, especially for term subjects, the correlation is positive for both ODI and FA, even though the regions of interest are disjoint.

8.4.4 IQ and microstructure parameters

We also investigate whether these regions show correlation with IQ scores. To do this, we take the same two anatomical regions, and plot their mean parameter values against the subject's full-scale IQ. We plot the trend lines separately for the preterm and term groups in Figure 8.5. While there are correlations between the parameters and IQ, these are caused by differences within the population values. There is no evidence that the parameter values predict IQ within groups.

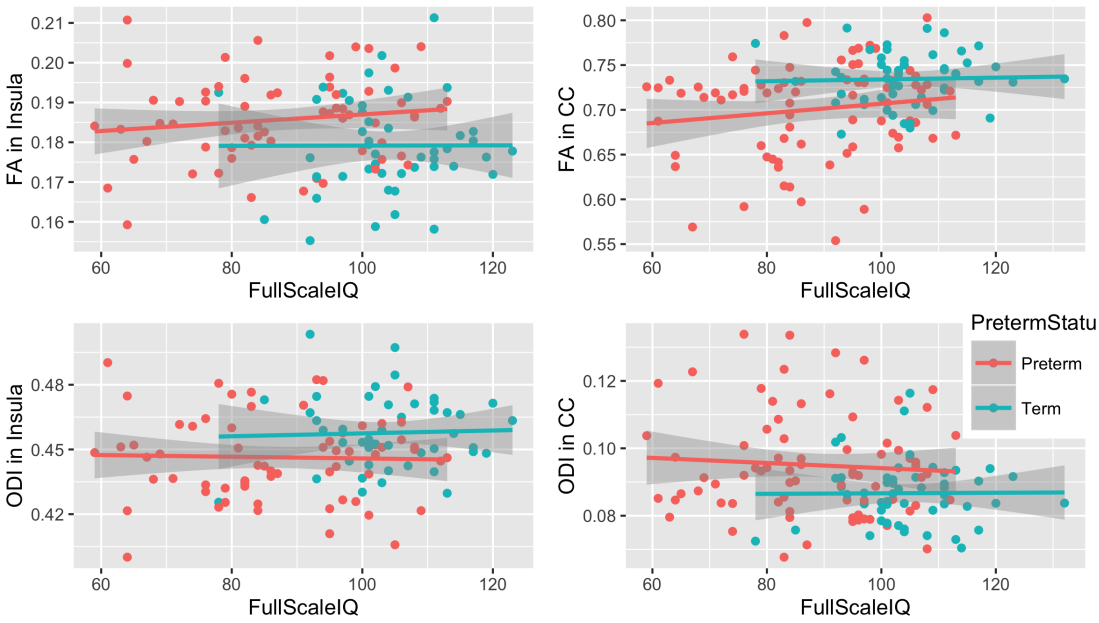

Figure 8.5: We use the parameters from these candidate regions to plot vs IQ. There is no evidence that parameter values correlate with IQ within the groups, even though the parameter values are different between groups.

8.5 Discussion

Microstructure imaging has the potential to observe, in-vivo, indicators of healthy or unhealthy development, with the aim of being able to intervene earlier for those at risk of neurocognitive deficits. This study suggests that DTI parameter changes are due to differences in axonal density and orientation dispersion within the white matter, with the changes being larger for ODI. Previous work has attributed changes in the FA in the corpus callosum to changes in the packing of axons, including their density, rather than fibre structure or axonal injury [58], but we do not find evidence of a change in v_i that would plausibly indicate this. We found that neither v_i nor ODI are significantly different between subjects and controls in the body of the corpus callosum. In the forceps minor, there is significantly higher FA in controls and lower ODI. This is the only region in which we found *decreased* ODI in the term brain, which could relate to more aligned tracts. The interpretation of the FA difference could be that term-born subjects have higher alignment in this region. Increased ODI in several regions in the term subjects is a surprising result, because low ODI is sometimes regarded as a marker of tract integrity. The regions of increased ODI in term-born subjects could come about because there could be more crossing fibres (i.e. a more developed white

matter structure). Also, the decreased MD in some of those regions may have affected the NODDI model's estimates of free water volume fraction, which may in turn alter the white matter parameter estimates.

In the cortex, there are differences between the preterm and term populations. The cingulate cortex and insula are both significantly different between groups, adjusting for multiple comparisons. Both regions have higher FA/lower ODI in the preterm group. It is possible that this difference relates to early cortical development. Because preterm birth occurs before the dendrification of the cortex, but after the radial glial cells are in place, it is possible that the microstructure develops differently, and that these differences persist throughout the lifetime. As opposed to WM regions, high FA and low ODI within the cerebral cortex indicates less "mature" tissue. ODI differences have larger Cohen's d, suggesting that NODDI may yield increased sensitivity to microstructural differences between term-born and preterm infants. However, there is no ground truth of the underlying microstructure available, so it is possible that NODDI is less specific. There may also be some trade-off between specificity and sensitivity, which would require further investigation.

Having shown that there are differences throughout the white matter, and some differences in the cortical grey matter, we investigated whether these differences are co-occurring. For the regions we selected, this would manifest itself as a negative correlation between the FA/ODI in the CC and insula. We do not see this anti-correlation at all, and in fact see a positive correlation in term-born subjects for the FA. Although there is evidence that WM/GM develop in tandem in infancy [108, 142], this does not appear in our data. This shows that it is not a low number of outlier subjects that drive the group differences. It also suggests that alterations in GM/WM do not necessarily occur in tandem.

For the IQ results, there are group differences in both DW MRI parameters and IQ. The higher-IQ subjects have higher values of FA/ODI within the white matter, and lower values in the cortical grey matter. However, when we break this correlation down by preterm/term status, the intra-class correlation is non-existent. In general, with two groups with such different IQ averages, *any* observed differences, in any given parameter, will correlate with IQ. This does not imply that these differences cause the differences in IQ. For a predictive MRI measurement of IQ, we would expect it to also

correlate within groups. Studies have not revealed cellular or microstructural difference in brains that depend on intelligence in the healthy population. Although there are likely to be some differences in tissue microstructure that are in part responsible for decreased intelligence, the lack of evidence thereof in this study indicates that perhaps we are not yet at the resolution or scan quality that would quantify these differences.

In terms of limitations, one confounding factor is that all the subjects were segmented with the same adult-specific technique for the grey matter. Because the preterm subjects have smaller brains, with different morphological characteristics, this may bias the segmentations. In addition to this, we examined relatively large areas of the cortex. It could be the case that heterogeneity in the cortex would mean that more significant differences would be found for smaller regions. For instance, parts of S1 have a tangential, rather than radial, diffusivity [151], and this may have correlates in microstructural parameters.

One interesting future avenue would be to use the partial-volume approach detailed in Chapter 9 to investigate the impact of partial volume on region-of-interest measures, and whether the small size of preterm tracts affected the imaging (beyond what is corrected for by including volume as a covariate).

8.6 Conclusions

The NODDI parameters show that there are significant differences between control and study groups in the white matter microstructure, whereas microstructural differences in cortical grey matter are smaller in magnitude, although present. Micro-structure within regions of interest is not correlated, intra-group, with IQ differences.

Chapter 9

Dealing with partial volume in diffusion MRI

9.1 Introduction

Diffusion MRI is a frequently-used imaging modality that is able to infer properties of local tissue microstructure, down to the scale of microns. For single-compartment models such as the diffusion tensor, the interpretation of the models depends on the voxels having homogeneous tissue. This limitation makes it impossible to directly measure diffusion parameters for small structures such as the fornix, which will have partial volume in every voxel. In this work, we use data from a high-resolution structural scan to infer the tissue composition for each voxel. We model the signal from a voxel as a linear combination of the signals from these components, and thus fit parameters on a per-region basis. Fitting diffusion parameters to all regions simultaneously bolsters the data for small regions, which allows accurate estimation of the diffusion parameters. We use diffusion data from the Human Connectome Project to test the proposed method. The high resolution and quality of the data allow us to measure diffusion parameters in the fornix, before downsampling the data to look like a more typical diffusion acquisition. We compare our parameter estimates for the downsampled scans against these high-resolution standards. After showing that our approach accurately calculates diffusion parameters for small regions, we compare the diffusion parameters in the fornix for adults born extremely preterm and controls. This technique allows accurate estimation of diffusion parameters for structures that are small, compared to a typical diffusion MRI resolution.

Diffusion imaging is a vital tool for probing the microstructure of *in-vivo* tissue. Parametric models of diffusion offer an informative way to summarise the information from many different b-value and gradient directions. The model parameters are often summarised over a region, under the reasonable assumption that tissue within a structure will have similar diffusion properties. This approach works well in large regions, where we can erode a probabilistic segmentation to obtain voxels that are fully within the tissue. But, the diffusion parameters within structures such as the fornix — a narrow white matter structure surrounded by cerebrospinal fluid — may not be measured by this approach [111]. Because of the large scale of diffusion MRI voxels relative to the fornix a majority of, and perhaps all, voxels will contain partial volume. This partial volume affects the measurements of fitted diffusion parameter models, Were we to monitor the diffusion parameters in the fornix, or any other region close to the diffusion resolution, this partial volume would be problematic. We could select a threshold-based segmentation, we may have to adjust the threshold probability over time if the fornix changed size (for example during growth or atrophy), biasing the experiment. If we chose a low percentage threshold throughout, we would be biasing the experiment by including more or less partial volume depending on the structure's size, when we are more interested in its microstructure.

In this chapter, we extend the calculation of a region's parameters to include information from all voxels in the region *during* the model-fitting. Instead of averaging an ensemble of point-wise estimates, we make one point estimate for a region by considering all of the data simultaneously. While there has been work on eliminating the contribution of free water to diffusion parameter estimates [124], the proposed approach directly estimates the diffusion parameters of all tissue types within the image, without relying on *a priori* diffusion models or values. In our approach, we are optimising the model-fit in exactly the manner that our intuition suggests that similar tissues have similar diffusion properties. In this framework, probabilistic segmentations represent linear weights of tissue classes. The signal in each voxel is modelled as the sum of the signal from each tissue class in the region, in proportion to its segmentation weight.

Before implementing the method in the EPICure subject cohort, we first validate the method on *in-vivo* diffusion data from the Human Connectome Project [153]. This dataset is of excellent resolution and quality, and hence we can investigate our ability

to recover parameters for structures that exist below the typical resolution of diffusion data. We can measure diffusion parameters in the fornix directly, in native diffusion space, using hand-drawn regions of interest. By downsampling this data, we simulate a more typical diffusion acquisition, and are able to test whether our approach retrieves the correct parameter values. After validating our approach, we apply it to adults born extremely preterm, comparing the diffusion within the fornix to term-born controls. This patient group has pervasive differences in brain morphology and function, including memory, so this approach has merit in investigating this population.

9.1.1 Contribution

This framework was initially developed and presented as a poster at SPIE Medical Imaging 2016 (Section B.2[2]). The work in this chapter differs in that there is no need of multiple shells of diffusion data, which is an important advantage for using this method in older data. The work here is based more upon its presentation in MICCAI 2016 (Section B.2[1]).

9.2 Methods

9.2.1 Theory

In this work we consider measuring diffusion parameters from below the resolution at which they were obtained. If we imagine a voxel at a higher resolution (for example in the T_1-weighted scan) being downsampled to a lower resolution (the diffusion scans), the proportion of the tissue in a voxel of diffusion space will be reduced. Even in a best case scenario, the probability of there being at least a threshold T% of the tissue within a voxel depends on the position of the tissue relative to the voxel's borders. Our approach eliminates any dependence of measured parameters on the precise voxel boundaries, by using all diffusion information within the region of interest.

During a diffusion acquisition, we vary the b-value and the direction of the diffusion gradients in order to establish how water is able to diffuse in a voxel. We use models to conveniently and informatively summarise the information. Within a given voxel, the water diffusion from several microstructural environments is measured to-

gether. A voxel's signal, S, in the DT model, is given by:

$$\frac{S}{S_0} = e^{-bg^T \mathbf{D} g} \tag{9.1}$$

where S_0 is the diffusion signal with zero diffusion weighting, b are the b-values, g are the gradient directions and $\mathbf{D}$ is the second-rank diffusion tensor.

In our approach, we are trying to obtain $\mathbf{D}$ for each of the k tissue classes. In a given voxel, we model the signal as being represented as a weighted sum of each of the tissue classes that are present:

$$S = S_0 \sum_{j=1}^{k} p_j e^{-bg^T \mathbf{D_j} g} \tag{9.2}$$

$\mathbf{D_j}$ is now the diffusion tensor for a given region. The p_j are non-negative, constrained between 0 and 1, and $\sum_{j=1}^{k} p_j = 1$. This approach considers the components of the $\mathbf{D_j}$ as unknown parameters that are optimised to best fit the data. This is a mixture-model approach, that generates the diffusion parameter estimates for the entire volume simultaneously, instead of per voxel. For the simple case of two tissue classes, this reduces to the signal model in [111].

In order for a single diffusion tensor to represent the diffusion properties in different voxels, we must account for different orientation in different parts of the same tissue. In the conventional approach, we would use the same b-matrix for each voxel in the image. However, we are mainly interested in orientationally-independent measurements, such as the fractional anisotropy (FA). In this work, we redefine the gradient-directions for each voxel, so that the principal directions of all voxels in the image align. The gradient directions at each voxel are calculated by first, performing a tensor-fit to the voxel and establishing V_1 and V_2, the first and second eigenvectors of $\mathbf{D}$. We then calculate the rotation matrix R such that V_1 and V_2 align with [1,0,0] and [0,1,0]. Our vector for the i^{th} voxel then becomes $g_i = Rg$.

After calculating principal diffusion directions in every voxel, and the S_0, with a weighted-least-squares tensor fit, we initialise a $3 \times k$ matrix with identical diffusivities in each of the tissue classes. At each iteration of the optimisation, we calculate the signal for the entire volume simultaneously, before the $3k$ diffusion parameters are

updated. We fit using Matlab 2014b, using non-linear optimisation [38].

9.2.2 Data

To test the proposed approach, we use data from the Human Connectome Project (HCP). The HCP is a flagship effort to map the neural circuitry of the healthy adult human brain. It is a multi-institution project that has scanned hundreds of healthy volunteers with MRI, recording genetic information and other metadata to allow for an unprecedented insight into the wiring of the brain. The data are distributed openly to enable worldwide research.

The MRI data were acquired at high resolution and with a strict protocol, facilitating the creation of one of the biggest datasets of *in-vivo* MRI. The data are available with "minimal pre-processing pipelines", that co-register all the scans into the same space and correct for spatial distortion, among other things. The diffusion protocol takes 55 minutes and uses multiband and other state-of-the-art techniques to produce 270 diffusion-weighted scans per subject, at b-values of 1000, 2000 and 3000 $s.mm^{-2}$. This diffusion data has a resolution of 1.25^3mm^3, with 108 volumes with $b \leq 1200 s.mm^{-2}$. The T_1-weighted MRI is at resolution 0.70^3mm^3, and these data are described further in [153].

For the experiments on adult subjects, we collected MRI data at 19 years of age from 15 adolescents. Eight (4 Male) of these were born extremely preterm (fewer than 26 weeks completed gestation) and seven (3 Male) were recruited as matched controls. The data acquisition is described in Section 8.1.1.

For the segmentations, we manually drew the fornix on a T_1-weighted segmentation and also labelled the surrounding tissue using multi-atlas label propagation and fusion [34] based on the Neuromorphometrics, Inc. labels.

9.2.3 Validating method using HCP data.

We used the high resolution of the HCP data to determine pseudo ground-truth values for diffusion parameters in the column, the crus and the body of the fornix. Each of these regions is hand-drawn onto the subject's T_1-weighted MRI. We downsample the segmentation from categorical labels into a probabilistic diffusion segmentation, where the probabilities represent fractions of the tissue in that diffusion voxel. We varied the downsampling to achieve voxels of isotropic dimension from 1.25mm to 3.5mm. In

order to use HCP data as a model for a more typical diffusion acquisition, we adjust it in the following ways. We added rician noise to the downsampled data, to bring the data to a clinically realistic SNR. We exclude any volumes corresponding to b-values of over 1200, to ignore effects that are not modelled with the DT. We also used a subset of the 108 available diffusion volumes. We tested the performance of our algorithm with varying numbers of these subsets, using between 12 and 60 readings. We compare three approaches for analysing average parameter values:

M1 For each region, we identify voxels where the membership to that region is above the threshold and average their values.

M2 We resample the downsampled DWI to high-resolution HCP space before fitting the DT model and, again, averaging the values for each region. For this, we use 7th-order b-splines, as recommended in [54].

M3 (proposed): We calculate parameter values for each region, explicitly accounting for partial volume. The p are given by downsampling labels from the T_1-weighted segmentation into diffusion space.

9.2.4 Results

In Figure 9.1 we test approach M1. As the threshold changes, so do the results for the classical approach. With a 90% threshold, at a resolution of 2mm isotropic, all fornix tissue has partial volume, and so even at this good resolution, we would be unable to proceed with this threshold. However, as we decrease the threshold, increasing the resolution results in decreasing FA, as CSF partial volume contaminates the estimates. For the body of the fornix, the measured FA decreases by up to 13% by changing the thresholding, and when downsampled to 2.5mm, the measured FA is up to 25% lower than the pseudo-gold-standard.

In approach M2, we use the segmentation at the HCP resolution. After downsampling the data and adding noise, we interpolate the diffusion data back to the HCP resolution in order to fit the diffusion tensor and average the results over the ROI. These results are displayed in Figure 9.2. The measured diffusion parameters diverge from their 'true' values as we interpolate data of lower resolution. With no downsampling, the values of nearby white matter, the column and the crus of the fornix are similar.

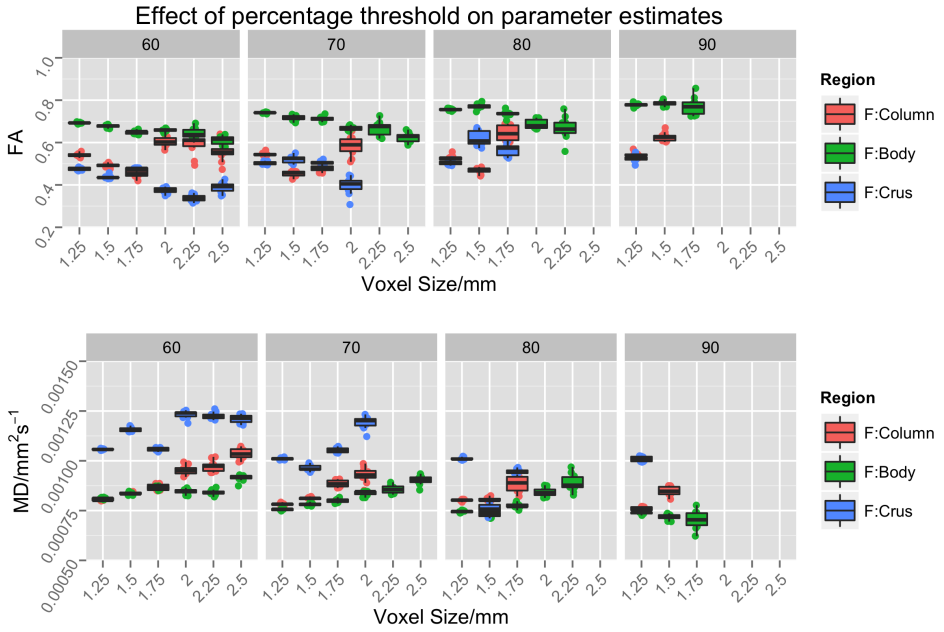

Figure 9.1: In this graph, we see the effect of downsampling the resolution (x axis) on parameter estimates from a threshold-based approach. As the voxel dimension increases, the parameter estimation is less reliable and at some point stops, as there are no more supra-threshold voxels to sample. The choice of the threshold will influence the measured parameter value.

However, as the downsampling increases, the FA estimates decrease due to the partial volume. This means that parameter values that should be similar are diverging because of local surroundings.

With the proposed method, the FA in the column and crus of the fornix is constant (Figure 9.2). The body of the fornix has an increasing FA. The mean diffusivities are more constant in the proposed method than with the classical. Downsampling the data affects the accuracy of all the measured parameters using the classical approach.

9.3 Comparison of preterm-born and term-born young adults.

We compare fornix DTI parameters as calculated with M2 (upsampling DWI to T_1-space and fitting the tensor) and M3 (proposed) in Figure 9.3. The MD in the fornix is higher in general for the classical approach compared to ours. In the classical approach, there is a significant difference in the MD with the subject group having higher MD ($p \leq 0.0005$). Both approaches measure higher mean FA in the subject group, but neither

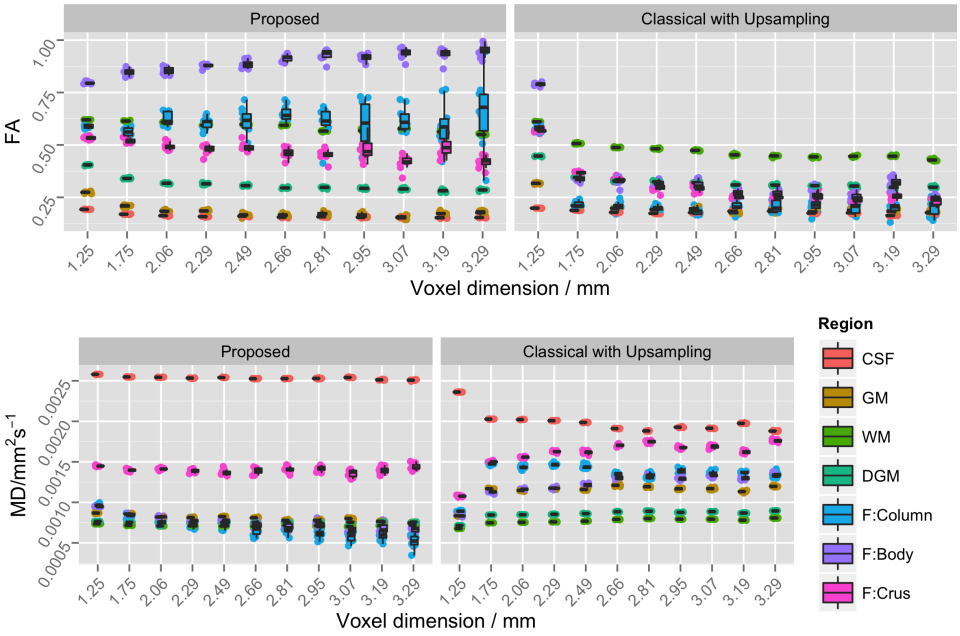

Figure 9.2: In our method (left), the diffusion parameters in the fornix are fairly consistent with downsampling. While the results for larger regions match the classical approach, we improve for the fornix. We present the results for a thresholding approach *with* prior upsampling of the data (right). The results here, for diffusion parameters of the fornix, show a divergence of the diffusion parameter readings depending on their surrounding tissue. The scale factor is the factor by which we've downsampled the volume. In these experiments, we used 12 diffusion readings, 2 of which were reference volumes.

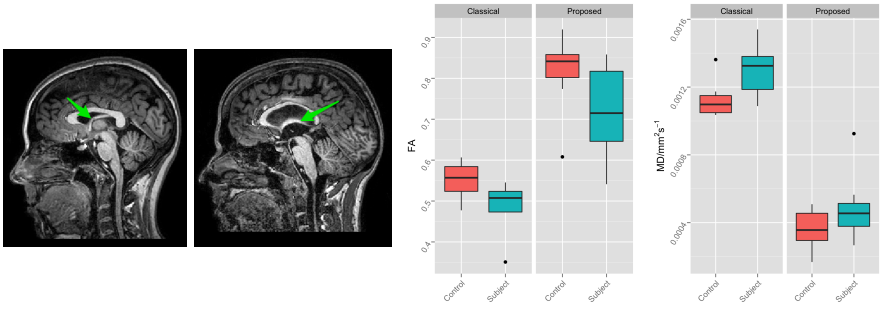

(a) Control (b) Subject (c)

Figure 9.3: In a-b the fornix is highlighted with an arrow in a control and a preterm subject. The preterm-born subject has noticeable abnormalities in the corpus callosum, and enlarged ventricles. In c, we display the measured parameters using our proposed approach vs the classical.

is significant when accounting for multiple comparisons.

9.4 Discussion

Our method achieves consistent and accurate parameter estimates for small regions in partial volume. Although interpolating data reveals some details that are hidden at low resolution [54], interpolation of downsampled HCP data biased the results of the measured diffusion parameters in the fornix. FA values in all parts of the fornix tended to be underestimated and diverged from FA estimates in other white matter regions.This means that the local surroundings of the fornix biased the diffusion results, which our method was able to address.

There is promise in using this approach in subject groups, such as the preterm-born young adults in this study. Our approach reduces the impact of partial volume on measuring the properties of the fornix. The lower MD we measured for subjects and controls is in accord with this. The higher FA values suggest that we are able to measure the diffusion in the highly-anisotropic region of the fornix with less impact from the surrounding cerebrospinal fluid. While this is not a conclusive result, due to the small number of subjects, it is a promising sign. There is some evidence from both methods that preterm-born adults have lower FA in the fornix than controls, which is congruent with the general consequences of being born prematurely (for example, in Chapter 8).

While there are a range of biophysical compartment models in use in diffusion imaging, most of these rely on multi-shell data to fit compartments in each voxel, or else have to heavily restrict the available parameters. We circumvent this by fitting on a per-tissue basis, by using information from a structural segmentation. Provided the segmentation maps well to diffusion space, this may mean that more advanced diffusion models can be fitted, as there is more data to fit to.

Another way to calculate diffusion parameters would be investigating super-resolution techniques. Alexander et al [5] showed that a machine-learning approach could be used to effectively super-resolve the diffusion data from DTI parameters. For this particular method, it is unclear how generalisable the approach is without high-resolution training data from each scanner in use. Our method requires only the original diffusion acquisitions, so is widely useable. We achieved our results with only 12 diffusion readings, which renders the method suitable to many past datasets.

We show that it is feasible and possible to estimate diffusion parameters for regions

that are small on the scale of diffusion MRI. In large, contiguous regions we achieved the same results as for the classical approach, of thresholding and averaging. We used the fornix as a region of interest to show that our approach was able to recover diffusion parameter estimates consistently, when the classical approach failed. Although results were good in the fornix, the model would have to be extended to cope with geometry such as crossing fibres.

The presented approach achieves close-to gold-standard results with minimal processing time and requirements for the diffusion acquisition. This is because we aggregate data from all voxels in which a particular region is present, even in part. This type of approach fits conceptually with more sophisticated, multi-compartment models — we plan to extend our investigation to using multi-modal segmentations to determine volume fractions for certain tissue types. In this work, we proposed a method to extract diffusion tensor parameters from tissue that has partial volume. We have validated the method using high-quality data from the HCP, and applied it in a new cohort of clinical interest.

Chapter 10

Conclusions & future investigations

10.1 Summary and conclusions

This thesis presents a range of investigations that use compartment models of diffusion MRI within the preterm brain. The versatility of this approach allows for a range of microstructural environments to be examined, using a common framework. We have developed and tested novel methodology to explore the effects of prematurity on the brain, and to quantify brain maturation.

From chapters 3 to 6, we examined the Sparks cohort. This cohort used a two-shell diffusion MRI acquisition, as well as T_2 relaxometry and structural scans, to study the longitudinal development of brain tissue for extremely-preterm infants. Within the white matter, we examined NODDI parameters on a longitudinal basis (Chapter 3). In white matter tracts, the increasing FA in development corresponds to both increasing intra-cellular volume fraction, and decreasing orientation dispersion. These rates depend on the white matter region. In Chapter 8 we investigated the white matter of adults born extremely preterm, whose white matter tissue has different DTI and NODDI parameters to their term-born counterparts. The lower FA in DTI mainly reflects lower values of orientation disperson in the NODDI model. The effect sizes of NODDI parameters in the white matter are smaller than for DTI parameters.

In Chapter 4, we investigated tissue parameters in the cortical and thalamic grey matter. We demonstrated that within the thalamus, the changes in FA were correlated with the changing v_i, with almost no change in ODI. In the cortex, the FA values decrease in the preterm period. In contrast to the thalamus, this change co-occurs with the ODI increasing, and a small change in v_i. We interpret the NODDI parameters as in-

dicating that microstructural change within the cortex is mainly geometric, which may relate to the cellular process of dendrification. The changes in the thalamus relate more closely to neurite density and packing. These findings highlight the potential of using biophysical models of diffusion MRI.

The thalamus is implicated in several disorders associated with prematurity. In Chapter 5, we present a method to register the thalamus to itself during development in a biologically-plausible manner, for two time-points within-subject. We used diffusion tractography to segment the thalamus, depending on its cortical connections, and used these sub-thalamic regions to drive the mapping. We created maps of parameter-changes within the registered thalamus over the first 10 weeks of neonatal life, which demonstrated that changes were predominantly seen in the v_i, concurrently with the thalamus myelinating. Although DW MRI is not directly sensitive to myelin, we investigated whether the change in v_i is caused by myelin in Chapter 6. Myelin contributes less than a third of the observed parameter change, and we propose that the remainder is caused principally by increasing intra-axonal space. We demonstrate that the g-ratio is measurable *in-vivo* by combining imaging modalities.

Using scalar diffusion parameters can be augmented by using the directional information from DW MRI. The decrease in fractional anisotropy in the infant cortex also involves the geometrical transition away from diffusion that is entirely radial to the surface of the cortex. We investigated the cortical radiality index in Chapter 7. By using the DIAMOND model to represent the diffusion, in tandem with cortical surface meshes, we calculated the radiality index and investigated its longitudinal trajectory. We showed that the rate of change during maturation depends on the cortical lobe. This is the first time that radiality has been measured longitudinally in a human population, and shows how structural and diffusion MRI can be combined to generate parameters that integrate this complementary information. Also, we showed that the DIAMOND model had greater sensitivity to these changes than DTI.

In Chapter 9, we developed a method to accurately estimate diffusion parameter values in regions of partial volume. This approach was tested on HCP data, and applied it to the EPICure cohort. This approach used a compartment model, where each tissue class was represented by one instance of a diffusion tensor, oriented depending on the underlying tissue. By combining information from several voxels, each with

some non-zero proportion of the tissue in question, we are able to estimate underlying tissue parameters accurately for small regions of interest, across varying levels of partial volume.

10.2 Future research directions

10.2.1 Further investigations in the developing cortex

Because the microstructural development in the cortex is so pronounced in the perinatal period, it is important to develop methods to quantify the changes within the cortex. The work we have presented on measuring cortical radiality could be extended in several ways. With scans at better resolutions, or by investigating higher b-values, it would be possible to fit more complex models of microstructure. Our collaborators on this work have submitted a grant to perform high-resolution DW MRI on a small number of infants in the NICU at Boston Children's Hospital. By using good image reconstruction, and an optimised acquisition protocol, they hope to determine the best signal model for the cortex in particular, and detect changes with more specificity to the underlying structure.

10.2.2 Partial volume diffusion parameter estimation

In Chapter 9, we described the work on estimating diffusion parameters in regions of partial volume. The work on this problem has used a framework in which diffusion within a voxel is represented as a linear combination of signals, coming from separate tissue compartments. The signal within each voxel is a sum of the signals from each tissue compartment within the voxel (here "tissue" means segmentation class). This technique is agnostic towards the chosen models. Work presented in SPIE Medical Imaging used the NODDI model to represent the signal [55]. For the presentation at MICCAI 2016 [56], we investigated using the diffusion tensor model. To validate this approach further, it would be useful to compare to the results of a fluid-attenuated diffusion acquisition in a region neighbouring the CSF.

Some reviewers highlighted the model's inability to model crossing-fibre regions, which are prevalent in the brain. Although these issues do not affect the measurements for the fornix, it would be possible to extend the framework to cope with multiple diffusion directions. We could fit multiple-tensors within each voxel, saving the principal

directions, and use these to create the forward model of diffusion. This would yield parameters for each compartment of the multi-tensor. However, there may be difficulties in separating contributions from fibres that have similar directions. Also, it may be important to spatially regularise the fitting of the multi-tensors, because spatial discontinuities may otherwise invalidate the assumptions. The effects of this regularisation would need careful assessment in terms of their impact on fitted parameters.

10.2.3 The impact of size on infant brain MRI

Several papers have looked at the progression of DTI metrics in brains of neonates and infants during the early months of life [123, 53], finding increases in FA and decreases in MD during maturation in the white matter. Partridge noted the effect of improving the DTI resolution, stating:

> *Through these reductions in partial volume averaging, it is predictable that our tract-specific D_{av} values should be lower and our anisotropy measurements higher than prior studies, by minimizing contributions from surrounding less mature and less compact white matter, as well as CSF, both of which have higher D_{av} and lower anisotropy values. Partial volume effects may additionally reduce anisotropy values by including adjacent pathways with different fiber orientations than the tract of interest.* [123]

where D_{av} is the mean diffusivity, MD. This observation remains relevant. If white matter diffusion properties vary in different anatomical regions (as we know they do), then the resolution of the MRI, relative to the size of the structure, matters. This effect is magnified in the developing brain: longitudinal measurements will have the same spatial resolution, but differing anatomical size. How does this affect the measurements of diffusion parameters?

One existing approach is to include regional volumes as confounding variables in a regression framework. In [11], the authors used regional volumes from regions other than the examined region of interest, in order to act as a proxy for the size. For instance, they measured FA in the corpus callosum, and included the volume of the thalamus as a co-variate. One limitation of this approach is that partial volume may affect regions differently, depending on their size or shape.

While partial volume is a known confound in diffusion MRI studies [157], it has not been fully taken into account for studies on infant brain development. We hypothesise that: **Some proportion of measured change in diffusion properties observed in infancy can be attributed to increases in physical size, with *no associated underlying change in microstructure***. To investigate this, we would create an MRI phantom, using an MR simulator [50, 51]. By contracting or expanding the phantom, we would simulate MRI acquisition from brains of varying size, by construction. The microstructure in the simulation would be identical at all length scales. We would measure the diffusion parameters obtained by applying standard segmentation and DT fitting, and test whether estimates depend on physical size of the phantom. If there is a correlation between regional size and measured diffusion parameters, it would then be possible to use this to estimate how much of the parameter change in infants is due to bulk size. This experiment would explain how macrostructural growth impacts the measurements of microstructure.

We have successfully performed some preliminary work on this. We computed phantoms, and found a relationship between the brain size and measured microstructure. For a simulation with the *same FA* at different sizes of tract, there was a significant, monotonic relationship between FA and size. Although more work is needed, it does appear that some of the parameter change in brain development can be attributed to bulk growth of the brain, rather than to the changing microstructure.

10.2.4 Closing thoughts

In this thesis, we have presented a variety of work using compartment models of diffusion MRI. We have defined normative NODDI parameter values within the preterm population, investigated the development of cortical radiality, and extended the framework of compartment modelling to handle partial-volume situations. We have also combined diffusion MRI with quantitative T_2 in order to map the g-ratio *in-vivo*.

Our findings include that:

- Our proposed partial volume correction technique fuses structural and diffusion measurements to better estimate region-of-interest parameters.
- The NODDI model can be applied in the grey and white matter of the preterm brain. While it does not offer increased sensitivity in white matter, its parame-

ters allow a more biologically-motivated interprestation of diffusion data in the thalamic and cortical grey matter.

- The NODDI model can be used in tandem with quantitative T_2 images in order to calculate the g-ratio in vivo. We used the myelin measurements to put an upper bound on the effect of myelin on v_i in the thalamus; it accounts for less than a third of the parameter change. The ability to correctly attribute changing diffusion MRI parameters to the underlying microstructure is critical to advancing the field.

- The 'radiality index' can be computed longitudinally in the preterm infant, with regional changes that do not simply replicate other parameters. The DIAMOND model is more sensitive to maturation than DTI for this purpose.

While diffusion MRI has been widely utilised, it is still short of being able to provide patient-specific prognosis. However, there is room for optimism. In combining DW MRI with other modalities and measurements, microstructural analysis will improve. The Human Connectome Project exemplifies a trend towards acquiring more and better data, which may come to encompass preterm subjects. With careful analysis and advances in scanning methodology, there will be advances in characterisation of preterm phenotypes at all ages. This will, in turn, enable the development and implementation of treatments, for what remains a significant public health problem.

Appendix A

Glossary of terms

Term	Definition
ADC	Apparent Diffusion Coefficient
AIC	Akaike Information Criterion
BIC	Bayesian Information Criterion
CSF	Cerebrospinal Fluid
DIAMOND	DIstribution of Anisotropic MicrOstructural eNvironments in Diffusion-compartment imaging
DKI	Diffusion kurtosis imaging
DTI	Diffusion tensor imaging
DW MRI	Diffusion-Weighted MRI
EGA	Estimated Gestational Age
FA	Fractional Anisotropy
FWE	Free Water Elimination
GM	Grey matter
HCP	Human Connectome Project
MD	Mean Diffusivity
MRI	Magnetic resonance imaging
NICU	Neonatal Intensive Care Unit
NMI	Normalised Mutual Information
NODDI	Neurite Orientation Dispersion and Density Imaging
PV	Partial Volume
ROI	Region of Interest
SMT	Spherical Mean Technique
v_i	NODDI's Intra-Neurite Volume Fraction
WM	White matter

Table A.1: This is a glossary of terms for common abbreviations used within the thesis.

Appendix B

Published work

B.1 Journal publications

1. **Z. Eaton-Rosen**, B. Scherrer, A. Melbourne, S. Ourselin, J.J. Neil & S.K. Warfield, "Investigating the maturation of microstructure and radial orientation in the preterm human cortex with diffusion MRI", *NeuroImage*, 2017, 162, pp65-72.

2. A. Melbourne, **Z. Eaton-Rosen**, E. Orasanu, D. Price, A. Bainbridge, M.J. Cardoso, G.S. Kendall, N.J. Robertson, N. Marlow & S. Ourselin. "Longitudinal development in the preterm thalamus and posterior white matter; MRI correlations between Diffusion Weighted Imaging and T_2 relaxometry". *Human Brain Mapping*, 2016, 7, pp2479-2492.

3. **Z. Eaton-Rosen**, A. Melbourne, E. Orasanu, M.J. Cardoso, A. Bainbridge, G.S. Kendall, N.J. Robertson, N. Marlow, and S. Ourselin. "Longitudinal measurement of the developing grey matter in preterm subjects using multi-modal MRI". *Neuroimage*, 2015, 111, pp580-589.

B.2 Conference proceedings

1. **Z. Eaton-Rosen**, A. Melbourne, M.J. Cardoso, A. Bainbridge, G.S. Kendall, N.J. Robertson, N. Marlow & S. Ourselin.. "Beyond the Resolution Limit: Diffusion Parameter Estimation in Partial Volume". *In MICCAI. Lecture Notes in Computer Science*, 2016, pp605-612.

2. **Z. Eaton-Rosen**, M.J. Cardoso, A. Melbourne,A. Bainbridge, G.S. Kendall, N.J.

Robertson, N. Marlow & S. Ourselin.. "Fitting parametric models of diffusion MRI in regions of partial volume". *SPIE Medical Imaging*, 2016.

3. E. Orasanu, A. Melbourne, M. Lorenzi, M. Modat, H. Lombaert, **Z. Eaton-Rosen**, G.S. Kendall, N.J. Robertson, N. Marlow and S. Ourselin.. "Tensor Spectral Matching of Diffusion Weighted Images". *Workshop on Spectral Analysis in Medical Imaging (SAMI)*, MICCAI, 2015.

4. A. Melbourne, **Z. Eaton-Rosen**, D. Owen, M.J. Cardoso, J. Beckmann, D. Atkinson, N. Marlow & S. Ourselin. "Measuring cortical neurite-dispersion and perfusion in preterm-born adolescents using multi-modal MRI". *In MICCAI. Lecture Notes in Computer Science*, 2015, pp 72-79.

5. A. Melbourne, **Z. Eaton-Rosen**, E. De Vita, A. Bainbridge, M.J. Cardoso, D. Price, E. Cady, G.S. Kendall, N.J. Robertson, N. Marlow & S. Ourselin.. "Multi-modal measurement of the myelin-to-axon diameter *g*-ratio in preterm-born neonates and adult controls". *In MICCAI. Lecture Notes in Computer Science*, 2014, pp268-275.

6. **Z. Eaton-Rosen**, A. Melbourne, E. Orasanu, M. Modat, A. Bainbridge, M. J. Cardoso, G. S. Kendall, N.J. Robertson, N. Marlow, and S. Ourselin. "Longitudinal measurement of the developing thalamus in the very-preterm brain using multi-modal MRI". *In MICCAI. Lecture Notes in Computer Science*, 2014, pp276-283.

7. Melbourne, A., **Z. Eaton-Rosen**, A. Bainbridge, G.S. Kendall, M.J. Cardoso, N.J. Robertson, N. Marlow, and S. Ourselin.. "Measurement of myelin in the preterm brain: multi-compartment diffusion imaging and multi-component T_2 relaxometry". *In MICCAI. Lecture Notes in Computer Science*, 2013, pp 336-344.

B.3 Conference abstracts

1. A. Melbourne, E. Orasanu, **Z. Eaton-Rosen**, M.J. Cardoso, J. Beckmann, L. Smith, D. Atkinson, N. Marlow, and S. Ourselin.. "Analysis of brain volume in a 19 year-old extremely- preterm born cohort". *ISMRM*, 2016.

2. A. Melbourne, **Z. Eaton-Rosen**, E. Orasanu, J. Beckmann, A. Saborowska, D. Atkinson, , N. Marlow, and S. Ourselin.. "Perfusion and diffusion in the extremely preterm young adult thalamus". *ISMRM*, 2016.

3. A. Melbourne, E. Orasanu, **Z. Eaton-Rosen**, J. Beckmann, A. Saborowska, D. Atkinson, , N. Marlow, and S. Ourselin.. "Characterizing microstructure and shape of the extremely preterm 19 year-old corpus callosum". *ISMRM*, 2016.

4. E. Orasanu, Melbourne, A., **Z. Eaton-Rosen**, D. Atkinson, , J. Lawan, J. Beckmann, N. Marlow, and S. Ourselin.. "Local shape analysis of the thalamus in extremely preterm born young adults". *ISMRM*, 2016.

5. E. Orasanu, Melbourne, A., **Z. Eaton-Rosen**, D. Atkinson, , A. Saborowska, J. Beckmann, N. Marlow, and S. Ourselin.. "Cortical folding patterns in extremely preterm born young adults". *ISMRM*, 2016.

6. E. Orasanu, Melbourne, A., M. Modat, M. Lorenzi, H. Lombaert, **Z. Eaton-Rosen**, N.J. Robertson, G.S. Kendall, N. Marlow, and S. Ourselin.. "Mapping longitudinal white matter changes in extremely preterm born infants". *ISMRM*, 2016.

7. **Z. Eaton-Rosen**, Melbourne, A., E. Orasanu, J. Beckmann, Nicola Stevens, D. Atkinson, , N. Marlow and S. Ourselin.. "White matter alterations in young adults born extremely preterm: a microstructural point of view". *ISMRM*, 2016.

8. A. Melbourne, **Z. Eaton-Rosen**, A. Bainbridge, G. S. Kendall, N. Robertson, N. Marlow, S. Ourselin. "Measurement of the myelin-to-axon diameter g-ratio in very-preterm infants using multi-modal MRI". *ISMRM*, 2014.

9. A. Melbourne, **Z. Eaton-Rosen**, D. Price, E. Cady, A. Bainbridge, G. S. Kendall, N. Robertson, N. Marlow, S. Ourselin. "Longitudinal imaging of the preterm brain: white matter multi-component T_2 relaxometry and MR spectroscopy". *ISMRM*, 2014.

10. **Z. Eaton-Rosen**, A. Melbourne, E. Orasanu, A. Bainbridge, G.S. Kendall, N.J. Robertson, N. Marlow and S. Ourselin. "Cortical maturation in the preterm pe-

riod revealed using a multi-component diffusion-weighted MR model". *ISMRM*, 2014.

11. **Z. Eaton-Rosen**, A. Melbourne, E. Orasanu, A. Bainbridge, G.S. Kendall, N.J. Robertson, N. Marlow and S. Ourselin. "Measurement of white matter maturation in the preterm brain using NODDI". *ISMRM*, 2014.

Appendix C

HBM Manuscript

C.1 Contribution

In this Appendix, we include work published in Human Brain Mapping, Vol. 7, 2016, pp2479-2492. The title is: **Longitudinal Development in the Preterm Thalamus and Posterior White Matter: MRI Correlations Between Diffusion Weighted Imaging and T_2 Relaxometry**.

Parts of this work are used in Chapter 6, but there is substantially more work here on magnetic resonance spectroscopy, as well as more detail on the precise protocols used. I conducted this work with Dr Andrew Melbourne. We were jointly responsible for deriving the formula for the *g*-ratio. He wrote the manuscript; I conducted the diffusion pre-processing, helped with the interpretation, and assisted in editing the work.

C.2 Abstract

Infants born prematurely are at increased risk of adverse neurodevelopmental outcome. The measurement of white matter tissue composition and structure can help predict functional performance. Specifically, measurements of myelination and indicators of myelination status in the preterm brain could be predictive of later neurological outcome. Quantitative imaging of myelin could thus serve to develop biomarkers for prognosis or therapeutic intervention; however, accurate estimation of myelin content is difficult. This work combines diffusion MRI and multi-component T_2 relaxation measurements in a group of 37 infants born very preterm and scanned between 27 and 58 weeks equivalent gestational age. Seven infants have longitudinal data at two time

points that we analyze in detail. Our aim is to show that measurement of the myelin water fraction is achievable using widely available pulse sequences and state-of-the-art algorithmic modeling of the MR imaging procedure and that a multi-component fitting routine to multi-shell diffusion weighted data can show differences in neurite density and local spatial arrangement in grey and white matter. Inference on the myelin water fraction allows us to demonstrate that the change in diffusion properties of the preterm *thalamus* is not solely due to myelination (that increase in myelin content accounts for about a third of the observed changes) whilst the decrease in the *posterior* white matter T_2 has no significant component that is due to myelin water content. This work applies multi-modal advanced quantitative neuroimaging to investigate changing tissue properties in the longitudinal setting.

C.3 Introduction

In the developing white matter of the preterm brain, processes leading to myelination progress in an established spatial pattern, ascending into the corticospinal tracts from as early as 30 weeks gestation and progressing from this region anterior and posterior over the first few months of life [29]. Infants born very preterm are at increased risk of adverse neurodevelopmental outcome [39] and this is believed to be related to delay or disruption to normal developmental processes during this crucial time. The reproducibility of the myelin developmental trajectory means that if myelin content can be measured, myelin location and quantity might be predictive of delays in the subsequent myelination process, and thus of neurological developmental delay in infancy. A number of Magnetic Resonance (MR) based techniques have been used to infer myelin content including magnetisation transfer [147] and T_2 relaxometry [127]. Diffusion Weighted MRI (DWI) is sensitive to local structure, but the short T_2 of the myelin signal component means that DWI is generally non-specific to myelin, although its presence will have some influence on parameters derived from a diffusion model. As a result any inference on myelin content using DWI alone is inherently speculative. In this work we estimate the myelin water signal from multi-echo multi-component T_2 relaxometry [127] and combine this with the intra-axonal volume signal measured by the NODDI model; this imaging combination can be used to define a joint *in-vivo* imaging biomarker that makes use of the structural sensitivity, but myelin inspecificity, of DWI

with the high myelin specificity, but structural insensitivity of multi-echo T_2 relaxometry. Previous work has combined similar measurements in both quantitative [106] and non-quantitative [147] frameworks to obtain the *internal axon diameter* to *myelinated axon diameter* g-ratio [37]. Since this measurement has the potential to map the electrical properties of axons, it may be correlated with specific functional measurements. Magnetic Resonance Spectroscopy (MRS) studies have demonstrated changes in white matter metabolism with brain development including an increase in N-Acetylaspartate (NAA) with progressing brain maturity, and a decrease in choline (Cho). The amino acid NAA is synthesised primarily in neuronal (including axonal) mitochondria and is therefore likely to have a relationship to cell energy turnover [83, 114]. In normal brain development, Cho related species incorporate into macromolecules during myelination and become invisible to MRS, thus enhancing the observed NAA/Cho ratio. Results of neonatal spectroscopy have been linked to function and motor outcome at one year of age [81].

During the period between 30-40 weeks gestation, short range associative connections increase in number and the white matter cellular composition is altered in advance of subsequent myelination. On magnetic resonance imaging (MRI), the absence of myelin is a major contributor to the inverted contrast, relative to the adult brain, seen on T_1 and T_2 weighted images and thus there is interest in using MR measurement of myelin as a biomarker of later neurological outcome. Some developmental changes can be observed on DW MRI; for instance in grey matter the increasing cortical connectivity between 30 and 40 weeks gestational age reduces the observed diffusion anisotropy in a characteristic pattern [101], but this imaging technique is mostly insensitive to myelination since the T_2 of proton spins bound into associated proteins is very short ($< 60ms$). As discussed in [72] changes to the diffusion tensor may be observed before the histological presence of myelin and so it is difficult to make statements about myelination without specific quantification. Furthermore, in the adult brain, only moderate correlations between diffusion parameters and multi-component T_2 were found by [96]. Single component relaxometry is thought to be a non-specific indicator of myelin and myelination [66, 69] but as demonstrated by [90, 91], a myelin water fraction v_{mwf} derived from multi-component T_2 relaxometry has a specific correlation with the results of histological staining. Nonetheless, changes to the cellular content of white matter

have been used to infer the presence of myelin: during the preterm period; at term equivalent age and to follow myelination through infancy [123, 66, 116, 86].

Recent studies have begun to investigate more quantitative measurements of neonatal brain development. Independently, [31] and [122] investigated how the derived structural connectivity from diffusion weighted imaging differs with degree of prematurity and results of this type have begun to be linked to functional outcome at later ages [13]. Recent work has moved away from the diffusion tensor model and begun to develop quantitative imaging parameters using biologically-motivated model-based diffusion-weighted imaging and this has been applied to both white [87] and grey matter [57] properties of preterm brain tissue. Results of combinations of imaging modalities have been linked to demonstrate the relationship between cortical folding and diffusion MRI [108] or to propose new imaging biomarkers [106].

In this work we investigate how properties derived form both diffusion imaging and multi-component T_2 relaxometry change in the developing thalami-cortical system between 30-40 weeks equivalent gestational age (EGA) as assessed cross sectionally on a cohort of 37 infants which includes longitudinal data for seven infants. We combine results from Diffusion weighted imaging, T_2 relaxometry and proton spectroscopy to study longitudinal changes in the same infants at two time-points. Here, we attempt to combine only quantitative measurements such as the intra-axonal and myelin-water volumes in contrast to surrogate, measurements such as the fractional anisotropy or the single-component T_2.

We show how T_2 values change in the thalamus, the adjacent white matter and in the posterior white matter. In addition we show that the overall change in T_2 can be attributed to an increase in myelination in the thalamus, but in the white matter this is not due to myelin but due to a reduction in free water content and increase in tissue volume. From DWI we show that the intra-axonal volume fraction increases in the thalamus, but that this change can be explained by a combination of both myelin volume increase and axonal volume increase. We also present multi-parametric results within common white-matter regions of interest.

C.4 Data

Imaging data were acquired for 42 preterm infants from the Sparks cohort (Section 3.2). Infants were excluded if they had abnormal cerebral ultrasound (2 infants), or if either the diffusion acquisition or the relaxometry acquisition was unusable due to patient movement (3 infants). Infant MRI was assessed using a white matter scoring system [161]. No infants in this study were graded as having moderate or severe injury. The remaining 37 (10/27 M/F) preterm infants comprised 15 infants with data acquired at approximately 31 and 42 weeks EGA, four infants with data acquired at approximately 30 weeks EGA only and 18 infants with data acquired at approximately 40 weeks EGA only. Seven infants had usable longitudinal data (5/2 M/F). Imaging was carried out on a 3T Phillips Achieva. Cohort information is summarized in Table C.1.

Male/Female	10/27
Gestational age at birth	26.27 ± 2.10wks
EGA at early scan	31.02 ± 1.91wks
EGA at late scan	41.66 ± 4.28wks
Birthweight	844 ± 141g
Antenatal steroids	94%
Postnatal steroids	6%
Sepsis	13%
CLD/BPD (O_2 at 36wks)	76%
Medically treated for NEC	33%

Table C.1: Selected demographic information for preterm cohort

The diffusion acquisition is described in Section 3.2. Whole brain 32-echo multi-component quantitative T_2 imaging was acquired at 1.2x1.2x3mm^3 resolution using a 2D GraSE acquisition at 12ms TE and resampled into the diffusion imaging space. In addition, proton Magnetic Resonance Spectroscopy (MRS) was acquired using water suppressed Point Resolved Spectroscopy (PRESS; TR/TE 2288/288ms) with a 14x13x11mm^3 voxel in the left posterior white matter. Spectra were analysed using the AMARES algorithm in the jMRUI spectroscopy package. Peak-area ratios of Cho/total creatine (Cr), NAA/Cho, and NAA/Cr, were calculated. MRS acquisition information was used to construct an estimate of the MRS voxel position in DWI space, thus defining a posterior white matter region of interest. Thalamus segmentations were carried out using the method described in [57] using a preterm-specific segmentation algo-

rithm [33].

C.5 Methods

C.5.1 Multi-component T_2 Relaxometry

Single exponential fitting of multi-echo or multi echo-time (TE) data can be used to generate quantitative maps of T_2 value [66]. We assume that the tissue composition can be described by a continuous (but computationally discrete and finite) set of compartments each with its own associated T_2 distribution undergoing exponential decay.

$$S(n) = \int m(T_2) e^{-n\mathrm{TE}/T_2} dT_2 \tag{C.1}$$

Of importance in this model is the detection of signal with $T_2 < 50ms$ which is associated with a water signal that is closely interacting with myelin. This provides an indirect measurement of myelin content, termed the myelin water fraction, v_{mwf} defined as the sum of all component magnitudes, $m(T_2)$, with a $T_2 < 50ms$ [127]. In the case of the neonatal data used here, which uses a multiply refocused echo train, the imaging sequence is theoretically susceptible to B_1-inhomogeneity [105]. Multi-spin echo T_2 decay generally assumes a train of perfect refocusing pulses which implies a perfectly homogenous B_1 field and uniform flip angle α. In practice this condition is not met with the consequence that stimulated echoes are produced along the echo train. However, these may be modelled using the Extended Phase Graph (EPG) algorithm [127] for n echoes in such a way that the local refocusing angle, can be estimated by simulating the history of previous imperfect refocusing pulses for N_c T_2 components. This effect can distort estimates of the T_2 distribution, particularly the short T_2 components. Initial T_2 component fitting was carried out using the extended phase graph algorithm (EPG) to extract a short component from three T_2 components to estimate the local applied flip angle α. We found that spatial homogeneity is high and flip angle remains above 90% of the applied angle. This weak inhomogeneity is not expected to distort a standard non-negative least squares multi-exponential fit [127].

C.5.2 Multi-compartment Diffusion Weighted Imaging

We fit a multi-compartment signal model to the multi-shell data using non-linear least squares specifically to estimate an intra-axonal volume fraction [165, 57].

$$S_a(b,\mathbf{x}) = S_{a0}\left[v'_{iso}e^{-bd_{iso}} + v'_i\int f(\mathbf{n},\gamma)e^{-bd_{||}(\mathbf{x}\cdot\mathbf{n})}d\Omega + v'_{ex}e^{-b\mathbf{x}D^*\mathbf{x}}\right] \tag{C.2}$$

The signal model attributes the white matter signal measured by DWI to three compartments; an intra-axonal space v'_i, and extra-axonal space v'_{ex} and a free-isotropic space v'_{iso} [4]. Given the experimental b-value, b, and gradient direction, $\mathbf{x}$, the signal from the intra-axonal and extra-axonal spaces is coupled by a specific distribution, $f(\mathbf{n},\gamma)$, which is assumed to represent axonal dispersion; formally a Watson distribution of oblateness γ, varying between 0, for highly oriented axons, up to 1 when there is no preferred structural orientation [165]. A principal diffusion direction incorporated into the extra-axonal diffusion tensor D^* can be defined by two angular parameters $\{\theta,\phi\}$. Lastly, $d_{||}$ and d_{iso} describe the parallel (to the principal diffuse direction) and isotropic diffusivities respectively.

C.5.3 Estimating an *in-vivo* g-ratio

Both axon diameter and myelin diameter have an impact on the physical properties of nerve conduction. The ratio of internal axonal diameter to the total nerve diameter (axon+myelin) is a useful number that has theoretical relationships to axonal conduction velocity and energetic cost. This measurement is known from *in vitro* and histological studies of the electrical properties of axons [37]. Emergent approximations of this *g-ratio*, can be measured using MRI [147, 106].

We approximate n axons as long cylinders with an internal axon radius of r_{in} and an external myelin+axonal radius of r_{out}. Assuming a cylindrical geometry, the intra-axonal space is given by $v_i = n2\pi r_{in}^2 s_{||}$ and the myelin volume by $v_{mwf} = n2\pi(r_{out}^2 - r_{in}^2)s_{||}$ where $s_{||}$ is a fixed axonal length. Taking the ratio of v_{mwf}/v_i yields an expression for the bulk average g-ratio, Γ (C.3) in terms of the myelin volume v_{mwf} and the intra-axonal volume v_i, capitalised to represent the bulk average nature of this measurement.

$$\Gamma = \left(\frac{v_{mwf}}{v_i} + 1\right)^{-\frac{1}{2}} \tag{C.3}$$

Using only DWI or multi-component relaxometry is insufficient to estimate both v_i and v_{mwf}. To reconcile these two modalities we make use of a four-compartment tissue model [4].

$$S_{total} = v_{mwf}S_1 + v_iS_2 + v_eS_3 + v_{iso}S_4 \tag{C.4}$$

The last three compartments of (C.4) are measurable using a multi-compartment diffusion model [165]. The model allows for the estimation of the signal from multiple compartments, specifically the intra-axonal volume fraction associated with highly directional structure, v_i. The remaining model compartment for S_1 describes signal associated, in white matter, primarily with myelin and can be estimated by T_2 relaxometry. Finally, because the diffusion signal model contains no signal from S_1 it is necessary to multiply the estimates of v_i', v_{ex}' and v_{iso}' from the diffusion measurement (Eq. C.2) by $(1 - v_{mwf})$ and hence, $v_i = v_i'(1 - v_{mwf})$. If the change in a diffusion imaging parameter such as v_i' was purely due to a change in local quantity of myelin (or at least DWI invisible structure), then the new value could be estimated from the old value and the correction factor of $1 - v_{mwf}$.

C.5.4 Regions of interest

Thalamus regions of interest are defined using a preterm specific segmentation routine [33]. *Posterior white matter* (*PWM*) regions of interest are defined by the spectroscopy voxel placement. *PWM-tract* based regions of interest are defined between the thalamus ROI and the posterior white matter ROI. For this purpose we use the multi-directional ball and stick model and probabilistic tractography method described in [23]. Connectivity distributions are defined between the thalamus as a seed mask and the posterior white matter MRS voxel as the target mask. The distributions are then used to form weighted parameter estimates for this regions of interest. Furthermore, a *thalamus-tract* ROI is defined by the number of times each voxel within the thalamus seed mask is able to reach the *PWM* target region. This implicitly weights the *thalamus* ROI by how easily each voxel within it can reach the *PWM* ROI. For each infant, longitudinal progression in the values of v_i, v_{mwf}, Γ and T_2 can then be observed in space as well as between estimated gestational ages.

Thus for each infant we are able to show results that have been weighted for both: 1) the thalamus, weighted by how easy it is for a tractography algorithm beginning in

a particular voxel within the thalamus mask to reach any part of the MRS voxel (as a percentage of the number of trials); and 2) the posterior white matter region that is passed through by the tractography algorithm between the thalamus and the MRS voxel, weighted by how often each voxel is traversed. We adopt this pragmatic, hydrostatic connectivity, definition of what is meant by the results of a tractography algorithm to avoid biological interpretation fallacies when using notions of fibre connectivity and fibre integrity [77].

Cross-sectional ROIs are manually delineated for each infant in the four regions: the bilateral posterior and anterior limbs of the internal capsule (PLIC and ALIC respectively) and the genu and splenium of the corpus callosum (Figure C.1E and C.1F). We additionally investigate manually placed bilateral regions of interest in the anterior white matter for comparison with the spectroscopic voxel in the posterior white matter.

C.5.5 Statistical Analysis

Two sample t-tests were used between imaging parameters. Results are reported to be significant if the corresponding statistical p-value is less than 0.05. Results that are corrected for age at birth or age at scan are reported from partial linear correlation coefficients with statistical significance if the (equivalent) p-value is less than 0.05. Parameter rates of change are estimated from linear fits to the parametric data and gestational age. Parameter rates of change are compared through the use of the Fisher z-transform.

C.6 Results

Figure C.1 shows white matter spectroscopy and thalamic masks and MWF maps for a representative term age infant. Masks defined by the spectroscopy voxel and of the thalamus using the data and method of [57] are shown overlaid on T_2-weighted images. The estimated MWF for this infant is shown overlaid on T_2-weighted and FA maps from the diffusion imaging. Thalamic and spectroscopy voxel masks are used as endpoints of tractography in Section C.6.3.

Results are divided into four sections: Section C.6.1 analyses parameter changes in the preterm thalamus; Section C.6.2 analyses parameter changes in the posterior white matter; Section C.6.3 analyses parameter changes along the diffusion pathway

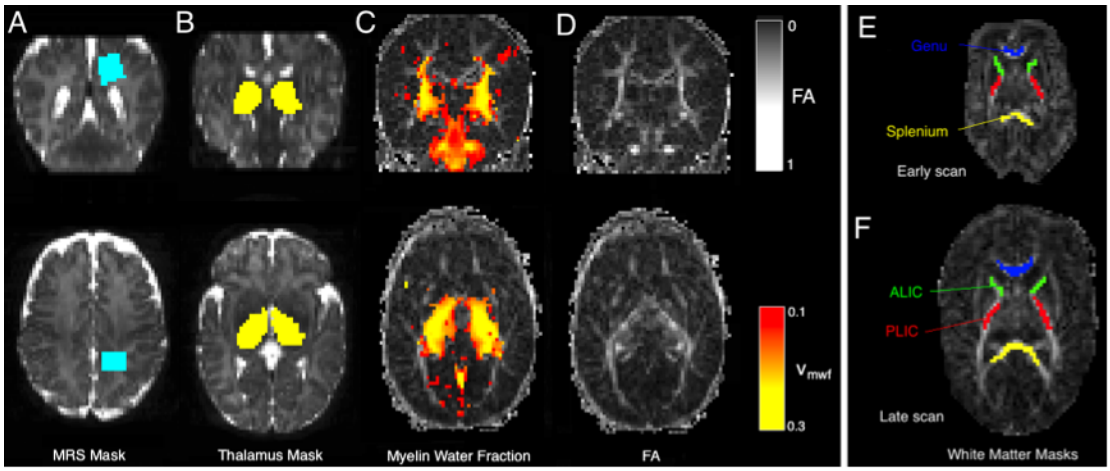

Figure C.1: Example imaging data for single term-infant. A) T_2-weighted image overlaid with MRS voxel position, B) T_2- weighted image overlaid with thalamic segmentation, C) Estimated regions of myelin water fraction > 0.01 overlaid on FA map and D) FA map. Example white matter regions of interest (PLIC, ALIC, genu and splenium) are shown for E) an early scan and F) a term-equivalent age scan.

connecting these two regions and finally; Section C.6.4 analyses results from the entire, and larger, cross-sectional cohort.

C.6.1 Longitudinal diffusion and myelin water fraction changes in the preterm thalamus

Imaging parameter estimates for all longitudinal infants are shown in Table C.2. Thalamic T_2 decreases from an average of 203 ± 7ms to 181 ± 7ms (correlation coefficient ρ=-0.84, $p \leq 0.001$). This is associated with a short T_2 component that increases its volume fraction from 0.05 ± 0.02 to 0.11 ± 0.02 (ρ=0.87, $p \leq 0.0001$). Adjusting the diffusion MRI measured intra-axonal change with knowledge of the myelination change using the correction strategy in Section C.5.3 suggests that myelin alone is insufficient to explain the longitudinal increase in v_i in the preterm thalamus, accounting for less than a third (0.27 ± 0.06) of the observed change. Additionally, the estimated voxel average g-ratio, Γ, is seen to decrease with increasing equivalent gestational age.

C.6.2 Longitudinal diffusion and myelin water fraction changes in the preterm posterior white matter

Table C.3 contains imaging parameter values for the MRS region of interest defined in the posterior white matter of each infant. T_2 values fall over this approximately 10 week

Infant	EGA (wks)	v_i'	v_{mwf}	Corrected v_i	Γ	T_2 (ms)
1b	26.14					
1p	33.14	0.189 (0.0032)	0.0586 (0.0025)	0.178 (0.003)	0.874 (0.005)	203 (2)
1t	40.14	0.241 (0.0026)	0.115 (0.0027)	0.213 (0.0024)	0.823 (0.0039)	177 (1.9)
2b	25.14					
2p	31.43	0.188 (0.0028)	0.0678 (0.002)	0.175 (0.0026)	0.857 (0.004)	197 (1.1)
2t	42	0.245 (0.0021)	0.132 (0.0028)	0.213 (0.0019)	0.806 (0.0038)	175 (1.5)
3b	25.14					
3p	31	0.175 (0.0026)	0.0289 (0.0011)	0.17 (0.0025)	0.926 (0.0029)	204 (1.2)
3t	42	0.242 (0.0019)	0.11 (0.0024)	0.215 (0.0018)	0.829 (0.0034)	172 (1.7)
4b	27.14					
4p	30.86	0.166 (0.0039)	0.0353 (0.0012)	0.16 (0.0037)	0.908 (0.0034)	208 (0.76)
4t	46.29	0.258 (0.0023)	0.115 (0.0026)	0.228 (0.0021)	0.832 (0.0035)	178 (2.3)
5b	27.14					
5p	29.86	0.154 (0.0026)	0.045 (0.0019)	0.147 (0.0025)	0.88 (0.0047)	215 (1.3)
5t	46.29	0.264 (0.0025)	0.109 (0.0034)	0.235 (0.0024)	0.842 (0.0046)	186 (2.8)
6b	26.29					
6p	31.86	0.183 (0.0037)	0.0712 (0.0023)	0.17 (0.0034)	0.849 (0.0049)	194 (1.7)
6t	40.29	0.216 (0.0026)	0.0899 (0.0033)	0.197 (0.0025)	0.84 (0.0052)	192 (2.8)
7b	26.29					
7p	34.57	0.191 (0.0037)	0.0394 (0.0016)	0.183 (0.0035)	0.911 (0.0037)	200 (1.4)
7t	40.29	0.248 (0.0022)	0.0846 (0.0026)	0.227 (0.0021)	0.863 (0.0038)	185 (2.4)

Table C.2: Thalamic parameter values for multi-modal MRI. Data is shown at birth (b), early scan (p) and late scan (t). Confidence intervals on the mean are shown in parenthesis. Errors for v_i and Γ are estimated using the general formula for propagation of uncertainty. Corrected v_i values are shown after using the correction strategy described in Section C.5.3.

gestational period (299 ± 11ms to 205 ± 93ms) whilst NAA/Cho increases (0.40 ± 0.09 to 1.04 ± 0.17) and Cho/Cr decreases (2.79 ± 0.16 to 1.80 ± 0.34).

C.6.3 Longitudinal diffusion and myelin water fraction changes in the thamalo-posterior white matter region

Combined results for each infant with longitudinal data are shown in Figure C.3. For each infant we show results from the entire thalamus, and posterior white matter (see Table C.2 and Table C.3), but additionally show parameter values that have been weighted for the thalamus and the posterior white matter regions that are passed through by the tractography algorithm. For each infant, longitudinal progression in the values of v_i, v_{mwf}, Γ and T_2 can be observed in space as well as between (equivalent) gestational ages.

Figure C.3 illustrates the spatio-temporal changes for this group of seven infants. Each infant has four data points, at each of the two time-points. Datapoints from the same scan are connected by solid grey lines. The marker style of these lines indicates the infant number (see figure legend) and is the same at both early and late scans. The

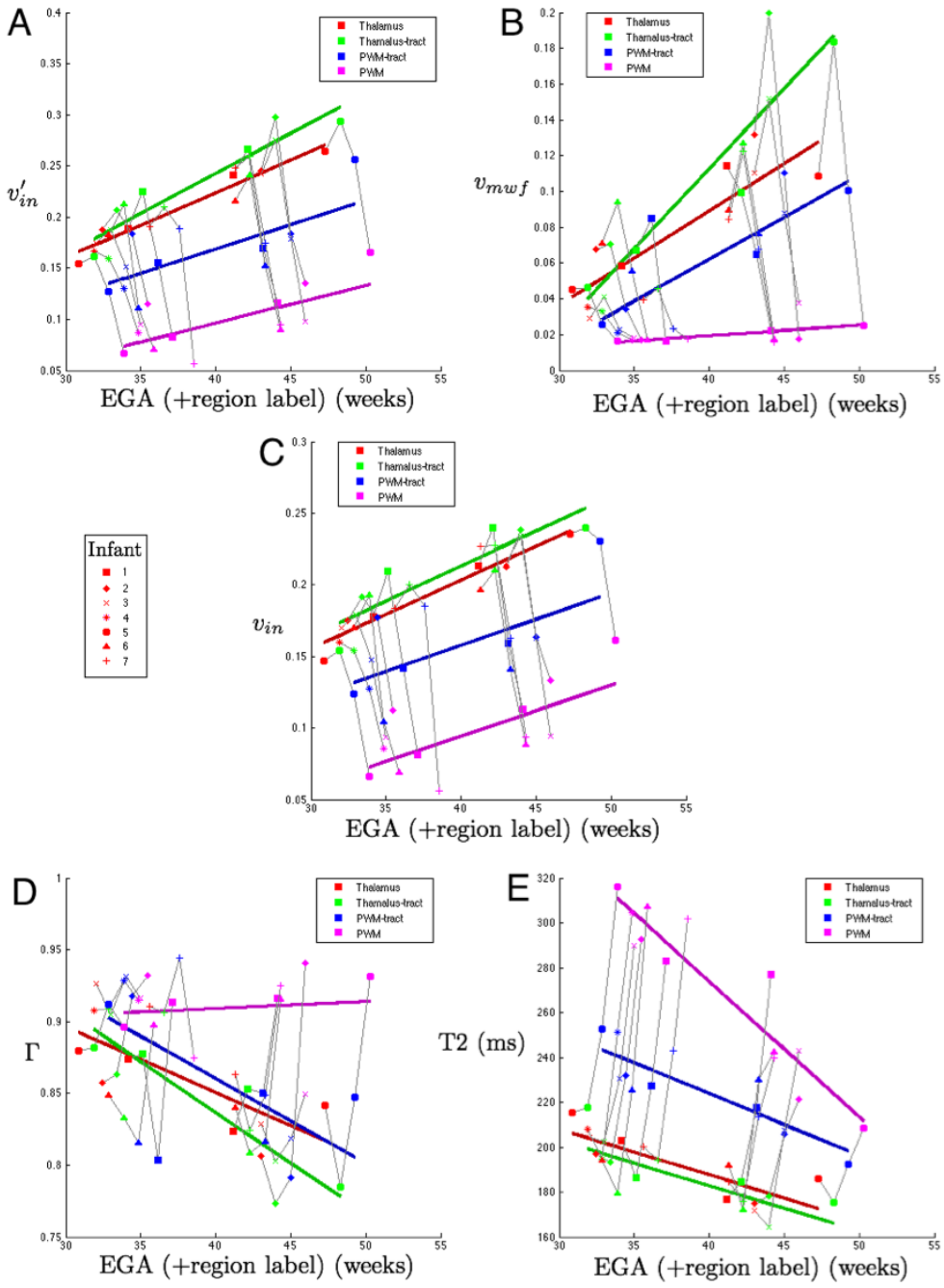

Figure C.2: Combined results for individual infants showing spatiotemporal parametric changes estimated over: in Red) the entire thalamus (Thalamus); Green) thalamic voxels weighted by how often tracts appear to reach the MRS voxel (Thalamus-tract); Blue) white matter voxels representing the most commonly found paths from the thalamus to the posterior white matter (PWM-tract); and Magenta) average values in the MRS voxel (PWM) and A) v_{in} (uncorrected) B) v_{mwf} C) v_i (corrected v_i) D) g-ratio E) T_2. Results for Thalamus-tract, PWM-tract and PWM are displayed offset by 1, 2 and 3 in weeks respectively for clarity.

first datapoint for each infant is located at the EGA at the time of the scan, subsequent connected points are spatially separated by 1 week to aid visualisation. Solid coloured

Infant	EGA (wks)	v_i'	v_{mwf}	Corrected v_i	T_2 (ms)	NAA/Cho	Cho/Cr
1b	26.14						
1p	33.14	0.083 (0.073)	0.0164 (0.004)	0.0817 (0.072)	283 (42)	0.475	2.73
1t	40.14	0.116 (0.073)	0.0221 (0.018)	0.113 (0.072)	277 (42)	-	-
2b	25.14						
2p	31.43	0.115 (0.15)	0.0173 (0.005)	0.113 (0.14)	292 (40)	0.36	2.77
2t	42	0.135 (0.052)	0.0177 (0.02)	0.133 (0.051)	222 (27)	1.24	1.61
3b	25.14						
3p	31	0.095 (0.098)	0.0182 (0.008)	0.0935 (0.096)	290 (38)	0.475	2.79
3t	42	0.098 (0.053)	0.0376 (0.034)	0.094 (0.051)	243 (35)	1.06	1.5
4b	27.14						
4p	30.86	0.087 (0.075)	0.017 (0.006)	0.0854 (0.074)	305 (45)	0.445	2.58
4t	46.29	-	-	-	-	-	-
5b	27.14						
5p	29.86	0.067 (0.065)	0.0165 (0.004)	0.0659 (0.063)	316 (49)	0.334	2.69
5t	46.29	0.166 (0.045)	0.0253 (0.026)	0.162 (0.044)	209 (30)	1.04	1.86
6b	26.29						
6p	31.86	0.070 (0.087)	0.0169 (0.004)	0.0692 (0.085)	307 (36)	0.467	2.88
6t	40.29	0.090 (0.073)	0.0175 (0.007)	0.0887 (0.071)	242 (51)	-	-
7b	26.29						
7p	34.57	0.057 (0.06)	0.0176 (0.004)	0.056 (0.059)	302 (43)	0.251	3.08
7t	40.29	0.095 (0.068)	0.016 (0.008)	0.0933 (0.067)	240 (48)	0.828	2.25

Table C.3: Posterior white matter parameter values for multi-modal MRI shown for v_i' estimated from diffusion MRI, T_2 value and MRS NAA/Cho and Cho/Cr values. Data is shown at birth (b), early scan (p) and late scan (t). Confidence intervals on the mean are shown in parenthesis. Term equivalent age spectroscopy data for infant 4 is unavailable. Corrected v_i values are shown after using the correction strategy described in Section C.5.3.

lines show trends in the parameter values in each region with time across the cohort. Separation in tissue properties by location is shown across these seven infants: comparing the values found in the unweighted and tract-weighted thalamus masks (see Table C.2) shows higher values of v_i and v_{mwf} in the weighted thalamus measurement and additionally those regions have the lowest values of g-ratio and T_2. The lowest T_2 values are estimated within the thalamus region, with little difference between the results of the weighted and unweighted thalamus mask. In the thalamus, the highest values for v_{mwf} are seen using the weighted mask, suggesting that the regions of highest v_i, (and also directionality, measured by the tractography) are associated with those regions that are estimated to contain the most myelin water. The highest values for T_2 are found in the unweighted spectroscopy voxel, with substantially lower values in the diffusion-derived tract system passing between thalamus and spectroscopy voxel. The strong fall in T_2 in the posterior white matter voxel is accompanied by an increase in v_i as measured by the DWI model and little change in the amount of myelin estimated in this region.

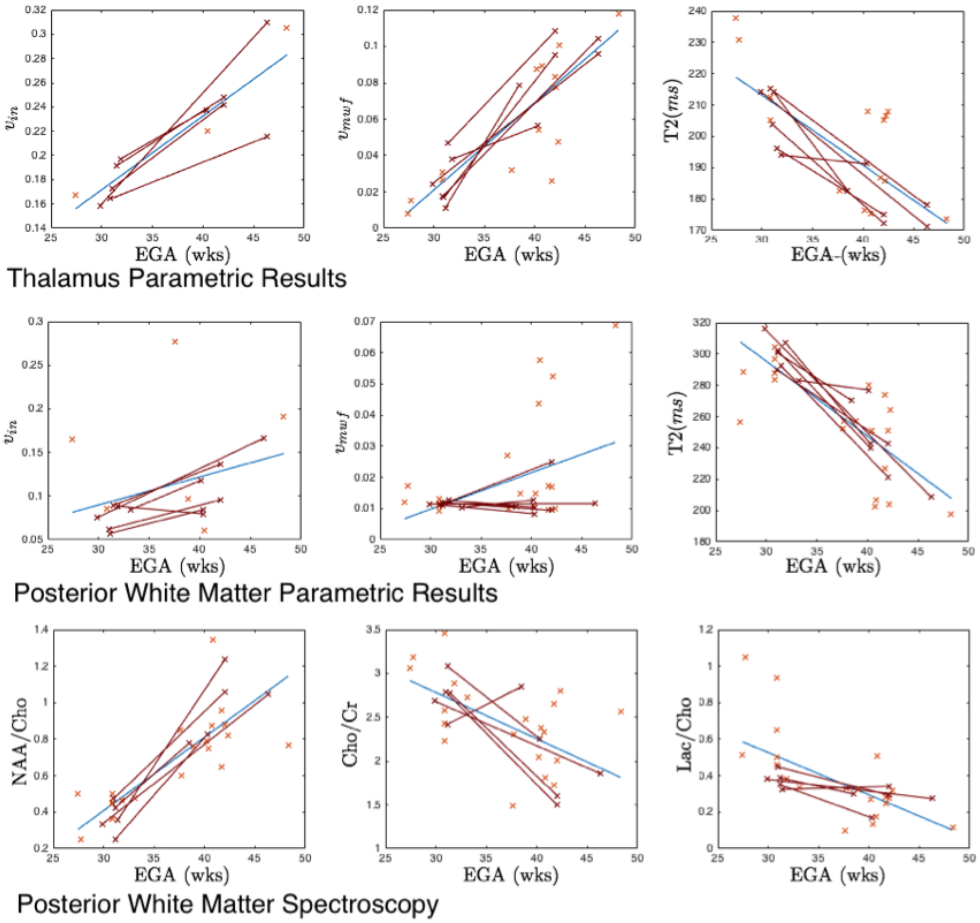

Figure C.3: Cross sectional changes in v_i, T_2 and spectroscopy. Figures a-c) *thalamus* parametric results for intra-axonal volume fraction v_i, myelin water fraction v_{mwf} and free water volume v_{iso} respectively; d-h) *Posterior white matter* parametric results defined in the spectroscopy voxel ROI for v_i, myelin water fraction v_{mwf}, Tissue T_2, tissue volume fraction v_{tissue} and free water volume v_{iso} respectively; i-k) spectroscopy ratios NAA/Cho, Cho/Cr and Lac/Cho respectively. Cross-sectional data is shown in blue, with blue trend line. Longitudinal data are shown in red, connected by red lines.

C.6.4 Cross-sectional parametric correlations in preterm white matter

This section contains results for the larger cross-sectional cohort of infants, including those with longitudinal data. Figure C.4 shows trends in the parameter values for this larger group. Cross sectional trend lines are shown in blue, whilst longitudinal results are shown connected with red lines. In the thalamus (figure C.4a-c), tissue T_2 is seen to decrease at a rate of 2.24ms/wk ($r = 0.76$, $p < 1 \times 10^{-7}$), v_{mwf} increases at a rate of 0.48%/wk ($r = 0.86$, $p < 1 \times 10^{-7}$). In the posterior white matter (figure C.4d-h), tissue

T_2 is seen to decrease at a rate of 5ms/wk ($r = 0.80$, $p < 1 \times 10^{-7}$), v_{mwf} increases at a rate of 0.1%/wk ($r = 0.44$, $p = 0.011$), v_{iso} decreases at a rate of 2.7%/wk ($r = 0.87$, $p < 1 \times 10^{-10}$) and v_{tissue} increases at a rate of 2.6%/wk ($r = 0.87$, $p < 1 \times 10^{-9}$).

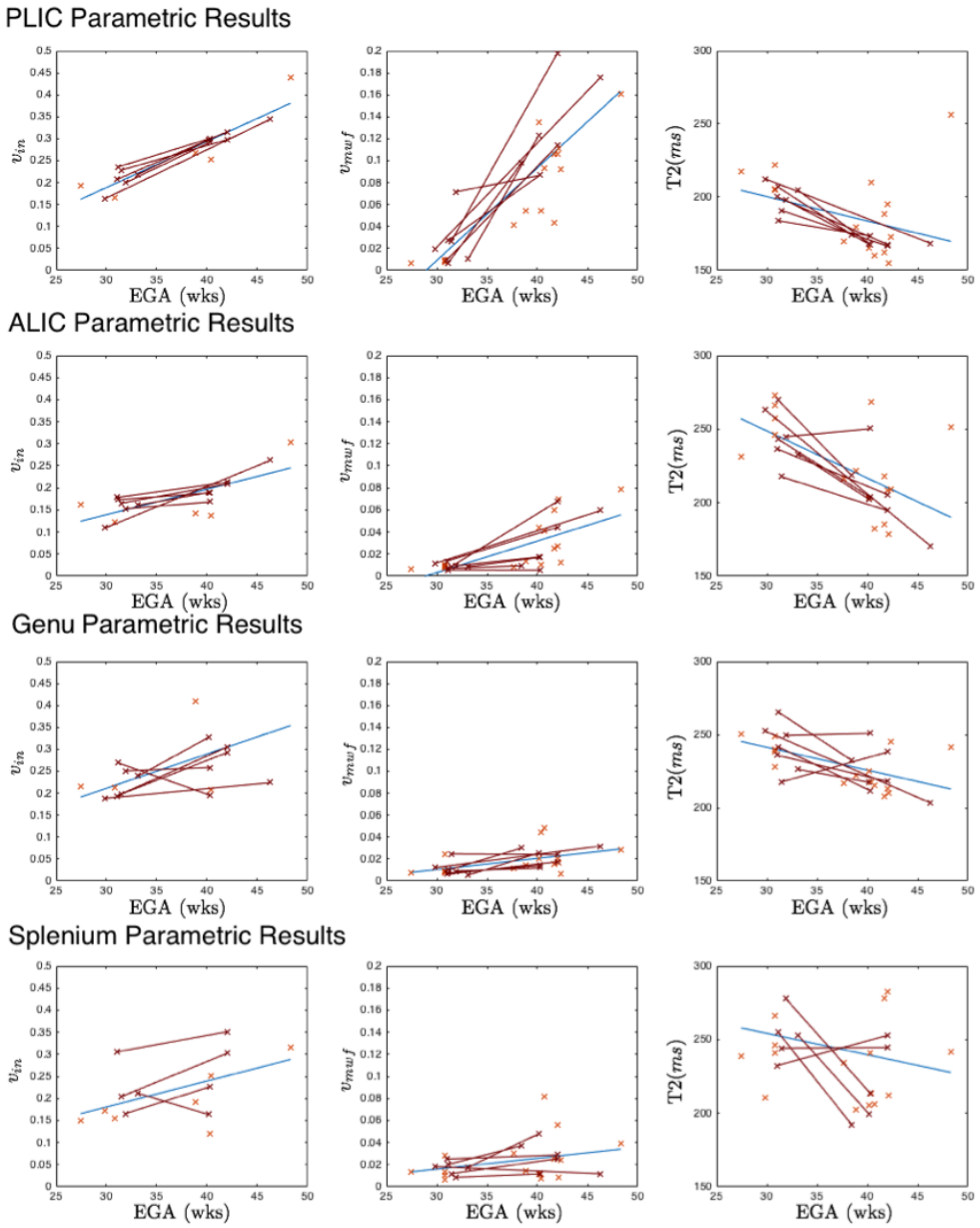

Figure C.4: Cross sectional correlations between T_2 relaxometry and spectroscopy for a) T_2 against NAA/Cho ratio, b) vtissue against NAA/Cho ratio and c) viso against NAA/Cho ratio. Cross-sectional data is shown in blue, with blue trend line. Longitudinal data are shown in red, connected by red lines.

Figure C.4 shows changes in v_i,. v_{mwf} and T_2 in four central white matter regions. The top row of Figure 4 shows results for the PLIC, showing trends for increasing v_i ($r = 0.93 p < 1 \times 10^{-7}$) and v_{mwf} (r = 0.86, $p < 1 \times 10^{-8}$) and decreasing T_2 (r = -

0.41, p=0.026) in both cross-section and for the longitudinal infants with growth rates of 1%/wk, 0.8%/wk and -1.67ms/wk respectively. v_{mwf} values in the PLIC are quite high, commensurate with earlier myelination in this region and in contrast to what is expected in the ALIC (Figure 4, second row) which has slower measured increases in v_i (0.5%/wk, r=0.75 $p < 1 \times 10^{-4}$) and v_{mwf} (0.2%/wk, r=0.72 $p < 1 \times 10^{-5}$). Although measurements of both v_i and v_{mwf} are significantly lower in the ALIC than the PLIC, the difference in growth rate is found to be significant only for v_i but not for v_{mwf}.

In the corpus callosum (Figure C.4 , third and fourth rows), results for the genu and splenium are found to be quite similar. Both regions have quite low measured values of v_{mwf} and comparable values of v_i. Both v_i and v_{mwf} are found to be increasing in the genu (v_i: 0.8%/wk r=0.58, p=0.015) (v_{mwf}: 0.1%/wk r=0.52, p=0.004), but increases do not reach significance in the splenium (v_i p=0.06, v_{mwf} p=0.09). T_2 values in both regions are falling (-1.56ms/wk (genu) vs -1.35ms/wk (splenium)), but this only reaches significance in the genu (r=0.55, p=0.002) compared to the splenium (r=0.19, p=0.34).

Figure C.5 investigates the relationship between white matter T_2 and spectroscopy. There is a high correlation between NAA/Cho ratio and T_2 ($r = 0.79$, $p < 1 \times 10^{-6}$) which, by comparison with the results in Figure C.4, could be related to a decrease in free-water volume fraction and replacement by structured, but unmyelinated tissue, with shorter T_2. Correcting for equivalent gestation age reduces the correlation between NAA/Cho ratio and T_2 ($r = 0.49$, $p = 0.008$), but does not remove the significant interaction entirely. Correlations between NAA/Cho and v_{tissue} and v_{iso} are also significant correcting for equivalent gestational age ($r = 0.43$, $p < 0.02$ and $r = 0.44$, $p < 0.019$ respectively). Comparison with tissue properties in the anterior white matter reveals similar, but less strong trends, the correlation between AWM T_2 and PWM NAA/Cho is strongly significant (r = 0.76, $p < 1 \times 10^{-6}$) falling to r=0.35 (p=0.08 — no longer significant) when correcting for EGA. Although uncorrected trends between NAA/Cho and T_2 in PWM and AWM are not significantly different from one another using a Fisher transform, correcting for gestational age dependence reveals that the correlation is much weaker between AWM T_2 and PWM NAA/Cho than for PWM T_2 and PWM NAA/Cho. This result is commensurate with differential rates of tissue development in the anterior and posterior brain once the general effect of gestational age is removed.

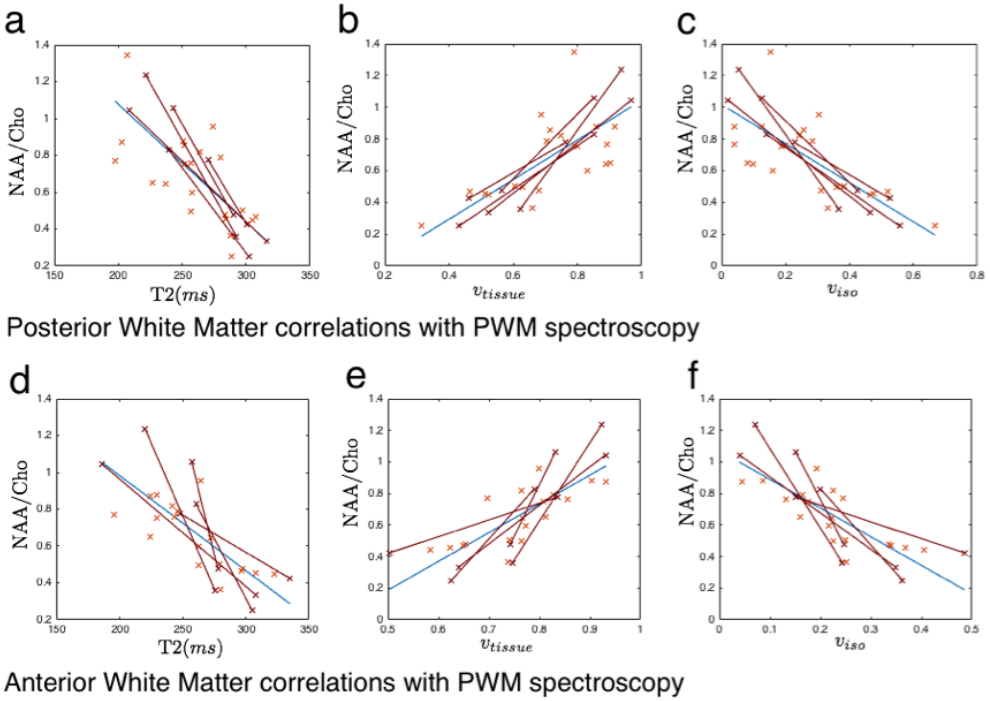

Figure C.5: Cross sectional correlations between white matter T_2 relaxometry and spectroscopy for top row: a) PWM T_2 against PWM NAA/Cho ratio, b) PWM vtissue against PWM NAA/Cho ratio and c) PWM viso against PWM NAA/Cho ratio and bottom row: a) AWM T_2 against PWM NAA/Cho ratio, b) AWM vtissue against PWM NAA/Cho ratio and c) AWM viso against PWM NAA/Cho ratio Cross-sectional data is shown in blue, with blue trend line. Longitudinal data are shown in red, connected by red lines.

C.7 Discussion

In this work we have investigated how properties derived from both diffusion imaging and multi-component T_2 relaxometry change in the developing thalami-cortical system between 27-58 weeks equivalent gestational age (EGA) as assessed cross-sectionally on a cohort of 37 infants, including a sub-cohort of longitudinal data for seven infants. We have combined results from DW MRI, T_2 relaxometry, and proton spectroscopy to study longitudinal changes between two time-points intra-subject. In contrast to previous work, here we combined only quantitative measurements such as the intra-axonal and myelin-water volumes in contrast to surrogate measurements, such as the fractional anisotropy or the single-component T_2.

The imaging data acquired on this cohort has shown how MR measurable tissue properties vary longitudinally over the preterm period. Data from the diffusion imaging suggests that the intra-axonal volume fraction increases in both the thalamus and the

posterior white matter over this period which matches previous work [87, 57]. Data from multi-compartment T_2 relaxometry suggest that the myelin water fraction also increases in both these regions, although the increase in the thalamus is of greater magnitude. Additionally, the estimated myelin water fraction can be used to correct the volume fractions measured from the diffusion imaging since DWI is non-specific to myelination [96]. The result shows that increasing myelin content in the thalamus accounts for about one third of the change in axonal volume fraction measured solely from DWI. Additionally, the changes seen in the spectroscopy ratios of an increase in NAA/Cho and decrease in Cho/Cr are comparable to 1.5T values, although here the results are longitudinal not cross-sectional [83, 81]. The correlation between T_2 and NAA/Cho that persists after correction for EGA suggests a synergy in the relationship between measured tissue structure and function.

The multi-modal data presented in this work has allowed some of the confounding factors related to mono-modal neonatal data to be explored. Of note, the rapid decrease in white matter T_2 value is associated with a decrease in free water and an increase of tissue volume fraction. In general, the contribution of myelination (or strictly here v_{mwf}) is quite minor, and we attribute the dominant change to (unmyelinated) axonal and glial proliferation, as suggested by the multi-modal results in Figure C.3. This structural change is associated with increase NAA/Cho ratio which could imply an increase in the volume of functional tissue. Conversely in the thalamus, the increase in intra-axonal volume fraction is shown to be related to myelination as suggested in [57], but this does not entirely explain the tissue changes observed. About two-thirds of this tissue structural change must be the result of other tissue composition changes contributing to increased apparent intra-axonal volume fraction (and thus FA) in this region. In addition to the thalamus, we have shown how the posterior white matter section of the thalamo-cortical system is developing in the seven infants with longitudinal data. This data quantifies our general observations of tissue parameter change to specific individual cases and we are able to infer increases in thalamic myelin water fraction, changes to the white matter fibre structure and also infer how this correlates to functional spectroscopic data in the region to which it is connected.

Results in the white matter PLIC and ALIC show differentiation in axonal and myelin density with high v_{mwf} values in the posterior limb and much lower values in

the ALIC despite relatively similar values of v_i. Differential axonal and myelin density changes in these regions may make them good markers of future developmental changes, although the direct v_i measurements should be corrected by (1-v_{mwf}) to remove the contribution of the myelin water space to the axonal density measurement. In the corpus callosum imaging properties related to axonal density, myelin density and T_2 change in tandem and rates of change in these measurements are not distinguishable. Although some authors have found differences in imaging parameters between the genu and splenium [123], the size of the cohort used in our work is quite low and the baseline of measurements quite narrow compared to other larger scale cross-sectional studies.

It is possible that over the gestational ages that we are measuring, that there is either a normalisation of imaging parameters towards term equivalent age, or an otherwise variable rate of change [14]. The results in Figures C.3 and C.4 do not support this observation, and appear to suggest that the opposite may be true especially for those areas that are beginning to myelinate over this late gestational period. This is suggested by the v_{mwf} results in the genu and splenium in Figure C.4 where the parameter variability increases. Figure C.3 further suggests that the variability on the cross-sectional measurements increases with gestational age. Over the longer-term (the first year of life) parameter variability should reduce and stabilise, but in the period we are measuring there is rapid change in tissue volume and composition. Interestingly the individual parameter trajectories of the longitudinal infants are relatively similar to one another. The results in Figure C.3 and 4, and the limitation of only two timepoints for some subjects makes it difficult to infer variable or non-linear parameter trajectories.

The main limitation of this work is the low number of infants with longitudinal data, although the number of infants with a single scan is much higher. Obtaining repeated MR acquisitions on this vulnerable cohort is challenging; especially with a relatively low initial number of extremely preterm infants suitable for scanning. However, data of this type is fundamental to understanding brain maturation and the effect of preterm birth on brain maturation. Ideally, multiple time-points would be acquired on each infant during their time in the NICU, but this is not possible. The variation in the range of equivalent gestational ages at scan is also an unavoidable limitation of our work. Some longitudinal imaging timepoints are more widely separated than others

and it is unclear what the effect of this will be on our description of longitudinal parameter changes. The cross-sectional data in our work appear well supported by linear relationships, although there is some evidence that parameter changes over this range of equivalent gestational ages may not be linear [14]. With the data that we have, it is difficult with two longitudinal imaging time points to support an alternative model, and it is not clear how models applied to cross-sectional data should really be applied in the longitudinal setting. However, the underlying results that suggest an increase in both thalamus axonal density and thalamus myelin density are unlikely to be altered. Although the combination of DWI and T_2 relaxometry makes many assumptions about the image formation process (this is also true of the individual modalities too), the combination of these data does allow new information to be obtained. Importantly, measurement of the *g*-ratio can be linked speculatively with simple physical models to predict the effect of change in myelin thickness on conduction velocity and energetic efficiency [37, 106].

Future work will use this multi-modal approach to make predictions about functional development in preterm children. This is plausible since there is a well-defined sequence of myelination from the PLIC outward [29], and delays to this might predict corresponding delays in functional progression of motor, language and executive function as the brain increases functional electrical energetic efficiency. Irrespective of the combination of measurements in this work, broader adoption of multi-shell DWI and multi-echo T_2 imaging within clinically feasible time frames is important, and will stimulate the generation of novel predictive structural biomarkers with a tangible physical link to neuronal function.

One of the main contributions of this work is the combination of results from a number of notionally quantitative imaging modalities. Investigation of mono-modal properties can only reveal so much about the developing brain. In isolation, imaging modalities can only be so informative: multi-modal data analysis can use complementary information to build up a more complete picture.

Bibliography

[1] M. Aggarwal, D. W. Nauen, J. C. Troncoso, and S. Mori, "Probing region-specific microstructure of human cortical areas using high angular and spatial resolution diffusion MRI," *NeuroImage*, 2014.

[2] M. Ajayi-Obe, N. Saeed, F. M. Cowan, M. A. Rutherford, and A. D. Edwards, "Reduced development of cerebral cortex in extremely preterm infants," *The Lancet*, vol. 356, no. 9236, pp. 1162–1163, 2000.

[3] D. C. Alexander and G. J. Barker, "Optimal imaging parameters for fiber-orientation estimation in diffusion MRI." *NeuroImage*, vol. 27, no. 2, pp. 357–67, 2005.

[4] D. C. Alexander, P. L. Hubbard, M. G. Hall, E. A. Moore, M. Ptito, G. J. M. Parker, and T. B. Dyrby, "Orientationally invariant indices of axon diameter and density from diffusion MRI." *NeuroImage*, vol. 52, no. 4, pp. 1374–89, 2010.

[5] D. C. Alexander, D. Zikic, J. Zhang, H. Zhang, and A. Criminisi, "Image quality transfer via random forest regression: Applications in diffusion MRI," in *LNCS: MICCAI*, vol. 8675: Part, 2014, pp. 225–232.

[6] M. Anjari, L. Srinivasan, J. M. Allsop, J. V. Hajnal, M. A. Rutherford, A. D. Edwards, and S. J. Counsell, "Diffusion tensor imaging with tract-based spatial statistics reveals local white matter abnormalities in preterm infants." *NeuroImage*, vol. 35, no. 3, pp. 1021–7, 2007.

[7] A. Anwander, A. Pampel, and T. Knosche, "In vivo measurement of cortical anisotropy by diffusion-weighted imaging correlates with cortex type," *Proc. Int. Soc. Magn. Reson. ...*, vol. 18, p. 2403, 2010.

[8] Y. Assaf and P. J. Basser, "Composite hindered and restricted model of diffusion (CHARMED) MR imaging of the human brain." *NeuroImage*, vol. 27, no. 1, pp. 48–58, 2005.

[9] Y. Assaf and O. Pasternak, "Diffusion tensor imaging (DTI)-based white matter mapping in brain research: a review." *Journal of molecular neuroscience : MN*, vol. 34, no. 1, pp. 51–61, 2008.

[10] Y. Bai and D. C. Alexander, "Model-based registration to correct for motion between acquisitions in diffusion MR imaging," in *IEEE International Symposium on Biomedical Imaging: from Nano to Macro*, vol. 1-4, 2008, pp. 947–950.

[11] G. Ball, J. P. Boardman, D. Rueckert, P. Aljabar, T. Arichi, N. Merchant, I. S. Gousias, A. D. Edwards, and S. J. Counsell, "The effect of preterm birth on thalamic and cortical development." *Cerebral Cortex*, vol. 22, no. 5, pp. 1016–24, 2012.

[12] G. Ball, S. J. Counsell, M. Anjari, N. Merchant, T. Arichi, V. Doria, M. A. Rutherford, A. D. Edwards, D. Rueckert, and J. P. Boardman, "An optimised tract-based spatial statistics protocol for neonates: applications to prematurity and chronic lung disease." *NeuroImage*, vol. 53, no. 1, pp. 94–102, 2010.

[13] G. Ball, L. Pazderova, A. Chew, N. Tusor, N. Merchant, T. Arichi, J. M. Allsop, F. M. Cowan, A. D. Edwards, and S. J. Counsell, "Thalamocortical connectivity predicts cognition in children born preterm," *Cerebral Cortex*, vol. 25, no. 11, pp. 4310–4318, 2015.

[14] G. Ball, L. Srinivasan, P. Aljabar, S. J. Counsell, G. Durighel, J. V. Hajnal, M. A. Rutherford, and A. D. Edwards, "Development of cortical microstructure in the preterm human brain." *Proceedings of the National Academy of Sciences of the United States of America*, vol. 110, no. 23, pp. 9541–6, 2013.

[15] A. J. Barkovich, B. O. Kjos, D. E. Jackson, and D. Norman, "Normal maturation of the neonatal and infant brain: MR imaging at 1.5 T'," *Radiology*, pp. 173–180, 1988.

[16] P. J. Basser, J. Mattiello, and D. Lebihan, "MR diffusion tensor spectroscopy and imaging." *Biophysical journal*, vol. 66, no. January, pp. 259–267, 1994.

[17] P. J. Basser and C. Pierpaoli, "Microstructural and Physiological Features of Tissues Elucidated by Quantitative-Diffusion-Tensor MRI," *Journal of Magnetic Resonance, Series B*, vol. 111, no. 3, pp. 209–219, 1996.

[18] P. Basser, "Inferring microstructural features and the physiological state of tissues from diffusion-weighted images," *NMR in Biomedicine*, vol. 8, pp. 334–344, 1995.

[19] D. Bates, M. Mächler, B. Bolker, and S. Walker, "Fitting Linear Mixed-Effects Models Using {lme4}," *Journal of Statistical Software*, vol. 67, no. 1, pp. 1–48, 2015.

[20] P.-L. Bazin and D. L. Pham, "Topology correction of segmented medical images using a fast marching algorithm," *Computer Methods and Programs in Biomedicine*, vol. 88, no. 2, pp. 182–190, 2007.

[21] C. Beaulieu, *The biological basis of diffusion anisotropy*, 2nd ed. Elsevier, 2009.

[22] S. Beck, D. Wojdyla, L. Say, A. P. Betran, M. Merialdi, J. H. Requejo, C. Rubens, R. Menon, and P. F. A. van Look, "The worldwide incidence of preterm birth: a systematic review of maternal mortality and morbidity." *Bulletin of the World Health Organization*, vol. 88, no. 1, pp. 31–8, 2010.

[23] T. E. J. Behrens, H. J. Berg, S. Jbabdi, M. F. S. Rushworth, and M. W. Woolrich, "Probabilistic diffusion tractography with multiple fibre orientations: What can we gain?" *NeuroImage*, vol. 34, no. 1, pp. 144–155, 2007.

[24] T. E. J. Behrens, H. Johansen-Berg, M. W. Woolrich, S. M. Smith, C. A. M. Wheeler-Kingshott, P. A. Boulby, G. J. Barker, E. L. Sillery, K. Sheehan, O. Ciccarelli, A. J. Thompson, J. M. Brady, and P. M. Matthews, "Non-invasive mapping of connections between human thalamus and cortex using diffusion imaging." *Nature neuroscience*, vol. 6, no. 7, pp. 750–7, 2003.

[25] T. E. J. Behrens, M. W. Woolrich, M. Jenkinson, H. Johansen-Berg, R. G. Nunes, S. Clare, P. M. Matthews, J. M. Brady, and S. M. Smith, "Characterization and propagation of uncertainty in diffusion-weighted MR imaging." *Magnetic resonance in medicine : official journal of the Society of Magnetic Resonance in Medicine / Society of Magnetic Resonance in Medicine*, vol. 50, no. 5, pp. 1077–88, 2003.

[26] R. Behrman and A. Butler, *Preterm birth: causes, consequences, and prevention*. Institute of Medicine (US) Committee on Understanding Premature Birth and Assuring Healthy Outcomes, 2007.

[27] M. Bentivoglio and P. Mazzarello, "The history of radial glia," *Brain research bulletin*, vol. 49, no. 5, pp. 305–315, 1999.

[28] J. L. Bernal-Rusiel, M. Reuter, D. N. Greve, B. Fischl, and M. R. Sabuncu, "Spatiotemporal linear mixed effects modeling for the mass-univariate analysis of longitudinal neuroimage data," *NeuroImage*, vol. 81, pp. 358–370, 2013.

[29] B. A. Brody, H. C. Kinney, A. S. Kloman, and F. H. Gilles, "Sequence of central nervous system myelination in human infancy. I. An autopsy study of myelination." *Journal of neuropathology and experimental neurology*, vol. 46, no. 3, pp. 283–301, 1987.

[30] P. Broser, F. Vargha-Khadem, and C. A. Clark, "Robust subdivision of the thalamus in children based on probability distribution functions calculated from probabilistic tractography," *Neuroimage*, vol. 57, no. 2, pp. 403–415, 2011.

[31] C. J. Brown, S. P. Miller, B. G. Booth, S. Andrews, V. Chau, K. J. Poskitt, and G. Hamarneh, "Structural network analysis of brain development in young preterm neonates," *NeuroImage*, vol. 101, pp. 667–680, 2014.

[32] I. Bystron, C. Blakemore, and P. Rakic, "Development of the human cerebral cortex: Boulder Committee revisited." *Nature reviews. Neuroscience*, vol. 9, no. 2, pp. 110–22, 2008.

[33] M. J. Cardoso, A. Melbourne, G. S. Kendall, M. Modat, N. J. Robertson, N. Marlow, and S. Ourselin, "AdaPT: An adaptive preterm segmentation algorithm for neonatal brain MRI." *NeuroImage*, vol. 65, pp. 97–108, 2013.

[34] M. J. Cardoso, M. Modat, R. Wolz, A. Melbourne, D. Cash, D. Rueckert, and S. Ourselin, "Geodesic Information Flows: Spatially-Variant Graphs and Their Application to Segmentation and Fusion," *IEEE Transactions on Medical Imaging*, pp. 1–1, 2015.

[35] M. J. Cardoso, R. Wolz, M. Modat, N. C. Fox, D. Rueckert, and S. Ourselin, "Geodesic information flows." in *MICCAI 2012, part II. LNCS*, A. Peters, T., Fichtinger, G., Martell, Ed., vol. 15. Heidelberg: Springer, 2012, pp. 262–70.

[36] V. Chau, A. Synnes, R. E. Grunau, K. J. Poskitt, R. Brant, and S. P. Miller, "Abnormal brain maturation in preterm neonates associated with adverse developmental outcomes," *Neurology*, vol. 81, no. 24, pp. 2082–2089, 2013.

[37] T. Chomiak and B. Hu, "What is the optimal value of the g-ratio for myelinated fibers in the rat CNS? A theoretical approach," *PLoS ONE*, vol. 4, no. 11, 2009.

[38] T. F. Coleman and Y. Li, "An Interior Trust Region Approach for Nonlinear Minimization Subject to Bounds," *SIAM Journal on Optimization*, vol. 6, no. 2, pp. 418–445, 1996.

[39] K. L. Costeloe, E. M. Hennessy, S. Haider, F. Stacey, N. Marlow, and E. S. Draper, "Short term outcomes after extreme preterm birth in England: comparison of two birth cohorts in 1995 and 2006 (the EPICure studies)." *BMJ (Clinical research ed.)*, vol. 345, no. December, p. e7976, 2012.

[40] S. J. Counsell, A. D. Edwards, A. T. M. Chew, M. Anjari, L. E. Dyet, L. Srinivasan, J. P. Boardman, J. M. Allsop, J. V. Hajnal, M. A. Rutherford, and F. M. Cowan, "Specific relations between neurodevelopmental abilities and white matter microstructure in children born preterm," *Brain*, vol. 131, no. 12, pp. 3201–3208, 2008.

[41] S. J. Counsell, L. E. Dyet, D. J. Larkman, R. G. Nunes, J. P. Boardman, J. M. Allsop, J. Fitzpatrick, L. Srinivasan, F. M. Cowan, J. V. Hajnal, M. A.

Rutherford, and A. D. Edwards, "Thalamo-cortical connectivity in children born preterm mapped using probabilistic magnetic resonance tractography." *NeuroImage*, vol. 34, no. 3, pp. 896–904, 2007.

[42] S. J. Counsell, H. Zhang, E. Hughes, H. Steele, N. Tusor, G. Ball, A. Makropoulos, D. C. Alexander, J. V. Hajnal, and A. D. Edwards, "In vivo assessment of neurite density in the preterm brain using diffusion magnetic resonance imaging," in *International Society for Magnetic Resonance in Medicine*, vol. 22, 2014, p. 1745.

[43] A. Daducci, E. J. Canales-Rodríguez, H. Zhang, T. B. Dyrby, C. Daniel, D. C. Alexander, J.-P. Thiran, and C. Daniel, "Accelerated Microstructure Imaging via Convex Optimization (AMICO) from diffusion MRI data," *NeuroImage*, vol. 105, no. 0, pp. 32–44, 2015.

[44] A. N. Davison and J. Dobbing, "Myelination as a vulnerable period in brain development." *British medical bulletin*, vol. 22, no. 1, pp. 40–4, 1966.

[45] F. T. de Bruïne, A. A. van den Berg-Huysmans, L. M. Leijser, M. Rijken, S. J. Steggerda, J. van der Grond, and G. van Wezel-Meijler, "Clinical implications of mr imaging findings in the white matter in very preterm infants: a 2-year follow-up study," *Radiology*, vol. 261, no. 3, pp. 899–906, 2011.

[46] D. C. Dean, J. O'Muircheartaigh, H. Dirks, B. G. Travers, N. Adluru, A. L. Alexander, and S. C. Deoni, "Mapping an index of the myelin g-ratio in infants using magnetic resonance imaging," *NeuroImage*, 2016.

[47] A. R. Deipolyi, P. Mukherjee, K. Gill, R. G. Henry, S. C. Partridge, S. Veeraraghavan, H. Jin, Y. Lu, S. P. Miller, D. M. Ferriero, D. B. Vigneron, and A. J. Barkovich, "Comparing microstructural and macrostructural development of the cerebral cortex in premature newborns: diffusion tensor imaging versus cortical gyration." *NeuroImage*, vol. 27, no. 3, pp. 579–586, 2005.

[48] A. Dekaban, "Anatomical, developmental and pathological study development of the human thalamic nuclei," *Journal of Comparative Neurology*, vol. 100, pp. 63–97, 1954.

[49] M. S. Der Knaap, G. Van Wezel-Meijler, P. G. Barth, F. Barkhof, H. J. Adèr, and J. Valk, "Normal gyration and sulcation in preterm and term neonates: appearance on MR images." *Radiology*, vol. 200, no. 2, pp. 389–396, 1996.

[50] I. Drobnjak, D. Gavaghan, E. Süli, J. Pitt-Francis, and M. Jenkinson, "Development of a functional magnetic resonance imaging simulator for modeling realistic rigid-body motion artifacts," *Magnetic Resonance in Medicine*, vol. 56, no. 2, pp. 364–380, 2006.

[51] I. Drobnjak, G. S. Pell, and M. Jenkinson, "Simulating the effects of time-varying magnetic fields with a realistic simulated scanner," *Magnetic Resonance Imaging*, vol. 28, no. 7, pp. 1014–1021, 2010.

[52] J. Dubois, G. Dehaene-Lambertz, S. Kulikova, C. Poupon, P. S. Hüppi, and L. Hertz-Pannier, "The early development of brain white matter: A review of imaging studies in fetuses, newborns and infants." *Neuroscience*, 2013.

[53] J. Dubois, G. Dehaene-Lambertz, M. Perrin, J.-F. Mangin, Y. Cointepas, E. Duchesnay, D. le Bihan, and L. Hertz-Pannier, "Asynchrony of the early maturation of white matter bundles in healthy infants: quantitative landmarks revealed noninvasively by diffusion tensor imaging." *Human brain mapping*, vol. 29, no. 1, pp. 14–27, 2008.

[54] T. B. Dyrby, H. Lundell, M. W. Burke, N. L. Reislev, O. B. Paulson, M. Ptito, and H. R. Siebner, "Interpolation of diffusion weighted imaging datasets," *NeuroImage*, vol. 103, pp. 202–213, 2014.

[55] Z. Eaton-Rosen, M. J. Cardoso, A. Melbourne, E. Orasanu, A. Bainbridge, G. S. Kendall, N. J. Robertson, N. Marlow, and S. Ourselin, "Fitting parametric models of diffusion MRI in regions of partial volume," in *Proceedings of SPIE, Medical Imaging: Image Processing*, vol. 9784, 2016.

[56] Z. Eaton-Rosen, A. Melbourne, M. J. Cardoso, N. Marlow, and S. Ourselin, "Beyond the Resolution Limit: Diffusion Parameter Estimation in Partial Volume," in *International Conference on Medical Image Computing and Computer-Assisted Intervention*, 2016, pp. 605–612.

[57] Z. Eaton-Rosen, A. Melbourne, E. Orasanu, M. J. Cardoso, M. Modat, A. Bainbridge, G. S. Kendall, N. J. Robertson, N. Marlow, and S. Ourselin, "Longitudinal measurement of the developing grey matter in preterm subjects using multi-modal MRI," *NeuroImage*, 2015.

[58] L. Eikenes, G. C. Løhaugen, A.-M. Brubakk, J. Skranes, and A. K. Håberg, "Young adults born preterm with very low birth weight demonstrate widespread white matter alterations on brain DTI," *NeuroImage*, vol. 54, no. 3, pp. 1774–1785, 2011.

[59] D. C. V. Essen, D. Dierker, A. Z. Snyder, M. E. Raichle, A. L. Reiss, and J. Korenberg, "Symmetry of Cortical Folding Abnormalities in Williams Syndrome Revealed by Surface-Based Analyses." *Journal of Neuroscience*, vol. 39, no. April, pp. 1–38, 2006.

[60] U. Ferizi, T. Schneider, E. Panagiotaki, G. Nedjati-Gilani, H. Zhang, C. A. M. Wheeler-Kingshott, and D. C. Alexander, "A ranking of diffusion MRI compartment models with in vivo human brain data." *Magnetic resonance in medicine : official journal of the Society of Magnetic Resonance in Medicine / Society of Magnetic Resonance in Medicine*, vol. 72, no. 6, pp. 1785–92, 2014.

[61] R. D. Fields, "White matter in learning, cognition and psychiatric disorders," *Trends in Neurosciences*, vol. 31, no. 7, pp. 361–370, 2008.

[62] J. N. Giedd, J. M. Rumsey, F. X. Castellanos, J. C. Rajapakse, D. Kaysen, A. C. Vaituzis, Y. C. Vauss, S. D. Hamburger, and J. L. Rapoport, "A quantitative MRI study of the corpus callosum in children and adolescents." *Brain research. Developmental brain research*, vol. 91, no. 2, pp. 274–80, 1996.

[63] R. Goldenberg, J. Culhane, J. Iams, and R. Romero, "Epidemiology and Causes of Preterm Birth," *The Lancet*, pp. 75–84, 2008.

[64] I. S. Gousias, A. D. Edwards, M. A. Rutherford, S. J. Counsell, J. V. Hajnal, D. Rueckert, and A. Hammers, "Magnetic resonance imaging of the newborn brain: manual segmentation of labelled atlases in term-born and preterm infants." *NeuroImage*, vol. 62, no. 3, pp. 1499–509, 2012.

[65] D. N. Greve and B. Fischl, "Accurate and robust brain image alignment using boundary-based registration." *NeuroImage*, vol. 48, no. 1, pp. 63–72, 2009.

[66] C. F. Hagmann, E. de Vita, A. Bainbridge, R. Gunny, A. B. Kapetanakis, W. K. Chong, E. B. Cady, D. G. Gadian, and N. J. Robertson, "T2 at MR Imaging Is an Objective Quantitative Measure of Cerebral White Matter Signal Intensity Abnormality in Preterm Infants at Term-equivalent Age," *Radiology*, vol. 252, no. 1, pp. 209–217, 2009.

[67] X. Han, D. L. Pham, D. Tosun, M. E. Rettmann, C. Xu, and J. L. Prince, "CRUISE: Cortical reconstruction using implicit surface evolution," *NeuroImage*, vol. 23, no. 3, pp. 997–1012, 2004.

[68] M. Hasegawa, S. Houdou, T. Mito, S. Takashima, K. Asanuma, and T. Ohno, "Development of myelination in the human fetal and infant cerebrum: A myelin basic protein immunohistochemical study," *Brain and Development*, vol. 14, no. 1, pp. 1–6, 1992.

[69] L. He and N. A. Parikh, "Automated detection of white matter signal abnormality using T2 relaxometry: application to brain segmentation on term MRI in very preterm infants." *NeuroImage*, vol. 64, pp. 328–40, 2013.

[70] R. Heidemann, A. Anwander, T. Knosche, T. Feiweier, F. Fasano, J. Pfeuffer, and R. Turner, "High Resolution Diffusion-Weighted Imaging Showing Radial Anisotropy in the Human Cortex In Vivo," in *ISMRM*, vol. 17, no. 1, 2009.

[71] C. Hildebrand and R. Hahn, "Relation between myelin sheath thickness and axon size in spinal cord white matter of some vertebrate species," *Journal of the Neurological Sciences*, vol. 38, no. 3, pp. 421–434, 1978.

[72] P. S. Hüppi and J. Dubois, "Diffusion tensor imaging of brain development." *Seminars in fetal neonatal medicine*, vol. 11, no. 6, pp. 489–497, 2006.

[73] T. Jeon, V. Mishra, M. Ouyang, M. Chen, and H. Huang, "Synchronous Changes of Cortical Thickness and Corresponding White Matter Microstructure During Brain Development Accessed by Diffusion MRI Tractography from Parcellated Cortex." *Frontiers in neuroanatomy*, vol. 9, no. December, p. 158, 2015.

[74] B. Jeurissen, A. Leemans, J. D. Tournier, D. K. Jones, and J. Sijbers, "Investigating the prevalence of complex fiber configurations in white matter tissue with diffusion magnetic resonance imaging," *Human Brain Mapping*, vol. 34, no. 11, pp. 2747–2766, 2013.

[75] D. K. Jones, *Gaussian Modeling of the Diffusion Signal*, 2nd ed. Elsevier, 2013.

[76] D. K. Jones and M. Cercignani, "Twenty-five pitfalls in the analysis of diffusion MRI data." *NMR in biomedicine*, vol. 23, no. 7, pp. 803–20, 2010.

[77] D. K. Jones, T. R. Knösche, and R. Turner, "White matter integrity, fiber count, and other fallacies: the do's and don'ts of diffusion MRI." *NeuroImage*, vol. 73, pp. 239–54, 2013.

[78] E. Kaden, T. R. Knösche, and A. Anwander, "Parametric spherical deconvolution: inferring anatomical connectivity using diffusion MR imaging." *NeuroImage*, vol. 37, no. 2, pp. 474–488, 2007.

[79] E. Kaden, F. Kruggel, and D. C. Alexander, "Quantitative mapping of the per-axon diffusion coefficients in brain white matter," *Magnetic Resonance in Medicine*, vol. 00, pp. n/a–n/a, 2015.

[80] C. E. Kelly, D. K. Thompson, J. Chen, A. Leemans, C. L. Adamson, T. E. Inder, J. L. Y. Cheong, L. W. Doyle, and P. J. Anderson, "Axon density and axon orientation dispersion in children born preterm," *Human Brain Mapping*, vol. 37, no. 9, pp. 3080–3102, 2016.

[81] G. S. Kendall, A. Melbourne, S. Johnson, D. Price, A. Bainbridge, R. Gunny, A. Huertas-Ceballos, E. B. Cady, S. Ourselin, N. Marlow, and N. J. Robertson, "White matter NAA/Cho and Cho/Cr ratios at MR spectroscopy are predictive of motor outcome in preterm infants," *Radiology*, vol. 271, no. 1, pp. 230–238, 2014.

[82] I. Kostović and M. Judas, "The development of the subplate and thalamocortical connections in the human foetal brain." *Acta Paediatrica*, vol. 99, no. 8, pp. 1119–27, 2010.

[83] R. Kreis, L. Hofmann, B. Kuhlmann, C. Boesch, E. Bossi, and P. S. Hüppi, "Brain metabolite composition during early human brain development as measured by quantitative in vivo 1H magnetic resonance spectroscopy," *Magnetic Resonance in Medicine*, vol. 48, no. 6, pp. 949–958, 2002.

[84] M. Kuklisova-Murgasova, P. Aljabar, L. Srinivasan, S. J. Counsell, V. Doria, A. Serag, I. S. Gousias, J. P. Boardman, M. A. Rutherford, A. D. Edwards, J. V. Hajnal, and D. Rueckert, "A dynamic 4D probabilistic atlas of the developing brain." *NeuroImage*, vol. 54, no. 4, pp. 2750–63, 2011.

[85] ——, "NeuroImage A dynamic 4D probabilistic atlas of the developing brain," *NeuroImage*, vol. 54, no. 4, pp. 2750–2763, 2011.

[86] S. Kulikova, L. Hertz-Pannier, G. Dehaene-Lambertz, A. Buzmakov, C. Poupon, and J. Dubois, "Multi-parametric evaluation of the white matter maturation," *Brain Structure and Function*, vol. 220, no. 6, pp. 3657–3672, 2015.

[87] N. Kunz, H. Zhang, L. Vasung, and K. O'Brien, "Assessing white matter microstructure of the newborn with multi-shell diffusion MRI and biophysical compartment models," *NeuroImage*, vol. 96, pp. 288–99, 2014.

[88] A. Kuznetsova, P. B. Brockhoff, and R. H. B. Christensen, "Package lmerTest'."

[89] L. L. Latour, K. Svoboda, P. P. Mitra, and C. H. Sotak, "Time-dependent diffusion of water in a biological model system." *Proceedings of the National Academy of Sciences*, vol. 91, no. 4, pp. 1229–1233, 1994.

[90] C. Laule, E. Leung, D. K. B. Li, A. L. Traboulsee, D. W. Paty, A. L. Mackay, and G. R. W. Moore, "Myelin water imaging in multiple sclerosis: quantitative correlations with histopathology," *Multiple Sclerosis*, vol. 12, no. 6, pp. 747–753, 2006.

[91] C. Laule, P. Kozlowski, E. Leung, D. K. B. Li, A. L. Mackay, and G. R. W. Moore, "Myelin water imaging of multiple sclerosis at 7T: Correlations with histopathology," *NeuroImage*, vol. 40, no. 4, pp. 1575–1580, 2008.

[92] D. le Bihan, "Looking into the functional architecture of the brain with diffusion MRI." *Nature reviews. Neuroscience*, vol. 4, no. 6, pp. 469–80, 2003.

[93] A. Leemans and D. K. Jones, "The B-matrix must be rotated when correcting for subject motion in DTI data." *Magnetic resonance in medicine : official journal of the Society of Magnetic Resonance in Medicine / Society of Magnetic Resonance in Medicine*, vol. 61, no. 6, pp. 1336–49, 2009.

[94] L. Luo and D. D. O'Leary, "Axon Retraction and Degeneration in Development and Disease," *Annual Review of Neuroscience*, vol. 28, no. 1, pp. 127–156, 2005.

[95] L. C. Maas, P. Mukherjee, J. Carballido-Gamio, S. Veeraraghavan, S. P. Miller, S. C. Partridge, R. G. Henry, A. J. Barkovich, and D. B. Vigneron, "Early laminar organization of the human cerebrum demonstrated with diffusion tensor imaging in extremely premature infants." *NeuroImage*, vol. 22, no. 3, pp. 1134–40, 2004.

[96] B. Mädler, S. A. Drabycz, S. H. Kolind, K. P. Whittall, and A. L. Mackay, "Is diffusion anisotropy an accurate monitor of myelination?. Correlation of multi-component T2 relaxation and diffusion tensor anisotropy in human brain," *Magnetic Resonance Imaging*, vol. 26, no. 7, pp. 874–888, 2008.

[97] S. E. Maier and R. V. Mulkern, "Biexponential analysis of diffusion-related signal decay in normal human cortical and deep gray matter," *Magnetic Resonance Imaging*, vol. 26, no. 7, pp. 897–904, 2008.

[98] N. Marlow and D. Wolke, "Neurologic and developmental disability at six years of age after extremely preterm birth," *New England Journal of Medicine*, vol. 352, pp. 9–19, 2005.

[99] T. J. Mathews, A. M. Minino, M. J. K. Osterman, D. M. Strobino, and B. Guyer, "Annual Summary of Vital Statistics: 2008," *Pediatrics*, vol. 127, no. 1, pp. 146–157, 2011.

[100] A. M. Mathur, J. J. Neil, R. C. Mckinstry, and T. E. Inder, "Transport, monitoring, and successful brain MR imaging in unsedated neonates," *Pediatric Radiology*, vol. 38, no. 3, pp. 260–264, 2008.

[101] R. C. Mckinstry, A. Mathur, J. H. Miller, A. Ozcan, A. Z. Snyder, G. L. Schefft, C. R. Almli, S. I. Shiran, T. E. Conturo, and J. J. Neil, "Radial organization of developing preterm human cerebral cortex revealed by non-invasive water diffusion anisotropy MRI." *Cerebral Cortex*, vol. 12, no. 12, pp. 1237–1243, 2002.

[102] ——, "Radial organization of developing preterm human cerebral cortex revealed by non-invasive water diffusion anisotropy MRI." *Cerebral cortex (New York, N.Y. : 1991)*, vol. 12, no. 12, pp. 1237–43, 2002.

[103] J. A. Mcnab, J. R. Polimeni, R. Wang, J. C. Augustinack, K. Fujimoto, A. Stevens, T. Janssens, R. Farivar, R. D. Folkerth, W. Vanduffel, and L. L. Wald, "Surface based analysis of diffusion orientation for identifying architectonic domains in the in vivo human cortex," *NeuroImage*, vol. 69, pp. 87–100, 2013.

[104] A. Melbourne, Z. Eaton-Rosen, A. Bainbridge, G. S. Kendall, M. J. Cardoso, N. J. Robertson, and N. Marlow, "Measurement of myelin in the preterm brain : multi-compartment diffusion imaging and multi-component T 2 relaxometry," *MICCAI - in Press*, 2013.

[105] A. Melbourne, Z. Eaton-Rosen, A. Bainbridge, G. S. Kendall, M. J. Cardoso, N. J. Robertson, N. Marlow, and S. Ourselin, "Measurement of myelin in the preterm brain: multi-compartment diffusion imaging and multi-component T2 relaxometry." *Medical image computing and computer-assisted intervention : MICCAI ... International Conference on Medical Image Computing and Computer-Assisted Intervention*, vol. 16, no. Pt 2, pp. 336–44, 2013.

[106] A. Melbourne, Z. Eaton-Rosen, E. de Vita, A. Bainbridge, M. J. Cardoso, D. Price, E. Cady, G. S. Kendall, N. J. Robertson, N. Marlow, and S. Ourselin, "Multi-modal measurement of the myelin-to-axon diameter g-ratio in preterm-born neonates and adult controls," *Lecture Notes in Computer Science (including subseries Lecture Notes in Artificial Intelligence and Lecture Notes in Bioinformatics)*, vol. 8674 LNCS, no. PART 2, pp. 268–275, 2014.

[107] A. Melbourne, G. S. Kendall, M. J. Cardoso, R. Gunney, N. J. Robertson, N. Marlow, and S. Ourselin, "Radial structure in the preterm cortex; persistence of the preterm phenotype at term equivalent age?" *Medical image computing and computer-assisted intervention : MICCAI ... International Conference on Medical Image Computing and Computer-Assisted Intervention*, vol. 15, no. Pt 3, pp. 256–63, 2012.

[108] A. Melbourne, G. S. Kendall, M. J. Cardoso, R. Gunny, N. J. Robertson, N. Marlow, and S. Ourselin, "Preterm birth affects the developmental synergy between cortical folding and cortical connectivity observed on multimodal MRI," *NeuroImage*, vol. 89, pp. 23–34, 2014.

[109] A. Melbourne, N. Toussaint, D. Owen, I. Simpson, T. Anthopoulos, E. Vita, D. Atkinson, and S. Ourselin, "NiftyFit: a Software Package for Multi-parametric Model-Fitting of 4D Magnetic Resonance Imaging Data," *Neuroinformatics*, pp. 1–19, 2016.

[110] L. R. Ment, D. Hirtz, and P. S. Hüppi, "Imaging biomarkers of outcome in the developing preterm brain." *The Lancet*, vol. 8, no. 11, pp. 1042–1055, 2009.

[111] C. Metzler-Baddeley, M. J. O'Sullivan, S. Bells, O. Pasternak, and D. K. Jones, "How and how not to correct for CSF-contamination in diffusion MRI," *NeuroImage*, vol. 59, no. 2, pp. 1394–1403, 2012.

[112] D. J. Miller, T. Duka, C. D. Stimpson, S. J. Schapiro, W. B. Baze, M. J. Mcarthur, A. J. Fobbs, A. M. M. Sousa, N. šestan, D. E. Wildman, L. Lipovich, C. W. Kuzawa, P. R. Hof, and C. C. Sherwood, "Prolonged myelination in human neocortical evolution," *Proceedings of the National Academy of Sciences*, vol. 109, no. 41, pp. 16 480–16 485, 2012.

[113] M. Modat, G. R. Ridgway, Z. A. Taylor, M. Lehmann, J. Barnes, D. J. Hawkes, N. C. Fox, and S. Ourselin, "Fast free-form deformation using graphics processing units." *Computer methods and programs in biomedicine*, vol. 98, no. 3, pp. 278–84, 2010.

[114] J. R. Moffett, B. Ross, P. Arun, C. N. Madhavarao, and A. M. A. Namboodiri, "N-Acetylaspartate in the CNS: From neurodiagnostics to neurobiology," *Progress in Neurobiology*, vol. 81, no. 2, pp. 89–131, 2007.

[115] C. Nosarti, M. H. Al-Asady, S. Frangou, A. L. Stewart, L. Rifkin, and R. M. Murray, "Adolescents who were born very preterm have decreased brain volumes," *Brain*, vol. 125, no. 7, pp. 1616–1623, 2002.

[116] R. Nossin-Manor, D. Card, D. Morris, S. Noormohamed, M. M. Shroff, H. E. Whyte, M. J. Taylor, and J. G. Sled, "Quantitative MRI in the very preterm brain: assessing tissue organization and myelination using magnetization transfer, diffusion tensor and T imaging." *NeuroImage*, vol. 64, pp. 505–16, 2013.

[117] K. Oishi, S. Mori, P. K. Donohue, T. Ernst, L. Anderson, S. Buchthal, A. Faria, H. Jiang, X. Li, M. I. Miller, P. C. M. V. Zijl, and L. Chang, "NeuroImage Multi-contrast human neonatal brain atlas : Application to normal neonate development analysis," *NeuroImage*, vol. 56, no. 1, pp. 8–20, 2011.

[118] C. Ortinau and J. Neil, "The neuroanatomy of prematurity: Normal brain development and the impact of preterm birth." *Clinical anatomy (New York, N.Y.)*, vol. 00, no. June, pp. 168–183, 2014.

[119] S. Ourselin, R. Stefanescu, and X. Pennec, "Robust registration of multi-modal images: towards real-time clinical applications," *Medical image computing and computer-assisted intervention : MICCAI*, pp. 140–147, 2002.

[120] S. Ourselin, A. Roche, S. Prima, and N. Ayache, "Block matching: A general framework to improve robustness of rigid registration of medical images," *Medical image computing and computer-assisted intervention: MICCAI*, pp. 557–566, 2000.

[121] E. Panagiotaki, T. Schneider, B. Siow, M. G. Hall, M. F. Lythgoe, and D. C. Alexander, "Compartment models of the diffusion MR signal in brain white matter: a taxonomy and comparison." *NeuroImage*, vol. 59, no. 3, pp. 2241–54, 2012.

[122] A. S. Pandit, E. Robinson, P. Aljabar, G. Ball, I. S. Gousias, Z. Wang, J. V. Hajnal, D. Rueckert, S. J. Counsell, G. Montana, and A. D. Edwards, "Whole-brain mapping of structural connectivity in infants reveals altered connection strength associated with growth and preterm birth," *Cerebral Cortex*, vol. 24, no. 9, pp. 2324–2333, 2014.

[123] S. C. Partridge, P. Mukherjee, R. G. Henry, S. P. Miller, J. I. Berman, H. Jin, Y. Lu, O. A. Glenn, D. M. Ferriero, A. J. Barkovich, and D. B. Vigneron, "Diffusion tensor imaging: serial quantitation of white matter tract maturity in premature newborns." *NeuroImage*, vol. 22, no. 3, pp. 1302–14, 2004.

[124] O. Pasternak, N. Sochen, Y. Gur, N. Intrator, and Y. Assaf, "Free water elimination and mapping from diffusion MRI," *Magnetic Resonance in Medicine*, vol. 62, no. 3, pp. 717–730, 2009.

[125] A. Paydar, E. Fieremans, J. I. Nwankwo, M. Lazar, H. D. Sheth, V. Adisetiyo, J. A. Helpern, J. H. Jensen, and S. S. Milla, "Diffusional kurtosis imaging of the developing brain," *American Journal of Neuroradiology*, vol. 35, no. 4, pp. 808–814, 2014.

[126] S. Petrou, "Economic consequences of preterm birth and low birthweight," *BJOG: An International Journal of Obstetrics and Gynaecology*, vol. 110, no. April, pp. 17–23, 2003.

[127] T. Prasloski, B. Mädler, Q. S. Xiang, A. Mackay, and C. Jones, "Applications of stimulated echo correction to multicomponent T2 analysis," *Magnetic Resonance in Medicine*, vol. 67, no. 6, pp. 1803–1814, 2012.

[128] P. Rakic, "Neuronal-glial interaction during brain development," *Trends in Neurosciences*, vol. 4, pp. 184–187, 1981.

[129] J. Rose, R. Vassar, K. Cahill-Rowley, X. stecher Guzman, S. R. Hintz, D. K. Stevenson, and N. Barnea-Goraly, "Neonatal physiological correlates of near-term brain development on MRI and DTI in very-low-birth-weight preterm infants," *NeuroImage: Clinical*, 2014.

[130] S. E. Rose, X. Hatzigeorgiou, M. W. Strudwick, G. Durbridge, P. S. W. Davies, and P. B. Colditz, "Altered white matter diffusion anisotropy in normal and preterm infants at term-equivalent age." *Magnetic resonance in medicine : official journal of the Society of Magnetic Resonance in Medicine / Society of Magnetic Resonance in Medicine*, vol. 60, no. 4, pp. 761–7, 2008.

[131] D. Rueckert, L. I. Sonoda, C. Hayes, D. L. Hill, M. O. Leach, and D. J. Hawkes, "Nonrigid registration using free-form deformations: application to breast MR images." *IEEE transactions on medical imaging*, vol. 18, no. 8, pp. 712–21, 1999.

[132] N. Sadeghi, P. T. Fletcher, M. Prastawa, J. H. Gilmore, and G. Gerig, "Subject-specific prediction using nonlinear population modeling: Application to early brain maturation from DTI," in *Lecture Notes in Computer Science (including subseries Lecture Notes in Artificial Intelligence and Lecture Notes in Bioinformatics)*, vol. 8675 LNCS, no. PART 3, 2014, pp. 33–40.

[133] N. Sadeghi, M. Prastawa, P. T. Fletcher, J. Wolff, J. H. Gilmore, and G. Gerig, "Regional characterization of longitudinal DT-MRI to study white matter maturation of the early developing brain." *NeuroImage*, vol. 68, pp. 236–47, 2013.

[134] ——, "Regional characterization of longitudinal DT-MRI to study white matter maturation of the early developing brain," *NeuroImage*, vol. 68, pp. 236–247, 2013.

[135] N. Sadeghi, M. Prastawa, J. H. Gilmore, W. Lin, and G. Gerig, "Spatio-temporal analysis of early brain development," *2010 Conference Record of the Forty Fourth Asilomar Conference on Signals, Systems and Computers*, pp. 777–781, 2010.

[136] S. Saigal and L. W. Doyle, "An overview of mortality and sequelae of preterm birth from infancy to adulthood." *Lancet*, vol. 371, no. 9608, pp. 261–9, 2008.

[137] B. Scherrer, A. Schwartzman, M. Taquet, M. Sahin, S. P. Prabhu, and S. K. Warfield, "Characterizing brain tissue by assessment of the distribution of

anisotropic microstructural environments in diffusion-compartment imaging (DIAMOND)," *Magnetic Resonance in Medicine*, vol. 00, no. August, 2015.

[138] J. S. Shimony, C. D. Smyser, G. Wideman, D. Alexopoulos, J. Hill, J. Harwell, D. Dierker, D. C. van Essen, T. E. Inder, and J. J. Neil, "Comparison of cortical folding measures for evaluation of developing human brain," *NeuroImage*, vol. 125, pp. 780–790, 2016.

[139] R. S. Smith and J. Koles, "Myelinated thickness nerve fibers : computed velocity effect of myelin on conduction," *Physiology*, vol. 219, no. 5, pp. 5–7, 1970.

[140] S. M. Smith, M. Jenkinson, H. Johansen-Berg, D. Rueckert, T. E. Nichols, C. E. Mackay, K. E. Watkins, O. Ciccarelli, M. Z. Cader, P. M. Matthews, and T. E. J. Behrens, "Tract-based spatial statistics: voxelwise analysis of multi-subject diffusion data." *NeuroImage*, vol. 31, no. 4, pp. 1487–1505, 2006.

[141] S. M. Smith, M. Jenkinson, M. W. Woolrich, C. F. Beckmann, T. E. J. Behrens, H. Johansen-Berg, P. R. Bannister, M. de Luca, I. Drobnjak, D. E. Flitney, R. K. Niazy, J. Saunders, J. Vickers, Y. Zhang, N. de Stefano, J. M. Brady, and P. M. Matthews, "Advances in functional and structural MR image analysis and implementation as FSL." *NeuroImage*, vol. 23 Suppl 1, pp. S208–19, 2004.

[142] T. A. Smyser, C. D. Smyser, C. E. Rogers, S. K. Gillespie, T. E. Inder, and J. J. Neil, "Cortical Gray and Adjacent White Matter Demonstrate Synchronous Maturation in Very Preterm Infants." *Cerebral cortex (New York, N.Y. : 1991)*, pp. 1–9, 2015.

[143] L. Snook, C. Plewes, and C. Beaulieu, "Voxel based versus region of interest analysis in diffusion tensor imaging of neurodevelopment," *NeuroImage*, vol. 34, no. 1, pp. 243–252, 2007.

[144] R. Srinivasan, "Neonate imaging sub-system," 2005.

[145] G. J. Stanisz, A. Szafer, G. A. Wright, and R. M. Henkelman, "An analytical model of restricted diffusion in bovine optic nerve." *Magnetic resonance in medicine : official journal of the Society of Magnetic Resonance in Medicine / Society of Magnetic Resonance in Medicine*, vol. 37, no. 1, pp. 103–11, 1997.

[146] N. Stikov, J. S. W. Campbell, T. Stroh, M. Lavelée, S. Frey, J. Novek, S. Nuara, M.-K. Ho, B. J. Bedell, R. F. Dougherty, I. R. Leppert, M. Boudreau, S. Narayanan, T. Duval, J. Cohen-Adad, P. Picard, A. Gasecka, D. Côté, and G. bruce Pike, "In vivo histology of the myelin g-ratio with magnetic resonance imaging." *NeuroImage*, vol. 118, pp. 397–405, 2015.

[147] N. Stikov, L. M. Perry, A. Mezer, E. Rykhlevskaia, B. A. Wandell, J. M. Pauly, and R. F. Dougherty, "Bound pool fractions complement diffusion measures to describe white matter micro and macrostructure." *NeuroImage*, vol. 54, no. 2, pp. 1112–21, 2011.

[148] A. Szafer, J. Zhong, and J. C. Gore, "Theoretical model for water diffusion in tissues," *Magnetic resonance in medicine*, vol. 33, no. 5, pp. 697–712, 1995.

[149] D. Thompson, T. Inder, N. Faggian, L. Johnston, S. K. Warfield, P. J. Anderson, L. W. Doyle, and G. F. Egan, "Characterization of the corpus callosum in very preterm and full-term infants utilizing MRI," *Neuroimage*, vol. 55, pp. 479–490, 2011.

[150] R. Trivedi, R. K. Gupta, N. Husain, R. K. S. Rathore, S. Saksena, S. Srivastava, G. K. Malik, V. Das, M. Pradhan, M. K. Sarma, C. M. Pandey, and P. A. Narayana, "Region-specific maturation of cerebral cortex in human fetal brain: diffusion tensor imaging and histology." *Neuroradiology*, vol. 51, no. 9, pp. 567–76, 2009.

[151] T. K. Truong, A. Guidon, and A. W. Song, "Cortical depth dependence of the diffusion anisotropy in the human cortical gray matter in vivo," *PLoS ONE*, vol. 9, no. 3, 2014.

[152] H. Ullman, M. Spencer-Smith, D. K. Thompson, L. W. Doyle, T. E. Inder, P. J. Anderson, and T. Klingberg, "Neonatal MRI is associated with future cognition and academic achievement in preterm children," *Brain*, vol. 138, no. 11, pp. 3251–3262, 2015.

[153] D. C. van Essen, K. Ugurbil, E. Auerbach, D. Barch, T. E. J. Behrens, R. Bucholz, A. Chang, L. Chen, M. Corbetta, S. W. Curtiss, S. della Penna, D. Fein-

berg, M. F. Glasser, N. Harel, A. C. Heath, L. Larson-Prior, D. Marcus, G. Michalareas, S. Moeller, R. Oostenveld, S. E. Petersen, F. Prior, B. L. Schlaggar, S. M. Smith, A. Z. Snyder, J. Xu, and E. Yacoub, "The Human Connectome Project: A data acquisition perspective," *NeuroImage*, vol. 62, no. 4, pp. 2222–2231, 2012.

[154] B. J. M. Van Kooij, L. S. De Vries, G. Ball, I. C. Van Haastert, M. J. N. L. Benders, F. Groenendaal, and S. J. Counsell, "Neonatal tract-based spatial statistics findings and outcome in preterm infants." *AJNR. American journal of neuroradiology*, vol. 33, no. 1, pp. 188–94, 2012.

[155] G. van Steenkiste, B. Jeurissen, J. Veraart, A. J. Den Dekker, P. M. Parizel, D. H. J. Poot, and J. Sijbers, "Super-resolution reconstruction of diffusion parameters from diffusion-weighted images with different slice orientations," *Magnetic Resonance in Medicine*, vol. 00, no. November 2014, pp. n/a–n/a, 2015.

[156] J. J. Volpe, "Brain injury in premature infants: a complex amalgam of destructive and developmental disturbances." *Lancet neurology*, vol. 8, no. 1, pp. 110–24, 2009.

[157] S. B. Vos, D. K. Jones, M. A. Viergever, and A. Leemans, "Partial volume effect as a hidden covariate in DTI analyses." *NeuroImage*, vol. 55, no. 4, pp. 1566–76, 2011.

[158] K. L. West, N. D. Kelm, R. P. Carson, and M. D. Does, "A revised model for estimating g-ratio from MRI," *NeuroImage*, pp. 8–11, 2015.

[159] D. M. Wimberger, T. P. Roberts, A. J. Barkovich, L. M. Prayer, M. E. Moseley, and J. Kucharczyk, "Identification of" premyelination" by diffusion-weighted mri." *Journal of computer assisted tomography*, vol. 19, no. 1, pp. 28–33, 1995.

[160] N. S. Wood, N. Marlow, K. Costeloe, A. T. Gibson, and A. R. Wilkinson, "Neurologic and developmental disability after extremely preterm birth," *The New England Journal of Medicine*, vol. 343, no. 6, pp. 378–384, 2000.

[161] L. J. Woodward, P. J. Anderson, N. C. Austin, K. Howard, and T. E. Inder, "Neonatal MRI to predict neurodevelopmental outcomes in preterm infants." *The New England Journal of Medicine*, vol. 355, no. 7, pp. 685–94, 2006.

[162] D. A. Yablonskiy, G. L. Bretthorst, and J. J. H. Ackerman, "Statistical model for diffusion attenuated MR signal," *Magnetic Resonance in Medicine*, vol. 50, no. 4, pp. 664–669, 2003.

[163] J. M. Young, B. R. Morgan, H. E. Whyte, W. Lee, M. L. Smith, C. Raybaud, M. M. Shroff, J. G. Sled, and M. J. Taylor, "Longitudinal Study of White Matter Development and Outcomes in Children Born Very Preterm," *Cerebral Cortex*, pp. 1–12, 2016.

[164] H. Zhang, P. L. Hubbard, G. J. M. Parker, and D. C. Alexander, "Axon diameter mapping in the presence of orientation dispersion with diffusion MRI," *NeuroImage*, vol. 56, no. 3, pp. 1301–1315, 2011.

[165] H. Zhang, T. Schneider, C. A. Wheeler-Kingshott, and D. C. Alexander, "NODDI: practical in vivo neurite orientation dispersion and density imaging of the human brain." *NeuroImage*, vol. 61, no. 4, pp. 1000–16, 2012.